

2016

## Application of the Finite Element Method to Solve Coupled Multiphysics Problems for Subsurface Energy Extraction

Milad Ahmadi

*Louisiana State University and Agricultural and Mechanical College*

Follow this and additional works at: [https://digitalcommons.lsu.edu/gradschool\\_dissertations](https://digitalcommons.lsu.edu/gradschool_dissertations)



Part of the [Petroleum Engineering Commons](#)

---

### Recommended Citation

Ahmadi, Milad, "Application of the Finite Element Method to Solve Coupled Multiphysics Problems for Subsurface Energy Extraction" (2016). *LSU Doctoral Dissertations*. 165.

[https://digitalcommons.lsu.edu/gradschool\\_dissertations/165](https://digitalcommons.lsu.edu/gradschool_dissertations/165)

This Dissertation is brought to you for free and open access by the Graduate School at LSU Digital Commons. It has been accepted for inclusion in LSU Doctoral Dissertations by an authorized graduate school editor of LSU Digital Commons. For more information, please contact [gradetd@lsu.edu](mailto:gradetd@lsu.edu).

APPLICATION OF THE FINITE ELEMENT METHODS TO SOLVE COUPLED  
MULTIPHYSICS PROBLEMS FOR SUBSURFACE ENERGY EXTRACTION

A Dissertation

Submitted to the Graduate Faculty of the  
Louisiana State University and  
Agricultural and Mechanical College  
in partial fulfillment of the  
requirements for the degree of  
Doctor of Philosophy

in

Craft & Hawkins Department of Petroleum Engineering

by

Milad Ahmadi

B.S., University of Tehran, 2008

M.S., University of Tehran, 2011

August 2016

©Copyright by Milad Ahmadi, 2016  
All Rights Reserved

To my mother, Afshineh  
To my father, Amir  
To my sister, Mona  
and To the memory of my grandpaernts, Mahmoud and Zinat



# Acknowledgments

This dissertation could not have been completed without the great support that I have received from so many people over the years. I wish to offer my most genuine thanks to the following people.

First and foremost, I would like to thank my advisor, Dr. Arash Dahi-Taleghani, for his enduring support and guidance during my PhD. He patiently guided me through the dissertation process, and never accepting less than my best efforts. His advice on both research as well as on my career has been invaluable.

I would also like to thank my committee members Dr. Richard Hughes, Dr. Stephan Sears, Dr. Barbara Dutrow, and Dr. Shengli Chen for their brilliant comments, suggestions, criticisms, and helpful contributions that have given shape to this work.

I would especially like to thank Houman Bedayat, Denis Klimenko, Miguel Gonzalez, and Wei Wang for their help, support, suggestions, and incredible friendships. It has been a pleasure to share unforgettable moments with them.

To the Craft & Hawkins department of petroleum engineering for offering me the opportunity to advance my knowledge and skills through their graduate program. In addition, credit also goes to all members of Geomechanics Research Group at Louisiana State University for their help, support, and friendship during these years.

I gratefully acknowledge financial support for this work from the US Department of Energy under grant DE-EE0005125. I thank the Computer Modelling Group Ltd. for providing research and academic licenses for their reservoir simulation software.

I would like to express my most sincere gratitude and appreciation to my parents, Amir and Afshineh, and my sister, Mona. This work could not have been accomplished without their love and encouragement.

To friends and fellows of LSU for the good moments. To anyone that may I have forgotten. I apologize. Thank you as well.

Last but not least, I dedicate this work to the Supreme God and my spiritual teachers for priceless blessings, divine light and divine guidance, divine help and divine protection, divine love and mercy.

Milad Ahmadi

Louisiana State University

August 2016

# Table of Contents

Acknowledgments.....	iv
List of Tables .....	viii
List of Figures .....	ix
Abstract .....	xiv
Chapter 1    Overview .....	1
1.1    Introduction .....	1
1.2    Research Objectives .....	6
1.3    References .....	7
Chapter 2    Effects of Roughness and Offset on Fracture Compliance Ratio .....	9
2.1    Introduction .....	9
2.2    Determination of Fracture Compliance.....	12
2.3    Dynamic Technique to Measure Fracture Compliance .....	15
2.4    Numerical Simulation.....	17
2.5    Results and Discussion .....	20
2.6    Conclusions.....	31
2.7    References .....	32
Chapter 3    Impact of Thermally Reactivated Micro-Natural Fractures on Well Pro- ductivity in Shale Reservoirs .....	36
3.1    Introduction .....	36
3.2    Natural Fractures Characterization .....	39
3.3    Natural Fractures Characterization .....	41
3.4    Semicircular Bending Test .....	43
3.5    Results and Discussion .....	45
3.6    Conclusion.....	58
3.7    References .....	59
Chapter 4    Thermoporoelastic Analysis of Artificially Fractured Geothermal Reser- voirs; a Multiphysics Problem.....	62
4.1    Introduction .....	62
4.2    Closed-Loop Geothermal Systems .....	65
4.3    Governing Equations .....	67

4.3.1	Momentum Balance .....	69
4.3.2	Mass Balance .....	70
4.3.3	Energy Balance .....	70
4.3.4	Elastic Constitutive Law .....	72
4.3.5	Seismic Assessment .....	73
4.4	Verification .....	74
4.5	Results and Discussion .....	78
4.6	Conclusion .....	90
4.7	References .....	91
Chapter 5	Summary and Future Works .....	94
5.1	Summary .....	94
5.2	Recommendations for Future Works .....	96
Appendix A:	FEM Discretization of Non-Isothermal Saturated Porous Media .....	98
Appendix B:	Analytical Solution of Benchmark Problems .....	101
Appendix C:	Letters of Permission to Use Published Material .....	103
Vita .....		105

# List of Tables

2.1	Initial values of rock and fracture parameters. ....	19
3.1	Cohesive properties used in the numerical simulation.....	45
3.2	Properties of cemented natural fractures and intact rock.....	47
3.3	Properties of gas reservoir .....	56
4.1	Classification of low, medium and high enthalpy resources based on temperature of geothermal system (Adapted from Dickson and Fanelli (2013)) .....	64
4.2	Estimation of worldwide geothermal resources (Adapted from Armstead (1983))	65
4.3	List of required parameters to solve the Mandel’s problem.....	74
4.4	List of required parameters to solve the Theis-Jacob’s problem.....	76
4.5	List of parameters used to solve the Elder’s problem .....	77
4.6	List of parameters used to solve the Elder’s problem .....	79

# List of Figures

2.1	Fracture modeled as two rough surfaces in contact in the quasi-static approach. Normal and tangential displacements of the upper fracture face are denoted by $u_N^+$ and $u_T^+$ , and of the lower fracture face by $u_N^-$ and $u_T^-$ .....	17
2.2	(a) 2D FEM model built to represent a rough fracture. (b) Roughness is modeled with a right-angled triangle in this specific geometry. Definition of <i>Soft</i> and <i>Stiff</i> direction derives from asymmetry of fracture surface geometry. .	19
2.3	Quasi-static compliance ratio in the presence of saw-tooth-like structures at the fracture interface.....	22
2.4	Increase in compliance ratio as a function of asperity angle II for two different values of asperity angle I. Asperity angle I is equal to $5.71^\circ$ and $10.43^\circ$ in (a) and (b), respectively. ....	23
2.5	Change in compliance ratio as a function of asperity to fracture length ratio at asperity angle I of $1.15^\circ$ . ....	24
2.6	Plot of difference in shear displacement between opposite fracture faces for different asperity lengths. As the ratio of asperity length to fracture length increases, the amount of difference in shear displacement decreases which raises the compliance ratio as shown in Figure 2.5. ....	25
2.7	Schematic picture of a cantilever beam with a uniformly distributed load of $\omega$ .	25
2.8	For normal offset, there is no preferential dependence on direction. The horizontal axis shows the percentage of contact between asperities of the two fracture faces. Zero percent normal offset means asperity heights are fully in contact and there is no gap between two fracture faces. ....	26
2.9	Change in compliance ratio with tangential offset due to the top fracture face sliding to the right to make a gap between the fracture faces. ....	27
2.10	Change in compliance ratio when fracture faces are partially in contact. The abscissa shows the fraction of asperities that are in full contact. Zero percent contact means all of the asperities in one face are separated from the corresponding ones on the other face. ....	28

2.11	This figure shows how a waveform amplitude of a seismic wave is attenuated by the presence of a smooth fracture. The solid line shows the amplitude of a compressional seismic wave at the receiver in intact rock, while the dashed line is the waveform amplitude in the presence of a fracture. ....	30
2.12	Numerical results for dynamic measurements are compared with the single crack analytical solution presented in Equation (2.5). The dynamic compliance ratio increases slightly with an incremental increase in asperity angle. ....	31
3.1	Power-law aperture-size distribution in Groove Creek and Kinlaw formations shows much larger frequency of micro-fractures in comparison to large size fractures (Plot borrowed from Gale, 2002). ....	37
3.2	Distribution of natural fractures in flagstones, Caithness, Scotland. (Source: Mike Norton, Wikipedia) .....	40
3.3	Broken surface of natural fractures sealed with calcite in Barnett Shale. (Borrowed from Gale <i>et al.</i> , 2007) .....	41
3.4	Schematic picture of natural fracture modeled cohesive zone method. Cohesive failure occurs in three phases: initiation, evolution, and removal of the cohesive zone at the complete failure. ....	42
3.5	Bilinear traction-separation law. Opening is equal to the $\delta_0$ at the maximum tensile strength. Complete failure happens at the $\delta_f$ where traction-separation law is no longer valid. ....	43
3.6	Match of experimental semicircular bending test, obtained from the Sierra <i>et al.</i> (2010), with the numerical semicircular bending test. Numerical experiment uses cohesive interface theory to model fracture initiation-propagation. ....	44
3.7	The match of numerical upscaled semicircular bending tests with two different cohesive element sizes. The cohesive properties of the case with four-time larger cohesive elements are adjusted in a way to have the similar loading-displacement curve with the one with smaller cohesive elements. ....	45
3.8	The two dimensional model representing a mosaic frame of hydraulic fracture with natural fractures embedded on the surface of hydraulic fracture. Cohesive interface theory models opening of natural fractures. ....	46
3.9	Temperature distributions along the cohesive interface after 50 and 100 seconds. Minimum Temperature happens at the intersection of natural and hydraulic fracture. ....	48

3.10	Crack length vs. crack opening after 100 seconds for the longest and shortest cracks in the primary numerical example. Right vertical axis represents the cohesive interface SDEG which is the scalar stiffness degradation of cohesive interface with a range from 0 to 1. SDEG of 1 shows the complete failure of cohesive element.....	48
3.11	Aperture-size distribution after elapsed time of 100 s for the primary numerical example. Aperture is measured at the surface of hydraulic fracture where cemented cracks cross the surface of hydraulic fracture. ....	49
3.12	Length-size distribution after elapsed time of 100 s for the spacing of 1.25 cm, and temperature differences of 100 °C and 50 °C at the end of elapsed time. ..	49
3.13	Length-size distribution for three shale thermal conductivities. If the rock thermal conductivity is very low, it is more expected that all of the activated cracks have more uniform length.....	50
3.14	Length-size distribution for two cohesive interfaces after elapsed time of 100 s. Critical separation and critical failure points of the weaker cohesive interface are half of their values for the stronger interface. ....	50
3.15	Average crack length at different cracks spacings. In small spacings, a crack should first overcome the imposed stress by the neighbouring cracks which equals to less available energy to propagate deeper. ....	51
3.16	Average crack width at different cracks spacings after elapsed time of 100. Stress shadow effect leads to narrower cracks. ....	51
3.17	Total reactivated cracks length per length of hydraulic. Total activated cracks length is equal to the cumulative length of activated cracks lengths for a specific cracks spacing. ....	52
3.18	Schematic picture of equivalent wellbore radius including the wellbore inflow area, hydraulic fracture inflow area and activated natural microcracks inflow area. ....	53
3.19	Schematic picture of a reservoir block including rock matrix and reactivated natural fractures. ....	55
3.20	Cumulative gas production after 1 year, left figure, and 5 five years, right figure.	57
3.21	Percentage of increase in cumulative gas production during 5 years in a semi-log graph.....	58
4.1	Schematic picture of a geothermal system containing heat source, geothermal reservoir, cap rock and geofluid (Adapted from Dickson and Fanelli (2013)). ...	64



4.2	Schematic of closed loop geothermal system with fractured wellbore. Hydraulic fractures are filled with the high thermal-conductive proppants to improve the heat withdrawal efficiency from the reservoir. ....	67
4.3	Verification of numerical solution with the Mandel's analytical solution. Fluid can be extracted from the sides while top and bottom boundaries are impermeable. ....	75
4.4	Verification of numerical solution with the Theis-Jacob's analytical solution. The middle layer is permeable while the top and bottom layer are impermeable. Fluid trapped in the permeable layer can flow into the well.....	76
4.5	Verification of numerical temperature with the Elder's experimental benchmark at the dimensionless time of 0.1. The initial temperature of the medium is $10^{\circ}\text{C}$ . Half of the bottom boundary is exposed to a heat source, keeping its temperature at a constant value of $20^{\circ}\text{C}$ . Elder's benchmark is famous for illustrating the effect of buoyancy and convection. ....	77
4.6	The picture represents the mesh distribution across the considered domain, around the wellbore and two wings of the fracture. Displacement quadratic triangular elements, with six nodes on each element, in conjunction with linear triangular element for temperature and pore pressure cover the domain of finite element model. ....	80
4.7	Comparing thermal power into a horizontal well in a closed-loop geothermal system. The "NF", "F", and "KP" stand for unfractured well, fractured well, and thermal conductivity of the proppants, respectively. In the fractured wellbore, the artificial fracture is filled within three different types of proppants with thermal conductivities of 45, 100 and $150 \text{ W/m}^{\circ}\text{C}$ . The larger is the thermal conductivity of the proppants, the more is the produced thermal power. 81	81
4.8	Comparing thermal power into a fractured horizontal well in a closed-loop geothermal system. The " $\Delta T$ " stands for the initial temperature difference between the wellbore and reservoir. The temperature difference is the main driving force for the heat transfer between the wellbore and the reservoir. The larger is the temperature difference, the more is the produced thermal power. .	81
4.9	Comparing cumulative extracted heat from a horizontal well in a closed-loop geothermal system. The cumulative collected heat for the wellbore with the fracture filled within the high thermal conductive proppants is one order of magnitude larger than the unfractured wellbore.....	83
4.10	Comparing cumulative extracted heat from a horizontal well in a closed-loop geothermal system. This Figure suggest that the increase in the temperature difference can significantly improve the extracted heat.....	83

4.11	Temperature drop, in centigrade, across the geothermal model after 20 years of heat withdrawal. Temperature drop is calculated by subtraction of the current temperature from the initial temperature. ....	85
4.12	Temperature drop changes versus time, measured along one of the fracture wings. Fracture is filled by the proppants with thermal conductivity of 150 W/m/°C. The initial temperature gradient at the wellbore is 100°C. ....	85
4.13	Pressure drop, in Pa, across the geothermal model after 20 years of heat withdrawal. Pressure drop is calculated by subtraction of the current temperature from the initial temperature.....	86
4.14	Horizontal displacement, in meter, across the geothermal model after 20 years of heat withdrawal. The maximum horizontal displacement happens around the wellbore. ....	87
4.15	Vertical displacement, in meter, across the geothermal model after 20 years of heat extraction. The maximum vertical displacement happens around the wellbore. ....	87
4.16	Surface subsidence versus time in a closed-loop fractured wellbore. The magnitude of surface subsidence increases with time. The largest subsidence happens at the middle of the model where the horizontal well is intersected with a vertical fracture. ....	88
4.17	Principal horizontal stress across the geothermal model after 20 years of heat extraction. The stress unit is Pa. ....	89
4.18	Principal vertical stress across the geothermal model after 20 years of heat extraction. The stress unit is Pa. ....	89
4.19	Shear stress across the geothermal model after 20 years of heat extraction. The stress unit is Pa. ....	90

# Abstract

Fractures are a source of extra compliance in the rock mass. Fracture compliance can estimate the fracture roughness and the type of fluid filling the fracture. The focus of this research study in chapter 2 is to illustrate how the compliance ratio of rough fractures can diverge from the compliance ratio of smooth fractures. The imperfect interface of the fracture is modeled with saw-tooth-like structures. The defined saw-tooth-like structures of contact asperities impose an in-plane asymmetry in the shear direction. The compliance ratio of the rough fracture is larger than the compliance ratio of the smooth fracture. Interlocking and riding up effects may explain our findings in chapter 2.

Recovered core samples and extensive outcrops studies have proved the existence of natural fractures in many tight formations. These natural fractures are likely filled with diagenetic materials such as clays, quartz or calcite. In chapter 3, this study suggests that small cemented natural fractures can be opened by the induced tensile stress due to the temperature difference between the cold fracturing fluid and hot formation. Cohesive zone model (CZM) is utilized here to simulate these natural fractures. Contribution of these micro natural fractures to cumulative gas production from a shale reservoir is investigated by modifying the transmissibility coefficient. Reservoir simulation results in chapter 3 suggest that reactivated natural fractures in the tight formations at early stages can improve gas production up to 25%; however, their effect significantly reduces to 3% in long term.

Geothermal systems are identified as either open-loop systems (OLGS) or closed-loop systems (CLGS). The loss of working fluid, surface subsidence, formation compaction, and

induced seismicity are major challenges in OLGS. To address the indicated challenges, CLGS can be considered as an alternative option. To improve the heat extraction from closed-loop wells, this research study in chapter 4 suggests highly conductive hydraulic fractures for CLGS to improve heat extraction rate. The results suggest that fractures significantly improve thermal power and cumulative extracted heat in CLGS. Thermal conductivity of the proppants is the key parameter enhancing heat extraction.

# Chapter 1

## Overview

### 1.1 Introduction

Hydraulic fracturing has been recognized as the most effective technique for economic recovery in tight oil and gas formations in North America (Holditch, 2006; Moniz *et al.*, 2006). Induced fractures significantly improve wellbore-formation contact area by creating a highly permeable conduit in the reservoir. The direction of hydraulic fracture propagation depends on the direction of the minimum principal stress as well as natural fractures (Economides and Nolte, 2000; Dahi Taleghani and Olson, 2011). Natural fractures are mechanical discontinuities in rock with the lengths varying from micrometers to kilometers (Narr *et al.*, 2006). These fractures can be formed due to tectonic deformation, excessive pore pressure, or major temperature change. Core and outcrop studies, advanced logging tools, microseismic techniques and well testing analysis have proved the existence of natural fractures in many unconventional reservoirs. Due to the limited access to the subsurface and limited precision of seismic techniques, outcrops are the main source to speculate fracture's geometry in the subsurface. Existence of natural fractures in the outcrop samples could be an indicative of their existence in the subsurface. However, most of the outcrop studies are qualitative and the existing models studying the interaction of natural fractures with the hydraulic fracture mainly consider the contribution of large natural fractures. Large natural fractures are the ones with the dimensions comparable to the size of hydraulic fracture (Jeffrey *et al.*, 2009; Dahi Taleghani and Olson, 2014).

Naturally fractured reservoirs frequently exhibit anisotropy in permeability, geomechanical properties and seismic velocities as they exist in one or more sets of partially aligned series. This anisotropy makes the prediction of reservoir performance more difficult. In the reservoirs with low-matrix permeability, fractures act as the primary conduits for fluid flow, whereas in reservoirs with higher permeability, they act as shortcuts for fluid flow. Contribution of natural fractures in the hydrocarbon recovery is more significant in the tight formations with low permeability than permeable reservoirs. However, they can also increase the leak-off volume during the fracturing treatments leading to early screenouts or poorly propped hydraulic fractures. Inaccurate evaluation of natural fractures not only affects the performance of waterflooding projects leading to low sweep efficiency, but also causes poor drilling performance resulting from lost circulation (Narr *et al.*, 2006). Knowledge of the orientation and density of fractures in the subsurface are thus important for designing well layout for optimal production and choosing an appropriate EOR technique (Reiss, 1980; Nelson, 2001; Saidi, 1987). Arrest and diversion of hydraulic fracture front into the pre-existing natural fractures have been the subject of many experimental and theoretical studies (Gonzalez *et al.*, 2015).

In reality, fracture faces are not smooth and instead consist of the asperities and morphological irregularities (Nagy, 1992; Yoshioka and Scholz, 1989b). These asperities are generally aligned perpendicular to the direction of the crack propagation or the direction of the fluid flow in the sedimentary rocks (Aydan *et al.*, 1996). The distribution and height of these ridges depend on the direction of the fracture slippage, rate of the slippage and the magnitude of the shearing stress (Durney and Ramsay, 1973). Degree of contact between fracture faces controls both fracture mechanical and hydromechanical properties. For instance, fracture ability to allow the fluid flow and to conduct the electrical current depends on the degree of contact between the fracture faces (Brown, 1989). Fracture compliance can be used to estimate the degree of fracturing of the rock mass, type of fluid filling the fracture and fracture roughness (Verdon and Wstefeld, 2013; Yoshioka and Scholz, 1989a).

Assessing the ratio of normal to tangential compliance may help in reservoir characterization, because compliance ratio depends on the type of material filling the fracture, such as clay or cement between the fracture faces, or fluid saturating the fracture, and the degree of fracture roughness. In Chapter 2, this research study uses the finite-element method (FEM) to investigate the effects of surface asperities and fracture offset on the fracture compliance ratio. To characterize the geometry of the fracture interface, we model fracture faces as periodic saw-tooth-like structures in a Cartesian system. The idea of such a specific geometry is inspired by Aydan *et al.* (1996), who reported saw-tooth-like structures at the fracture interface of sheeting joints in granite.

Field studies have confirmed the existence of a critical threshold that cracks with aperture less than this threshold are fully filled with diagenetic materials (Laubach, 2000). Laboratory measurements have proved that these filled natural fractures may act as the weak path for rock failure. For instance in Barnett shale samples, tensile strength of cemented cracks can be about 10 times lower than the tensile strength of intact rocks (Gale *et al.*, 2007). Power-law distribution of natural fractures indicate that small-size fractures are orders of magnitudes more than the large-size fractures in the tight formations. Therefore, it is not surprising if the induced hydraulic fractures are intersecting thousands of these small-fractures. Since the small-size natural fractures exist in large numbers, only partial reactivation of these fractures may affect fluid flow in the vicinity of the hydraulic fracture. This effect could be positive by enhancing the permeability around the fracture and improving hydrocarbon production, or could be negative by increasing the leak-off volume and boosting the capillary trapping. The entrapped water, which is essentially part of the leak-off volume that will never produce, could hinder hydrocarbon flow from the formation into the hydraulic fracture. Low required energy for the reactivation of small natural fractures makes them easy targets for reopening if large enough tensile stress is available at the surface of hydraulic fracture. Parameters controlling the opening of these small fractures are the tensile strength of cementing materials filling the fractures, magnitude of the tensile stress, and fractures density.

Fracturing fluid is frequently pumped with the temperature close to the surface temperature; therefore, its temperature at the bottomhole usually differs from the reservoir temperature, especially in deep and hot formations. Temperature of fracturing fluid delivered at the surface of hydraulic fracture depends on the injection rate, casing/tubing diameter, heat capacity of fracturing fluid, and fracture width. Temperature difference between cold fracturing fluid and hot reservoir rock induces tensile stress at the surface of hydraulic fracture. Magnitude of induced thermal stress is not large enough to induce large cracking in the rock, but it may be sufficient for opening of small-size natural fractures filled with the digenic materials since they are weaker than the intact rock. In chapter 3, this study aims to quantitatively estimate the opening of small pre-existing natural fractures, activated by the induced thermal stress between the hot formation and cold fracturing fluid, and show their contribution in the hydrocarbon recovery. Sensitivity analysis on the parameters controlling reactivation of pre-existing natural fractures is examined to determine the significance of each parameter on the opening of natural fractures.

Drastic climate changes during the last century caused by the emission of greenhouse gases from the burning fossil fuels has encouraged countries to expand the application of clean and sustainable energy resources. Geothermal energy is one of these sustainable resources and the general interest in the production of electricity from the geothermal power plants has immensely risen in recent years. Hot dry rocks are one of the common geothermal resources in the world. In these reservoirs, there is not enough fluid in place to be used for the heat extraction. Lack of fluid in place in the hot dry rock reservoirs may have a significant drawback. To overcome this problem, a working fluid should be injected into the reservoir to absorb the heat, and later be produced from production wells. In this system, enough reservoir permeability is crucial for the project success. In a reservoir with low permeability, hydraulic fracturing treatments are performed to increase injectivity and productivity. The amount of the produced heat in this system depends on the rock temperature, rate of fluid circulation in the reservoir, and the swept volume by the injected working fluid.



Loss of the working fluid, affecting total cost of the produced electricity, is a common issue. However, drawbacks are not limited to only this issue. Surface subsidence, formation compaction, induced earthquakes, and consequent damages to the wellbore integrity are other disadvantages of heat extraction from open-loop systems (Majer *et al.*, 2007).

To address the indicated issues, closed-loop geothermal system can be considered as an alternative solution. In this method, a working fluid, with low-boiling point, is circulated inside a series of coaxial sealed pipes to extract the stored heat in the reservoir. The low-boiling point improves the heat extraction efficiency (Diao *et al.*, 2004). It is expected that the lack of fluid production/injection from/into the reservoir should not significantly affect the pore pressure distribution. The closed-loop system has negligible environmental hazard compared to the open-loop system. For instance, produced water in an open-loop system contains high levels of sulfur, salt, and radioactive elements. Therefore, extracted water should be injected back into the reservoir which is a costly process (Kagel *et al.*, 2005). Land subsidence is another drawback in the open-loop systems. Production of the ground water reduces the pore pressure. Most of the open-loop facilities address this problem with reinjection of the produced fluid into the reservoir; however, this solution can induce significant seismic events. For instance, induced earthquakes in an open-loop geothermal plant in Basel, Switzerland, led to suspension of the whole project (Giardini, 2009). In chapter 4, focus of the research study is on enhancing heat extraction from a closed-loop geothermal wellbore via thermal conductive fractures. A thermoporoelastic finite element model is developed to study the geomechanical behavior of the proposed system as well as heat production. Thermoporoelasticity enables us to couple temperature, pore pressure, and displacement changes in the reservoir especially close to the wellbore. To solve the governing partial equations, Finite Element Method (FEM) is used to solve the governing equations.

## 1.2 Research Objectives

The proposed research has the following objectives:

- Investigate the effects of surface asperities and fracture offset on the fracture compliance ratio. Presence of fractures in a rock medium makes the medium more compliant. The magnitude of this additional compliance depends on various parameters such as fracture roughness, type of the fluid filling the fracture, fluid viscosity, rock permeability, fracture connectivity and the presence of cement, clay and other fracture fillings. In this research study, fracture rough interface is modeled with periodic saw-tooth-like structures in a Cartesian system. This research proposal studies different geometrical and offset configurations to show how compliance ratio is a function of available contact area at the fracture interface and also the size of the asperities.
- To quantitatively estimate the opening of small pre-existing natural fractures, activated by the induced thermal stress between the hot formation and cold fracturing fluid, and show their contribution in the hydrocarbon recovery. Cohesive zone model (CZM) is utilized here to simulate these natural fractures. Tensile strength of diagenetic cements, temperature difference between the fracturing fluid and formation, fractures spacing, and rock conductivity are the parameters controlling the opening and length of reactivated micro-fractures. Sensitivity analysis on these parameters is examined to determine the significance of each parameter on the opening of natural fractures.
- To provide a comprehensive analysis of a new method for heat extraction from the low-enthalpy geothermal reservoirs without mass withdrawal. The developed coupled numerical model in this study assesses the effectiveness of the proposed closed-loop configuration including the induced hydraulic fractures propped with highly thermal conductive materials to enhance heat production. Closed-loop geothermal system can be considered as an alternative solution for the open-loop systems. The level of surface

subsidence and seismic risk assessment in the proposed technique is also measured to investigate the safety and environmental hazards of proposed technique.

### 1.3 References

- Aydan, O., Y. Shimizu, and T. Kawamoto. "The anisotropy of surface morphology and shear strength characteristics of rock discontinuities and its evaluation." NARMS 96 (1996): 1391-1398.
- Brown, S. R. "Transport of fluid and electric current through a single fracture." *Journal of Geophysical Research: Solid Earth* 94, no. B7 (1989): 9429-9438.
- Bonnet, E., O. Bour, N. E. Odling, P. Davy, I. Main, P. Cowie, and B. Berkowitz. "Scaling of fracture systems in geological media." *Reviews of geophysics* 39, no. 3 (2001): 347-383.
- Diao, N., Q. Li, and Z. Fang. "Heat transfer in ground heat exchangers with groundwater advection." *International Journal of Thermal Sciences* 43.12 (2004): 1203-1211.
- Dahi Taleghani, A., and J. Olson. "Numerical modeling of multistranded-hydraulic-fracture propagation: accounting for the interaction between induced and natural fractures." *SPE Journal* 16.3 (2011): 575-581.
- Dahi Taleghani, A., and J. E. Olson. "How natural fractures could affect hydraulic-fracture geometry." *SPE Journal* 19, no. 01 (2014): 161-171.
- Durney, D. W., and J. G. Ramsay. "Incremental strains measured by syntectonic crystal growths." *Gravity and tectonics* 67 (1973): 96.
- Economides, M. J. and K.G. Nolte. "Reservoir stimulation." Wiley Press, 2000.
- Gale, J. FW, R. M. Reed, and J. Holder. "Natural fractures in the Barnett Shale and their importance for hydraulic fracture treatments." *AAPG bulletin* 91, no. 4 (2007): 603-622.
- Giardini, D. "Geothermal quake risks must be faced" *Nature* 462.7275 (2009): 848-849.
- Gonzalez-Chavez, M., P. Puyang, and A. D. Taleghani. "From semi-circular bending test to microseismic maps: an integrated modeling approach to incorporate natural fracture effects on hydraulic fracturing." *Unconventional resources technology conference, SPE*. Aug. 2015.
- Holditch, S. A. "Tight gas sands." *Journal of Petroleum Technology* 58, no. 06 (2006): 86-93.
- Jeffrey, R., X. Zhang, and M. Thiercelin. "Hydraulic Fracture Offsetting in Naturally Fractured Reservoirs: Quantifying a Long-Recognized Process." *SPE Hydraulic Fracturing Technology Conference*. 2009.
- Kagel, A., D. Bates, and K. Gawell. "A guide to geothermal energy and the environment Washington, DC: Geothermal Energy Association, (2005).

- Laubach, S. E. "Practical approaches to identifying sealed and open fractures." AAPG bulletin 87, no. 4 (2003): 561-579.
- Majer, E. L., R. Baria, M. Stark, S. Oates, J. Bommer, B. Smith, and H. Asanuma. "Induced seismicity associated with enhanced geothermal systems" *Geothermics* 36.3 (2007): 185-222.
- Moniz, E. J., H. D. Jacoby, A. J. M. Meggs, R. C. Armstrong, D. R. Cohn, S. R. Connors, J. M. Deutch, Q. J. Ejaz, J. S. Hezir, and G. M. Kaufman. "The future of natural gas." Cambridge, MA: Massachusetts Institute of Technology (2011).
- Nagy, P. B. "Ultrasonic classification of imperfect interfaces." *Journal of Nondestructive evaluation* 11, no. 3-4 (1992): 127-139.
- Narr, W., D. W. Schechter, and L. B. Thompson. *Naturally fractured reservoir characterization*. Richardson, TX: Society of Petroleum Engineers, 2006.
- Nelson, R. "Geologic analysis of naturally fractured reservoirs." Gulf Professional Publishing, 2001.
- Potluri, N. K., D. Zhu, and A. D. Hill. "The effect of natural fractures on hydraulic fracture propagation." In *SPE European Formation Damage Conference*. Society of Petroleum Engineers, 2005.
- Reiss, L. H. "The reservoir engineering aspects of fractured formations". Vol. 3. Editions Technip, 1980.
- Saidi, A. M. "Reservoir Engineering of Fractured Reservoirs (fundamental and Practical Aspects)." Total, 1987.
- Verdon, J. P., and A. Wstefeld. "Measurement of the normal/tangential fracture compliance ratio (ZN/ZT) during hydraulic fracture stimulation using Swave splitting data." *Geophysical Prospecting* 61, no. s1 (2013): 461-475.
- Warpinski, N. R., and L. W. Teufel. "Influence of geologic discontinuities on hydraulic fracture propagation." *Journal of Petroleum Technology* 39, no. 02 (1987): 209-220.
- Yoshioka, N., and Ch. H. Scholz. "Elastic properties of contacting surfaces under normal and shear loads, 1, Theory." *Journal of Geophysics. Res* 94, no. B12 (1989): 17681-17690.
- Yoshioka, N., and Ch. H. Scholz. "Elastic properties of contacting surfaces under normal and shear loads: 2. Comparison of theory with experiment." *Journal of Geophysical Research: Solid Earth* 94, no. B12 (1989): 17691-17700.

# Chapter 2

## Effects of Roughness and Offset on Fracture Compliance Ratio<sup>\*</sup>

### 2.1 Introduction

Significant percentage of hydrocarbon reservoirs are naturally fractured while some of these reservoirs have low permeability (Reiss, 1980; Nelson, 2001). Economic oil or gas production from these reservoirs depends on the connectivity of natural fractures network and execution of hydraulic fracturing treatments. Fractures can be defined as discontinuities in rock caused by tectonic deformation, excessive pore pressure, or major temperature change. Natural fractures may act as shortcuts or preferential flow paths for reservoir fluid recovery. Because fractures in hydrocarbon reservoirs often exist in one or more sets of partially aligned fractures, naturally fractured reservoirs frequently exhibit anisotropy in permeability, geomechanical properties and seismic velocities. This anisotropy makes the prediction of reservoir performance more difficult (Bedayat and Dahi Taleghani, 2016). Consequently, characterizing natural fractures in the subsurface is essential. The inaccurate evaluation of natural fractures not only affects the performance of waterflooding projects leading to low sweep efficiency, but also causes poor drilling performance resulting from lost circulation (Narr *et al.*, 2006).

---

<sup>\*</sup>Part of this chapter 2 previously appeared as "Ahmadi, M., A. Dahi Taleghani, and C. M. Sayers. The Effects of Roughness and Offset on Fracture Compliance Ratio. *Geophysical Journal International* (2016) 205 (1): 454-463" and "Ahmadi, M., A. Dahi Taleghani, and C. M. Sayers. Direction Dependence of Fracture Compliance Induced by Slickensides. *Geophysics* (2014) 79 (4): C91-C96". There are reprinted by permission of Oxford University Press and Society of Exploration Geophysicists (Appendix C).

In reality, fracture faces are not smooth and instead have rough-walled structures (Yoshioka and Scholz, 1989a; Yoshioka and Scholz, 1989b; Nagy, 1992). Fracture faces consist of the asperities and morphological irregularities. These asperities are generally aligned perpendicular to the direction of the crack propagation or the direction of the fluid flow in the sedimentary rocks (Paterson, 1958; Aydan *et al.*, 1996). The distribution and height of these ridges depend on the direction of the fracture slippage, rate of the slippage and the magnitude of the shearing stress (Durney and Ramsay, 1973). Aydan *et al.* (1996) suggested that the fracture discontinuities have different shear strengths in the different shear directions.

The degree of contact between fracture faces controls both fracture mechanical and hydromechanical properties. For instance, fracture ability to allow the fluid flow and to conduct electrical current depends on the degree of contact between the fracture faces (Brown, 1989). Fracture roughness and fracture aperture control fluid flow and proppant delivery during hydraulic fracturing treatments (Van Dam and de Pater, 1999). Liu (2005) discussed how the roughness affects the fracture mechanical and hydraulic apertures and if the mechanical aperture is at the same scale as the surface roughness, it is no longer realistic to assume that the mechanical and hydraulic apertures are equal, requiring correction in the fracture aperture estimated from the seismic data to be further used in reservoir simulations. Fracture roughness is scale dependent. In other words, the observed distribution of roughness significantly depends on the considered wavelength (Power *et al.*, 1988; Sagy *et al.*, 2007; Candela *et al.*, 2009). Root mean square (rms), joint roughness coefficient, height of roughness, maximumminimum height difference, Fourier power spectrum and wavelet power spectrum are some of the processing techniques used to quantify roughness and structure of the fracture asperities (Sagy *et al.*, 2007; Candela *et al.*, 2009).

There are several methods for predicting, evaluating and characterizing natural fractures in the subsurface, including analysis of core samples, well-logging techniques and seismic methods (Laubach *et al.*, 2000; Liu, 2005; Gale *et al.*, 2007; Olson *et al.*, 2009). Comprehensive knowledge of natural fractures (fracture orientation, spacing and spatial distribution)

can tremendously improve the well-layout design to maximize the likelihood of intersecting natural fractures, and can greatly enhance hydrocarbon production in low-permeability reservoirs. Although fracture data obtained from core analysis and borehole imaging are very useful to understand the existence of fractures in the subsurface, these data do not provide information between the wells. Therefore, other measurements, such as seismic velocity and amplitude, are required to characterize fracture density and orientation away from the wells (Sayers, 2009; Bachrach, 2013). Fracture size, orientation and density can be estimated from seismic data (Liu *et al.*, 2003; Maultzsch *et al.*, 2003). Seismic wave velocities, amplitudes and spectral characteristics can be distorted by the presence of fractures. This distortion can be used to further estimate fracture compliance, and can improve our knowledge about the fractured reservoir in order to better predict its behavior and design better depletion strategies.

The velocity of seismic waves in the subsurface significantly depends on rock type, stress state, pore pressure, fluid type and the presence or absence of natural fractures. Fractures can change both compressional and shear wave velocities. The variation of seismic wave velocities through the formation is sensitive to fracture properties such as fracture orientation, spacing, aperture, length, saturation and the presence or absence of cement, clay and other types of fracture fill (Sayers and Kachanov, 1991; Sayers and Kachanov, 1995; Schoenberg and Sayers, 1995; Boadu and Long, 1996; Leucci and De Giorgi, 2006; Lubbe *et al.*, 2008).

Fracture compliance can be used to estimate the degree of fracturing of the rock mass, type of fluid filling the fracture and fracture roughness (Schoenberg and Sayers, 1995; Yoshioka and Scholz, 1989a; Lubbe *et al.*, 2008; Verdon and Wustefeld, 2013; Ahmadi *et al.*, 2014; Rubino *et al.*, 2014). Fracture compliance can be represented as a second-rank tensor, with normal and shear components. Assessing the ratio of normal to tangential compliance may help in reservoir characterization, because compliance ratio depends on the type of material filling the fracture, such as clay or cement between the fracture faces (Sayers *et al.*, 2009), or fluid saturating the fracture, and the degree of fracture roughness. In this study, we aim

to show how compliance ratio can be affected by rough interface contact area. We calculate the compliance ratio using two different approaches: quasi-static and dynamic. In the quasi-static method, we calculate compliance from the jump in the displacement across the fracture interface divided by applied stress. However, in the dynamic technique, we calculate transmission coefficient as the ratio of waveform peak amplitudes to estimate compliance ratio.

## 2.2 Determination of Fracture Compliance

Fracture compliance depends on the mechanical properties of the fracture network and host rock, structure of fracture roughness and degree of cementation or mineralization on the fracture faces (Lubbe *et al.*, 2008; Sayers *et al.*, 2009; Rubino *et al.*, 2014). Fracture compliance can have applications in different fields, such as rock damage and stability analysis, hydrocarbon recovery, hydraulic fracturing, disposal of nuclear wastes, fault slippage and laboratory nondestructive tests (Mollhoff *et al.*, 2010). In fractures with the ability of fluid exchange via small pathways, Hudson *et al.* (1996) suggest that for a random distribution of coplanar cracks in an infinite domain, the ratio  $\frac{B_N}{B_T}$  of the normal compliance  $B_N$  to shear compliance  $B_T$  is

$$\frac{B_N}{B_T} = \frac{(1 + A)(1 - \frac{\nu}{2})}{1 + B} \quad (2.1)$$

where

$$A = \frac{4a}{\pi c} \left( \frac{i\omega\eta_f}{\mu} \right) \left( \frac{1 - \nu}{2 - \nu} \right) \quad (2.2)$$

and

$$B = \left[ \frac{2a}{\pi c} \frac{\kappa_f}{\mu} (1 - \nu) \right] \left( 1 - \frac{3i\kappa_f k^2 K_r}{4\pi\nu a^2 c \omega \eta_f} \right)^{-1} \quad (2.3)$$



Here,  $\mu$  and  $\nu$  are the shear modulus and Poisson's ratio of the solid matrix,  $\kappa_f$  and  $\eta_f$  are the bulk modulus and viscosity of the fluid, respectively,  $\frac{c}{a}$  is the aspect ratio of the fractures,  $\omega$  is the angular frequency,  $k$  is the wavenumber and  $K_r$  is the permeability of the rock medium including the contribution of cracks and cavities in permeability enhancement.

In fractured reservoirs with very low permeability, the compliance ratio in Equation (2.1) simplifies to

$$\frac{B_N}{B_T} = \frac{(1 + A)(1 - \frac{\nu}{2})}{1 + \frac{2a}{\pi c} \frac{\kappa_f}{\mu}(1 - \nu)} \quad (2.4)$$

An increase in the bulk modulus of the fluid leads to a decrease in compliance ratio. Moreover, the saturation of fractures with intrinsic fluid affects compliance ratio because effective bulk modulus is a function of fluid saturation. For instance, compliance ratio in a fractured rock saturated with gas is larger than that of a water saturated rock (Sayers and Kachanov, 1995; Hobday and Worthington, 2012; Verdon and Wustefeld, 2013). A simplified version of Equation (2.4) for the case of a dry or gas-filled fracture within rough faces is shown in Equation (2.5):

$$\frac{B_N}{B_T} = \frac{1 - \nu}{1 - \frac{\nu}{2}} \quad (2.5)$$

None of the mentioned models consider the effect of diagenesis or contact points along the fracture length. In the proposed formulae, fracture surfaces are considered as two separated faces with no welding, cementation, or interaction with each other. In particular, fracture faces do not have any relative shear strength against sliding induced by interface roughness or the presence of asperities. Resistance against sliding generally depends on roughness, bridging, cementation and contact areas between fracture faces.

Fracture compliance can be measured using either a quasi-static or dynamic technique (Pyrak-Nolte *et al.*, 1987; Pyrak-Nolte *et al.*, 1990; Barton, 2007). Quasi-static compliance

is measured at zero frequency; however, dynamic compliance corresponds to finite frequency. Pyrak-Nolte *et al.* (1987) and Pyrak-Nolte *et al.* (1990), through ultrasonic laboratory experiments, showed quasi-static normal compliance in quartz monzonite samples is larger than dynamic normal compliance in the same rock sample. The magnitude of the discrepancy in normal compliance between these techniques rises as the applied compressive stress on the sample increases. Friction is considered to be one of the causes of this discrepancy. However, another possibility for this discrepancy can be related to the difference in the magnitude of strain amplitudes in quasi-static and dynamic laboratory experiments. Strain amplitude in dynamic measurements is much smaller than in static measurements. The amplitude of elasticwaves is too small to trigger sliding of fracture faces; therefore, displacement magnitude may be the dominant cause of the difference between the static and dynamic measurements. From a field study on water-saturated fractures at the north coast of Scotland, Hobday and Worthington (2012) concluded that the compliance ratio of saturated fractured rocks in this region is less than 0.1. This low value of compliance ratio is what they attribute it to the presence of water contained in the fractures. They suggested that partially air-saturated fractures can have larger compliance ratio values; however, they could not characterize or recognize them in that specific area. MacBeth and Schuett (2007) studied the effect of diagenesis on the compliance of natural micro-fractures. They concluded that diagenesis can decrease compliance ratio by increasing the contact area between fracture faces.

One important potential application of the compliance ratio measurement has been studied by Verdon and Wustefeld (2013). Using the S-wave splitting technique, they monitored the progress of a hydraulic fracturing treatment in the Cotton Valley tight gas reservoir in Texas. They reported notable fluctuations in compliance ratio during different stages of hydraulic fracturing stimulation. They showed that proppant injection increases compliance ratio up to a value of two, which is more than the analytical value of 1 for the compliance ratio of a single fracture in 2D. They concluded that this discrepancy can be caused by the generation of new fractures or the activation of pre-existing fractures around the main hy-

draulic fracture. In this research study, we will see that this effect can be related to slippage along the fracture that can also occur at the intersection with natural fractures.

In this study, we calculate the compliance ratio of a single fracture and show how the presence of offset or roughness on the fracture face affects compliance ratio. Fractures are considered as discontinuities in which stress is continuous along the fracture faces, but displacement may be discontinuous. Any incremental change in the stress field around the fracture produces a linear incremental change in the displacement across the fracture faces. This excess displacement is characterized by the fracture compliance. To calculate the excess displacement in our calculations in the quasi-static technique, a pair of points at the center of fracture, one at the top face and one at the bottom face, is selected when the whole system is in the initial equilibrium and no normal or tangential stress is applied. These two points initially have the same coordinates as the top point lay down on the bottom point. A 2D crack in an infinite medium, subjected to stress at infinity, has a compliance ratio of 1. In the quasi-static approach, compliance is determined as the ratio of the difference between the displacement of fractured rock and the displacement in intact rock divided by the applied stress applied at the infinite boundary. The calculation of compliance from the dynamic technique is explained in the following section.

### **2.3 Dynamic Technique to Measure Fracture Compliance**

Schoenberg (1980) derived an analytical solution for an imperfectly bonded interface in an isotropic, linear elastic medium, known as linear-slip theory. He assumed a harmonic wave of angular frequency  $\omega$  and unit amplitude passed through the fractured medium. In this model, stress along the fracture is continuous but displacement may be discontinuous. Reflection ( $R$ ) and transmission ( $T$ ) coefficients of a harmonic plane wave, with angular frequency  $\omega$ , across the imperfectly bonded interface are computed from interface compliances. In a homogenous

elastic medium with a discontinuity, reflection ( $R$ ) and transmission ( $T$ ) coefficients are:

$$R(\omega) = \frac{i\omega\rho VB}{2 + i\omega\rho VB} \quad (2.6)$$

and

$$T(\omega) = \frac{2}{2 + i\omega\rho VB} \quad (2.7)$$

where  $\rho$  is rock density,  $\omega$  is angular frequency,  $V$  is wave velocity and  $B$  is fracture compliance. For a compressional wave,  $V$  and  $B$  are equal to the compressional wave velocity and normal compliance. For a shear wave,  $V$  and  $B$  are the shear wave velocity and shear compliance.

There are differences in the amplitudes of seismic compressional and shear waves between fractured and intact rock. These differences in seismic amplitudes can be used to compute the transmission coefficient (Pyrak-Nolte *et al.*, 1987; Mollhoff *et al.*, 2010). Furthermore, the transmission coefficient can be converted into compliance by rearranging Equation (2.7). The relationship between transmission modulus and fracture compliance is shown in Equation (2.8) (Schoenberg, 1980; Mollhoff and Bean, 2009).

$$|T| = \sqrt{\frac{(\frac{2}{B\rho V})^2}{(\frac{2}{B\rho V})^2 + \omega^2}} \quad (2.8)$$

$$B = \frac{2}{\omega\rho V} \sqrt{\frac{1}{|T|^2 - 1}}$$

In this study, the transmission coefficient is calculated from the ratio between first peak amplitude in fractured rock and first peak amplitude in intact rock. These amplitudes are measured at a receiving point located beneath the fracture interface.

## 2.4 Numerical Simulation

The presence of fractures in a rock medium makes the medium more compliant and consequently increases travel times of seismic waves. The magnitude of this additional compliance depends on various parameters such as bulk modulus and viscosity of the fluid filling the fracture, host rock permeability, fracture roughness and hydraulic connectivity of fractures. This study uses the finite-element method (FEM) to investigate the effects of surface asperities and fracture offset on the fracture compliance ratio. All of the finite-element simulations are executed in ABAQUS 6.10. The quasi-static technique is utilized to determine compliance from the corresponding displacement divided by the applied stress (Figure 2.1). Compliance can be measured also from the change in the amplitude of elastic waves in the dynamic technique. This study uses the transmission coefficient technique, explained in the preceding section, to calculate the dynamic compliance from the propagation of seismic waves in a fractured rock medium. In this study, we aim to show how the compliance ratio is affected by the presence of rough asperities on the fracture surfaces as well as offset between the fracture faces. To characterize the geometry of the fracture interface, we model fracture faces as periodic saw-tooth-like structures in a Cartesian system. The idea of such a specific geometry is inspired by Aydan *et al.* (1996), who reported saw-tooth-like structures at the fracture interface of sheeting joints in granite.

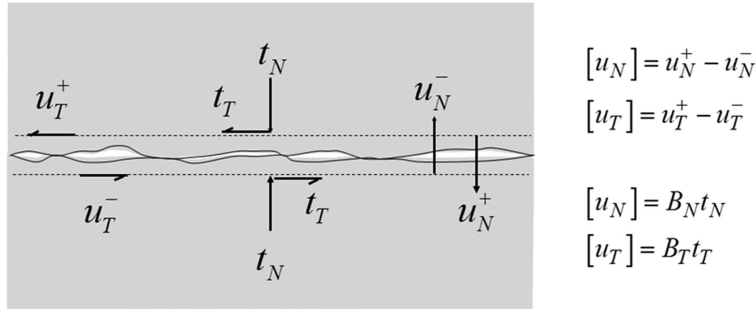


Figure 2.1: Fracture modeled as two rough surfaces in contact in the quasi-static approach. Normal and tangential displacements of the upper fracture face are denoted by  $u_N^+$  and  $u_T^+$ , and of the lower fracture face by  $u_N^-$  and  $u_T^-$ .

Numerical experiments are performed for a single fracture with a rough interface located in an infinite domain. The two tips of the one-meter-long fracture are in full contact. The infinite domain has a size of  $5000 \times 5000 \text{ m}^2$  which can be considered as an infinite domain compare to the size of the fracture as the fracture has a length of 1 m in the horizontal direction. Infinite elements at the surrounding boundaries are used to eliminate the effect of reflection from the boundaries. The 2D FEM, illustrated in Figure 2.2, is discretized adaptively to achieve the desired accuracy. Fracture roughness is modeled as saw-tooth-like structures with a single spectral component, whose wavelength is much shorter than the total length of the fracture. Each asperity on each fracture face is meshed with 10 quadrilateral quadratic elements for the quasi-static analysis; however, it is increased to 100 elements in the dynamic model per each asperity. As shown in Figure 2.2, saw-tooth-like asperities have two main angles, that are called *Asperity Angle I* and *Asperity Angle II*. These angles are defined to eliminate any ambiguity in further analysis of the numerical results. The asperity length shown in Figure 2.2 is assumed to be 1 cm. Therefore, asperity height can be adjusted by changing the asperity angles.

To improve the numerical accuracy, a refined mesh is used along the rough fracture faces to capture the high stress concentrations at the sharp corners. Friction between sliding fracture faces is simulated by the classical isotropic Coulomb friction model that considers a small sliding with a pre-defined friction coefficient. In the dynamic approach, a seismic plane wave with angular frequency of  $100 \frac{\text{rad}}{\text{s}}$  and amplitude of  $10^{-12} \text{ m}$  is transmitted at a point 0.0001 m above the fracture. The receiver point is located at 0.0001 m beneath the fracture faces. Properties of the host rock and fracture are presented in Table 2.1. It is assumed that the matrix has isotropic elastic properties.

To verify the accuracy of our numerical model, the quasi-static compliance ratio of a single smooth crack in a 2D infinite domain is compared with the analytical solution (Budiansky and O'Connell, 1976; Kachanov, 1992). The analytical solution suggests a value of 1 for the compliance ratio. The quasi-static compliance ratio obtained from our numerical model is

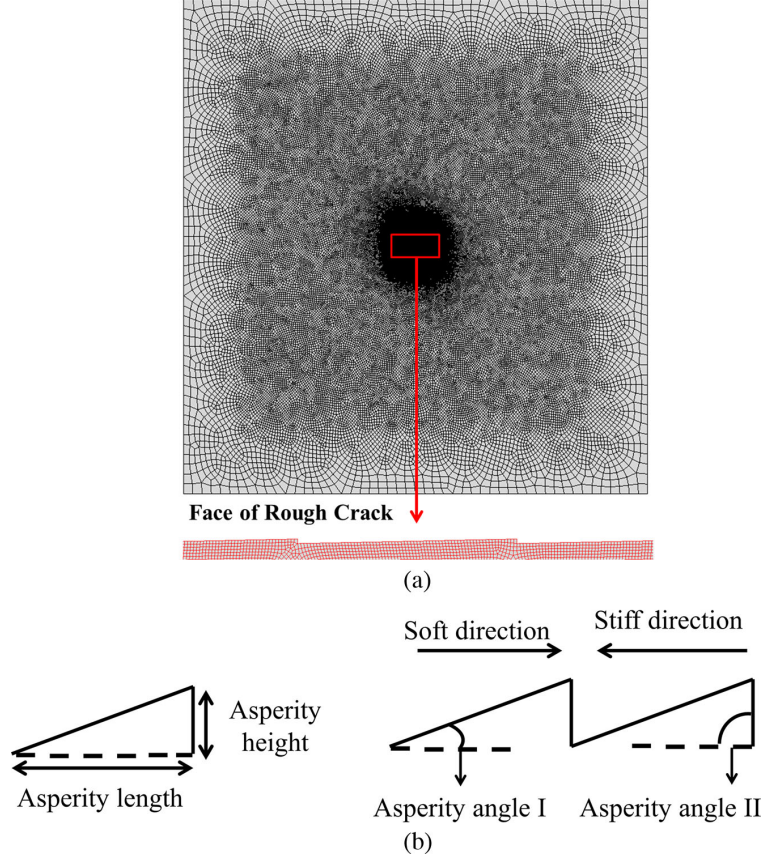


Figure 2.2: (a) 2D FEM model built to represent a rough fracture. (b) Roughness is modeled with a right-angled triangle in this specific geometry. Definition of *Soft* and *Stiff* direction derives from asymmetry of fracture surface geometry.

Table 2.1: Initial values of rock and fracture parameters.

Rock Properties	Value	Unit
Young's modulus	60	GPa
Coefficient of sliding friction	0.6	
Poisson's ratio	0.25	
Fracture length	1	m
P-wave velocity	5262.35	$\text{m.s}^{-1}$
S-wave velocity	3038.22	$\text{m.s}^{-1}$

1.0007, which is in good agreement with the analytical solution. The dynamic method gives a compliance ratio of 0.9905 for a single smooth crack located in an infinite medium.

In all of the following figures, the *soft compliance ratio* and *stiff compliance ratio* refer to the quasi-static compliance ratio in the directions shown in Figure 2.2. To calculate the normal compliance, a tensile stress is applied at the far field and then the excess displace-

ment at the center of the fracture is calculated from the difference in the displacement of corresponding points on the fracture faces. These two corresponding points are at the center of the fracture and before applying any stress sharing the same coordinates. The same procedure is followed for the shear compliance, applying a shear stress at the far field with the same magnitude as the tensile stress and measuring the excess displacements between the corresponding points at the center of the fracture. The in-plane direction in this study is considered as the reference direction as we are only interested to investigate the behavior of the fracture during its opening. Figures 2.3 to 2.10 give the quasi-static compliance ratios calculated from the stress-displacement measurements. The dynamic compliance ratio obtained from the attenuation of the transmitted seismic wave is presented in Figures 2.11 and 2.12.

## 2.5 Results and Discussion

The results of the quasi-static approach can be categorized in two different scenarios. In the first scenario, there is neither normal nor tangential offset between fracture faces, and all of the asperities on one fracture face are fully in contact with the corresponding ones on the other face. This case corresponds to Figures 2.3 to 2.5. The effect of offset and partial contact is investigated in the second scenario. The offset between fracture faces, in our study, may be either normal or tangential. The second case corresponds to Figures 2.8 to 2.10.

Interface roughness controls the degree of fracture deformation. However, the area of contact is not only a function of interface roughness, but also a function of the effective stress. In our numerical study, the differences between the compliance ratios in the soft and stiff directions may be explained by the two mechanisms of *riding up* and *interlocking* which describe the interactions of asperities under shearing (Scholz, 2002). In the riding up mechanism which is more dominant in the soft direction and for the smaller values of asperity angle  $I$ , a fracture face may ride up on the other face for the applied shear stress in soft direction. In this case, the effective friction which controls the riding up of two fracture



faces is a function of intrinsic friction and the magnitude of asperity angle I. However, interlocking mechanism is more dominant in the stiff direction and for the larger values of the asperity angle II. Based on this discussion, interlocking can provide more resistance than the purely frictional resistance manifesting in the riding up mechanism.

In Figures 2.3 and 2.4, it is assumed that fracture faces are initially perfectly matched so that there is no offset between fracture faces. Although the asperity angles in these figures are changing, the area of contact at the fracture faces is roughly constant because the size of asperities is very small and they are perfectly in contact. As a result, interlocking of asperities at the fracture faces controls the magnitude of the compliance ratios.

Figure 2.3 shows how compliance ratio varies with a change in asperity angle I if asperity angle II has a constant value of  $90^\circ$ . Asperity angle I is changing from  $0^\circ$  to  $15^\circ$ . The numerical results in Figure 2.3 are compared with the analytical solution of a single smooth crack, with no interaction at the fracture interface. The analytical solution gives a compliance ratio of 1 for a smooth crack in 2D. In reality, the assumption of extremely smooth cracks is not realistic. As discussed earlier, fractures have irregular faces and the presence of these irregularities control fracture mechanical and hydro-mechanical properties, seismicity and stress heterogeneity. Figure 2.3 shows how compliance ratio in the presence of saw-tooth-like structures at the fracture interface deviates from the value of 1 given by the analytical solution. Smaller values of asperity angle I represent fractures with smoother faces. For the values of asperity angle I close to zero, there is no difference in the compliance ratio in different shear directions as there is no preference for sliding in either of the soft or stiff directions. Therefore, the compliance ratios are independent of the direction of shear stress, and agree with the analytical solution. This agreement breaks down as asperity angle I increases, which provides more resistance against sliding. The source of this additional resistance in the stiff direction is the interlocking of opposing saw-tooth-like structures. However, the additional resistance in the soft direction may be explained by the larger frictional resistance and larger compression induced by the larger values of asperity angle

I. More resistance results in smaller displacement, which leads to lower shear compliance and higher compliance ratio. Deviation of compliance ratio from the analytical value of 1 happens in both the soft and stiff directions. However, the magnitude and onset of this deviation are different. In the soft direction, onset occurs at larger angles because the extra compression due to the rough asperities on the fracture interface can only be effective in the larger values of asperity angle I in order to increase the frictional resistance. The magnitude of the fracture compliance ratio in the soft direction is not as large as the corresponding magnitude in the stiff direction because the interlocking can provide more resistance than purely frictional resistance. Interlocking is more effective in the stiff direction as the sliding can be restrained more by the opposing fracture face.

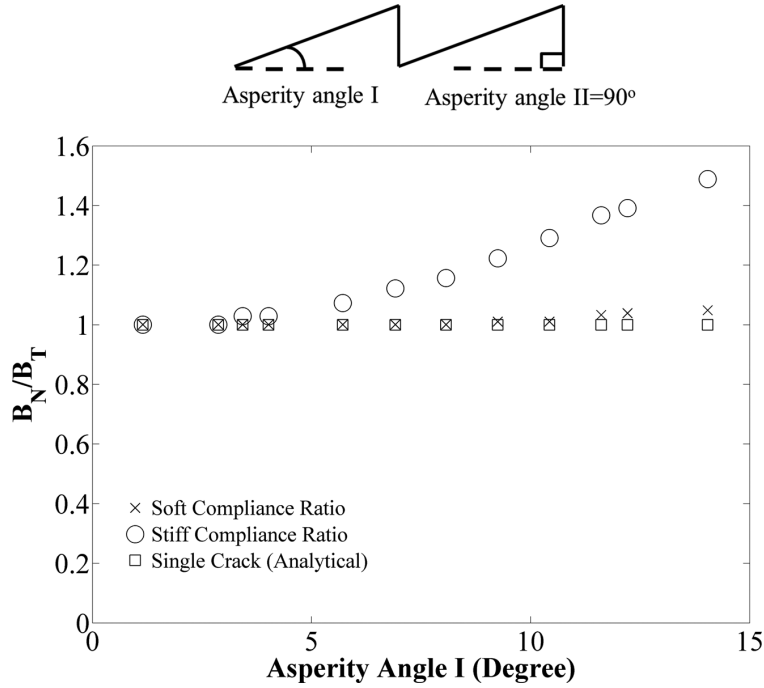


Figure 2.3: Quasi-static compliance ratio in the presence of saw-tooth-like structures at the fracture interface.

Change in the compliance ratio as a function of asperity angle II is shown in Figure 2.4, for two different values of asperity angle I. Asperity angle I is equal to  $5.71^\circ$  in Figure 2.4(a) and  $10.43^\circ$  in Figure 2.4(b). Keeping asperity angle I constant, asperity angle II varies between  $90^\circ$  and the value of asperity angle I. The deviation in compliance ratio, in

both the soft and stiff directions, reduces as asperity angle II approaches asperity angle I. It is expected that the compliance ratio will have no direction dependence if both asperity angles are equal to each other because there is no preference for sliding in either of these directions. However, the direction independence of the compliance ratio is seen to continue to larger values of asperity angle II up to around  $20^\circ$ . After passing this angle, the direction dependence of the compliance ratio becomes notable. The magnitude of the difference in the soft and stiff compliance ratio in Figure 2.4(b) is significantly larger than the difference of compliance ratios in Figure 2.4(a). We can conclude that the effects of asperity riding up and interlocking are more significant at larger values of asperity angles I and II.

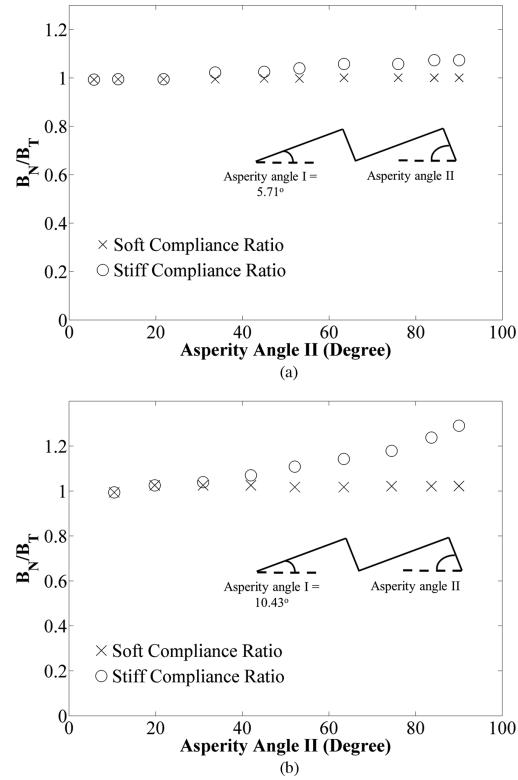


Figure 2.4: Increase in compliance ratio as a function of asperity angle II for two different values of asperity angle I. Asperity angle I is equal to  $5.71^\circ$  and  $10.43^\circ$  in (a) and (b), respectively.

As shown in Figure 2.5, the compliance ratio in the stiff direction deviates from 1 as the length of asperities increases. Keeping asperity angle and mechanical properties constant, larger size asperities have larger compliance ratio. The compliance ratio in the stiff direction

is enhanced by the stronger interlocking between opposite fracture faces due to larger asperity height.

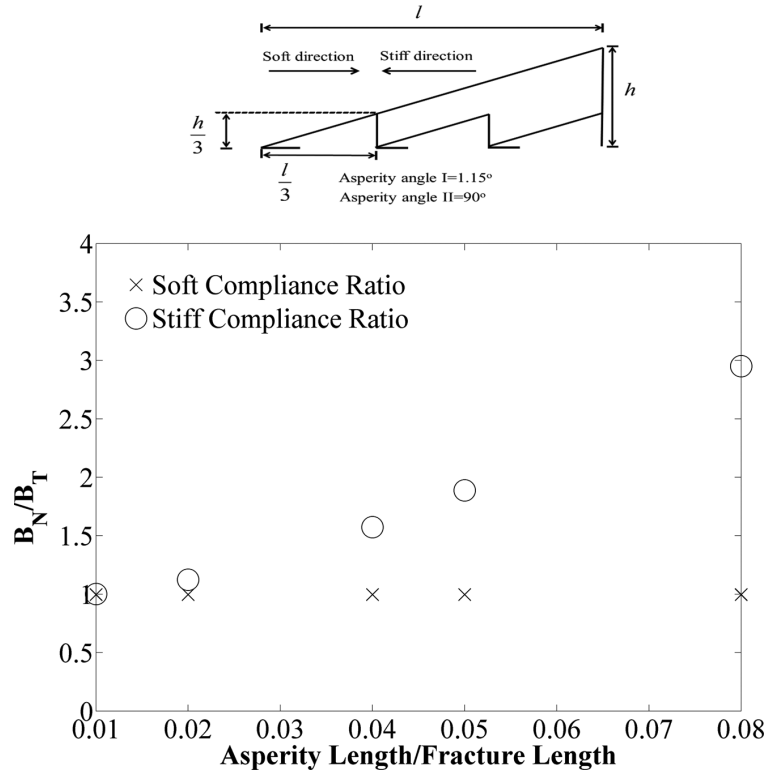


Figure 2.5: Change in compliance ratio as a function of asperity to fracture length ratio at asperity angle I of 1.15°.

This observation can be verified by looking at the magnitude of the difference in shear displacements between opposite fracture faces for various asperity sizes (Figure 2.6). To explain this finding, we may assume that each individual asperity along the fracture surface behaves like a cantilever beam with a variable height which goes to zero at the tip of each asperity (Figure 2.7). It is known that the deflection at the end of a cantilever beam is inversely proportional to the area moment of inertia of the beam's cross-section,  $I$ . The deflection at the end of a beam with a linear variable height can be calculated from Equation (2.9) where  $\omega$ ,  $a$ ,  $E$ ,  $I$ ,  $b$  and  $c$  are uniformly distributed load magnitude, beam height, Young's modulus, area moment of inertia, width and length of the beam. Considering the above equations, a single large beam with a height of  $h$  is stiffer than multiple beams (let

us say  $n$  beams) with height  $\frac{h}{n}$ , although the height summation of short beams is equal to the height of the large beam. As a result, larger asperities offer more resistance to shearing in the stiff direction leading to higher compliance ratio.

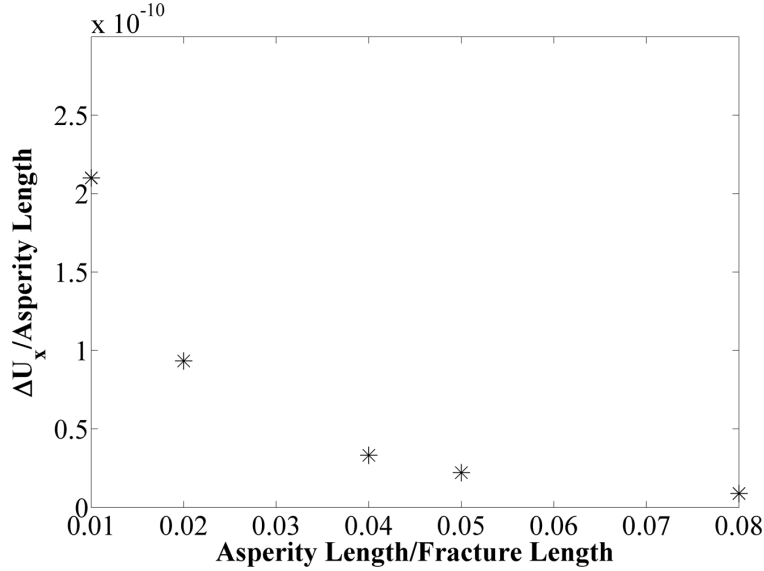


Figure 2.6: Plot of difference in shear displacement between opposite fracture faces for different asperity lengths. As the ratio of asperity length to fracture length increases, the amount of difference in shear displacement decreases which raises the compliance ratio as shown in Figure 2.5.

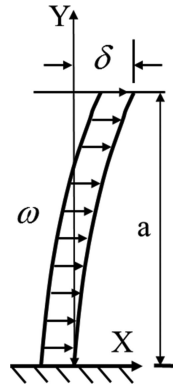


Figure 2.7: Schematic picture of a cantilever beam with a uniformly distributed load of  $\omega$ .

$$\delta = \frac{\omega a^4}{8EI} \tag{2.9}$$

$$I = \frac{bc^3}{12}$$

Interlocking and riding up effects are more effective where there is no offset between opposing fracture faces. Offset between the fracture faces allows such deformation to occur, and is discussed next. Figures 2.8 to 2.10 show the effect of different offset configurations, normal, tangential and partially in contact, respectively.

Figure 2.8 shows that the compliance ratio in the presence of normal offset is constant and there is no preferential direction dependence as the heights of asperities in this study is very small. The horizontal axis in Figure 2.8 shows the percentage of contact between asperity heights of the two fracture faces.

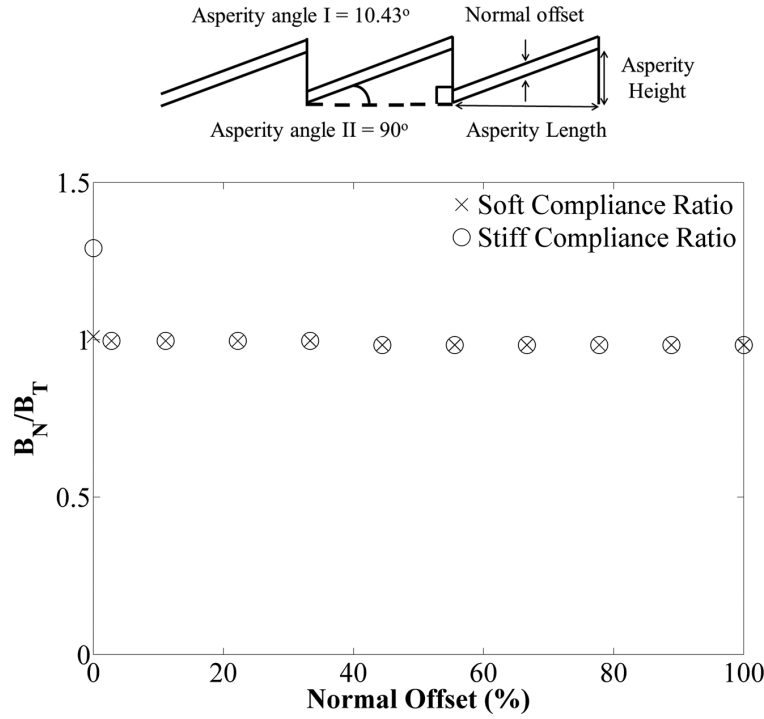


Figure 2.8: For normal offset, there is no preferential dependence on direction. The horizontal axis shows the percentage of contact between asperities of the two fracture faces. Zero percent normal offset means asperity heights are fully in contact and there is no gap between two fracture faces.

Zero percent normal offset means asperity heights are in full contact and there is no gap between the two fracture faces. By shifting one of the fracture faces upward, a normal gap is created at the fracture interface. For instance, at a normal offset of 50 percent, only half of the asperity height of each fracture face overlap, and a normal offset of 100 percent

means there is no contact between fracture faces. There is no variation in compliance ratio as normal offset changes. Small normal offset at fracture faces reduces the effect of riding up and interlocking at the fracture faces and the amount of shear displacement of the two faces is similar in the two different shear directions. Another reason for this behavior relates to the ratio of asperity length to asperity height in our simulation. The height of asperities in this figure is at least five times smaller than the asperity length. Therefore, the change in normal offset does not significantly change the area of contact. However, it is shown in Figures 2.9 and 2.10 that a change in area of contact can significantly affect compliance ratio.

In Figure 2.9, we assume that one of the fracture faces moves in a tangential direction to create tangential offset at the fracture interface.

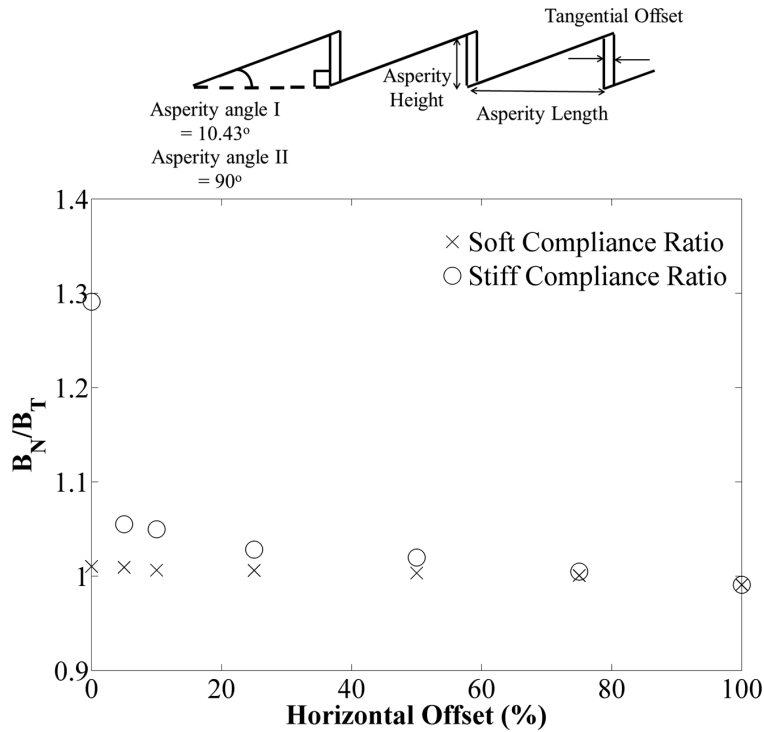


Figure 2.9: Change in compliance ratio with tangential offset due to the top fracture face sliding to the right to make a gap between the fracture faces.

As tangential offset increases, the available contact area between the inclined face of one asperity with the inclined face of the corresponding asperity on the other fracture face reduces. The increase in tangential offset continues until there is no overlap between fracture

faces at 100 percent horizontal offset. Figure 2.9 shows that the reduction in overlap at the contacts reduces the difference in the compliance ratio between soft and stiff directions. Overlap reduction continues up to the point that there is no contact at the fracture interface, after which the compliance ratio in the soft and stiff directions are equal to each other, resulting in no preferential direction dependence.

For imperfectly mated fracture surfaces, asperities present on the fracture interface are not fully in contact. In other words, only some of the asperities will be interlocked with the corresponding asperities on the other fracture face. The effect of imperfect contact area at the fracture interface is shown in Figure 2.10.

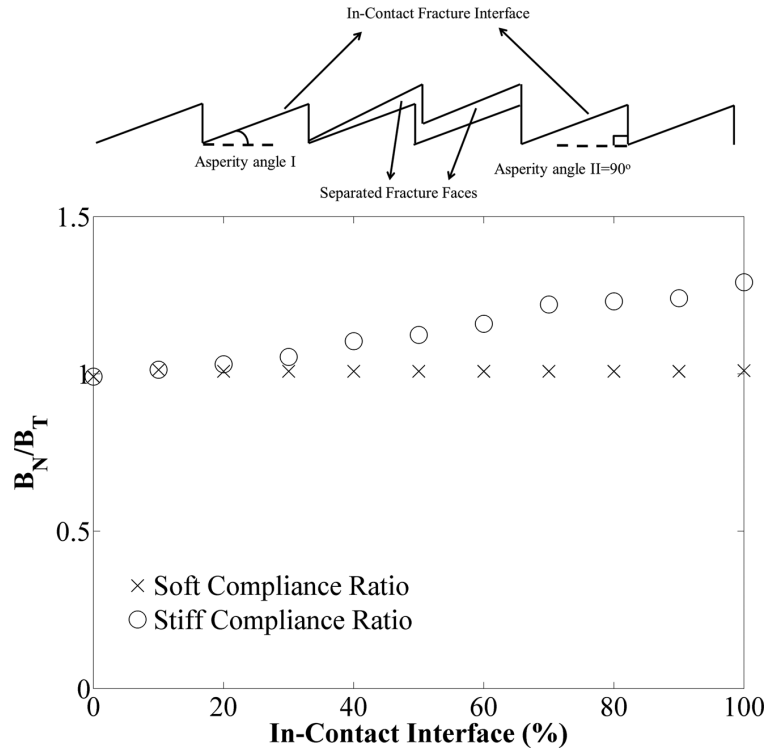


Figure 2.10: Change in compliance ratio when fracture faces are partially in contact. The abscissa shows the fraction of asperities that are in full contact. Zero percent contact means all of the asperities in one face are separated from the corresponding ones on the other face.

The abscissa of Figure 2.10 gives the fraction of asperities that are fully in contact at the fracture interface. Zero per cent means all of the asperities on one fracture face are separated from the corresponding ones on the other fracture face. Compliance ratio at this condition is



equal to the compliance ratio of dry or gas-filled fractures. With an increase in the percentage of contact between the fracture faces, the deviation in compliance ratio between soft and stiff direction increases. The largest difference happens when all of the asperities are fully in contact. Figure 2.10 demonstrates that the compliance ratio is a function of the number of in-contact faces along the fracture interface. An increase in the number of in-contact faces magnifies the compliance ratio discrepancy by increasing the effects of riding up and interlocking.

The numerical results of Figures 2.3 to 2.10 can be compared with the analytical solution for a fracture with in-contact faces of Yoshioka and Scholz (1989a) and Yoshioka and Scholz (1989b). Yoshioka and Scholz derived analytical solutions for normal and shear compliance of imperfectly bonded fracture faces. They used the distribution of local Hertzian spheres to mimic in-contact fracture faces. They assumed a no-slip condition in their solution. In their model, fracture faces are under compressive stress, leading to closure of the fracture. These sphere-made fracture faces provides smoother fracture interfaces compare to the saw-tooth structures considered in this study and observed in the field. Based on their assumptions, Yoshioka and Scholz concluded that the compliance ratio in imperfectly bonded interfaces only depends on Poisson's ratio, shown in Equation (2.10). This equation does not predict the direction dependence of the compliance ratio for imperfectly bonded fracture faces subject to a tensile stress and underestimates the compliance ratio. This formula shows that the compliance ratio equals 0.3043 for a Poisson's ratio of 0.25, which is significantly smaller than the ratios obtained in this study.

$$\frac{B_N}{B_T} = 0.71 \frac{1 - \nu}{2 - \nu} \quad (2.10)$$

Fracture compliance can be derived from either the quasi-static or dynamic technique. As mentioned above, stress–displacement measurements determine compliance in the quasi-static technique. Fracture compliance can be also derived from the change in properties of

an elastic wave such as waveform amplitude or delays in seismic arrival time. The time-delay technique is applicable if either a repeatable source with predefined amplitude or a receiving point ahead of the crack is not available. However, both of these parameters can be obtained in our numerical study. Therefore, we use the transmission coefficient technique to measure fracture compliance. Figure 2.11 shows how the waveform amplitude of a seismic wave is attenuated by the presence of a smooth fracture. The solid line in Figure 2.11 shows the amplitude of a compressional seismic wave at the receiver in intact rock, while the dashed line is the waveform amplitude in the presence of a fracture. The attenuation in displacement amplitude is used to calculate the transmission modulus. This can be converted to compliance, as explained in Equation (2.8).

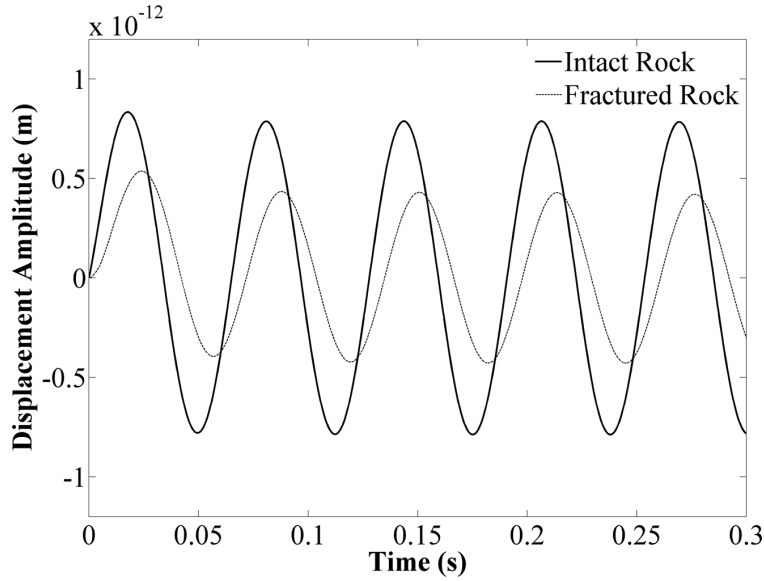


Figure 2.11: This figure shows how a waveform amplitude of a seismic wave is attenuated by the presence of a smooth fracture. The solid line shows the amplitude of a compressional seismic wave at the receiver in intact rock, while the dashed line is the waveform amplitude in the presence of a fracture.

Figure 2.12 shows how dynamic compliance ratio varies with the change in asperity angle I if asperity angle II has a constant value of  $90^\circ$ . The numerical results of Figure 2.12 are compared with the single crack analytical solution in 2D. The analytical solution suggests a compliance ratio of 1 for a smooth crack. Figure 2.12 suggests larger compliance ratios

than the analytical solution since the presence of saw-tooth-like structures at a fracture interface increases the effect of riding up and interlocking at the fracture faces. Compared to the quasi-static compliance ratio, the dynamic compliance ratio has a weak dependence on the value of asperity angle  $I$ . A possible reason for this observation may be related to the wavelength of the seismic wave compared to the size of the asperities. The wavelength of a seismic wave is significantly larger than the size of the saw-tooth-like asperities in our study.

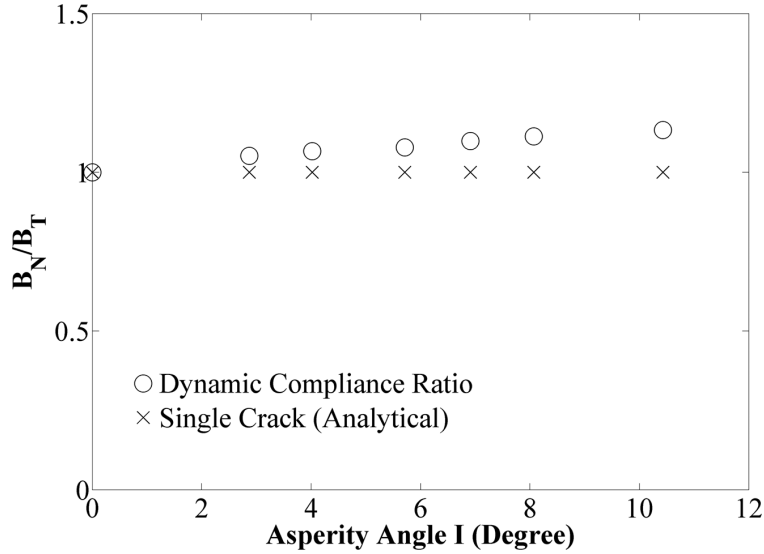


Figure 2.12: Numerical results for dynamic measurements are compared with the single crack analytical solution presented in Equation (2.5). The dynamic compliance ratio increases slightly with an incremental increase in asperity angle.

## 2.6 Conclusions

The ratio of normal-to-shear compliance can be used for reservoir characterization and depletion optimization. As extensively discussed in the literature, this ratio is sensitive to fracture roughness, type of the fluid filling the fracture, fluid viscosity, rock permeability, fracture connectivity and the presence of cement, clay and other fracture fillings. Fracture faces always consist of asperities and morphological irregularities. It is shown in the literature that the degree of contact between the fracture faces controls fluid flow and electrical current as well as fracture mechanical properties. Fracture roughness in the form of asper-

ities might be generated during joint formation or faulting. These features on the surface of fractures can affect measured compliance ratios. In this study, we employ quasi-static and dynamic approaches to investigate the effects of contact area and interface offset on the fracture compliance ratio. We study different geometrical and offset configurations to show how compliance ratio is a function of available contact area at the fracture interface and also the size of the asperities. For a single smooth crack in a tensile stress in a 2D infinite medium, the compliance ratio equals to 1. However, our study shows that compliance ratio increases to values more than 1 if the fracture has rough faces. The interlocking of asperities on fracture faces can significantly influence the compliance ratio in the stiff direction. The deviation in the compliance ratio for the soft direction from 1, suggested by the analytical solution for a single smooth crack, can be explained by the riding up effect. It is notable that interlocking is not the only parameter governing the interaction between rough fracture faces. The contact area between the fracture faces is also controlled by effective stress that affects the excess of compliance ratio, as shown in Figures 2.8 to 2.10.

## 2.7 References

- Ahmadi, M., A. Dahi Taleghani, and C. M. Sayers. "Direction dependence of fracture compliance induced by slickensides." *Geophysics* 79, no. 4 (2014): C91-C96.
- Aydan, O., Y. Shimizu, and T. Kawamoto. "The anisotropy of surface morphology and shear strength characteristics of rock discontinuities and its evaluation." *NARMS* 96 (1996): 1391-1398.
- Bachrach, R. "Recent advances in the characterization of unconventional reservoirs with wide-azimuth seismic data." *Unconventional Resources Technology Conference (URTEC)*, (2013).
- Barton, N. "Rock quality, seismic velocity, attenuation and anisotropy." CRC press, (2007).
- Bedayat, H., and A. Dahi Taleghani. "Anisotropic Inhomogeneous Poroelastic Inclusions: With Application to Underground Energy-Related Problems." *Journal of Energy Resources Technology* 138, no. 3 (2016): 032905.
- Boadu, F. K., and L. T. Long. "Effects of fractures on seismic-wave velocity and attenuation." *Geophysical Journal International* 127, no. 1 (1996): 86-110.

- Brown, S. R. "Transport of fluid and electric current through a single fracture." *Journal of Geophysical Research: Solid Earth* 94, no. B7 (1989): 9429-9438.
- Budiansky, B., and R. J. O'Connell. "Elastic moduli of a cracked solid." *International Journal of Solids and Structures* 12, no. 2 (1976): 81-97.
- Candela, Th., F. Renard, M. Bouchon, A. Brouste, D. Marsan, J. Schmittbuhl, and Ch. Voisin. "Characterization of fault roughness at various scales: Implications of three-dimensional high resolution topography measurements." *Pure and Applied Geophysics* 166, no. 10-11 (2009): 1817-1851.
- Durney, D. W, and J. G. Ramsay. "Incremental strains measured by syntectonic crystal growths." *Gravity and tectonics* 67 (1973): 96.
- Gale, J. FW, R. M. Reed, and J. Holder. "Natural fractures in the Barnett Shale and their importance for hydraulic fracture treatments." *AAPG bulletin* 91, no. 4 (2007): 603-622.
- Hobday, C., and M. H. Worthington. "Field measurements of normal and shear fracture compliance." *Geophysical Prospecting* 60, no. 3 (2012): 488-499.
- Hudson, J. A., E. Liu, and S. Crampin. "The mechanical properties of materials with interconnected cracks and pores." *Geophysical Journal International* 124, no. 1 (1996): 105-112.
- Kachanov, M. "Effective elastic properties of cracked solids: critical review of some basic concepts." *Applied Mechanics Reviews* 45, no. 8 (1992): 304-335.
- Laubach, S., R. Marrett, and J. Olson. "New directions in fracture characterization." *The Leading Edge* 19, no. 7 (2000): 704-711.
- Leucci, G., and L. De Giorgi. "Experimental studies on the effects of fracture on the P and S wave velocity propagation in sedimentary rock." *Engineering Geology* 84, no. 3 (2006): 130-142.
- Liu, E. "Effects of fracture aperture and roughness on hydraulic and mechanical properties of rocks: implication of seismic characterization of fractured reservoirs." *Journal of Geophysics and Engineering* 2, no. 1 (2005): 38.
- Liu, E., J. H. Queen, X. Y. Li, M. Chapman, S. Maultzsch, H. B. Lynn, and E. M. Chesnokov. "Observation and analysis of frequency-dependent anisotropy from a multicomponent VSP at Bluebell-Altamont field, Utah." *Journal of Applied Geophysics* 54, no. 3 (2003): 319-333.
- Lubbe, R., J. Sothcott, M. H. Worthington, and C. McCann. "Laboratory estimates of normal and shear fracture compliance." *Geophysical Prospecting* 56, no. 2 (2008): 239-247.
- MacBeth, C., and H. Schuett. "The stress dependent elastic properties of thermally induced microfractures in aeolian Rotliegend sandstone." *Geophysical Prospecting* 55, no. 3 (2007): 323-332.

- Maultzsch, S., M. Chapman, E. Liu, and X. Y. Li. "Modelling frequencydependent seismic anisotropy in fluidsaturated rock with aligned fractures: implication of fracture size estimation from anisotropic measurements." *Geophysical Prospecting* 51, no. 5 (2003): 381-392.
- Mollhoff, M., and Ch. J. Bean. "Validation of elastic wave measurements of rock fracture compliance using numerical discrete particle simulations." *Geophysical Prospecting* 57, no. 5 (2009): 883-895.
- Mollhoff, M., C. J. Bean, and P. G. Meredith. "Rock fracture compliance derived from time delays of elastic waves." *Geophysical Prospecting* 58, no. 6 (2010): 1111-1122.
- Nagy, P. B. "Ultrasonic classification of imperfect interfaces." *Journal of Nondestructive evaluation* 11, no. 3-4 (1992): 127-139.
- Narr, W., D. W. Schechter, and L. B. Thompson. "Naturally fractured reservoir characterization." Richardson, TX: Society of Petroleum Engineers, (2006).
- Nelson, R. "Geologic analysis of naturally fractured reservoirs." Gulf Professional Publishing, (2001).
- Olson, J. E., S. E. Laubach, and R. H. Lander. "Natural fracture characterization in tight gas sandstones: Integrating mechanics and diagenesis." *AAPG bulletin* 93, no. 11 (2009): 1535-1549.
- Paterson, M. S. "Experimental deformation and faulting in Wombeyan marble." *Geological Society of America Bulletin* 69, no. 4 (1958): 465-476.
- Power, W. L., T. E. Tullis, and J. D. Weeks. "Roughness and wear during brittle faulting." *Journal of Geophysical Research: Solid Earth* 93, no. B12 (1988): 15268-15278.
- Pyrak-Nolte, L. J., L. R. Myer, and N. G. W. Cook. "Seismic visibility of fractures". 28th US Symposium, June (1987), Arizona, USA, pp. 4756.
- PyrakNolte, L. J., L. R. Myer, and N. GW. Cook. "Transmission of seismic waves across single natural fractures." *Journal of Geophysical Research: Solid Earth* 95, no. B6 (1990): 8617-8638.
- Reiss, L. H. "The reservoir engineering aspects of fractured formations." Vol. 3. Editions Technip, (1980).
- Rubino, J., T. M. Mller, M. Milani, and K. Holliger. "Seismic attenuation and velocity dispersion in fractured rocks: The role played by fracture contact areas." *Geophysical Prospecting* 62, no. 6 (2014): 1278-1296.
- Sagy, A., E. E. Brodsky, and G. J. Axen. "Evolution of fault-surface roughness with slip." *Geology* 35, no. 3 (2007): 283-286.
- Sayers, C. M. "Seismic characterization of reservoirs containing multiple fracture sets." *Geophysical Prospecting* 57, no. 2 (2009): 187-192.

- Sayers, C. M., and M. Kachanov. "A simple technique for finding effective elastic constants of cracked solids for arbitrary crack orientation statistics." *International Journal of Solids and Structures* 27, no. 6 (1991): 671-680.
- Sayers, C. M., and M. Kachanov. "Microcrackinduced elastic wave anisotropy of brittle rocks." *Journal of Geophysical Research: Solid Earth* 100, no. B3 (1995): 4149-4156.
- Sayers, C. M., A. Dahi Taleghani, and J. Adachi. "The effect of mineralization on the ratio of normal to tangential compliance of fractures." *Geophysical Prospecting* 57, no. 3 (2009): 439-446.
- Schoenberg, M. "Elastic wave behavior across linear slip interfaces." *The Journal of the Acoustical Society of America* 68, no. 5 (1980): 1516-1521.
- Schoenberg, M., and C. M. Sayers. "Seismic anisotropy of fractured rock." *Geophysics* 60, no. 1 (1995): 204-211.
- Scholz, Ch. H. "The mechanics of earthquakes and faulting." Cambridge university press, (2002).
- Verdon, J. P., and A. Wustefeld. "Measurement of the normal/tangential fracture compliance ratio (ZN/ZT) during hydraulic fracture stimulation using Swave splitting data." *Geophysical Prospecting* 61, no. s1 (2013): 461-475.
- Van Dam, D. B., and C. J. de Pater. "Roughness of hydraulic fractures: The importance of in-situ stress and tip processes." In *SPE Annual Technical Conference and Exhibition*. Society of Petroleum Engineers, (1999).
- Yoshioka, N., and Ch. H. Scholz. "Elastic properties of contacting surfaces under normal and shear loads, 1, Theory." *Journal of Geophysics. Res* 94, no. B12 (1989): 17681-17690.
- Yoshioka, N., and Ch. H. Scholz. "Elastic properties of contacting surfaces under normal and shear loads: 2. Comparison of theory with experiment." *Journal of Geophysical Research: Solid Earth* 94, no. B12 (1989): 17691-17700.

# Chapter 3

## Impact of Thermally Reactivated Micro-Natural Fractures on Well Productivity in Shale Reservoirs

### 3.1 Introduction

Hydraulic fracturing treatments have played a crucial role in boosting hydrocarbon production from low permeability reservoirs. Induced fractures significantly improve wellbore-formation contact area and consequently increase the production rate. Injection of highly pressurized fracturing fluid fractures the formation to create a highly permeable conduit for the reservoir fluid to produce. The direction of hydraulic fracture propagation depends on the direction of the minimum principal stress as well as natural fractures (Economides and Nolte, 2000; Dahi Taleghani and Olson, 2011). Core and outcrop studies, advanced logging tools, microseismic techniques and well testing analysis have proved the existence of natural fractures in many unconventional reservoirs. In naturally fractured reservoirs, arrest and diversion of hydraulic fracture front into the pre-existing natural fractures have been the subject of many experimental and theoretical studies (Warpinski and Teufel, 2010; Potluri *et al.*, 2005; Dahi Taleghani *et al.*, 2013; Gonzalez *et al.*, 2015).

Natural fractures are mechanical discontinuities with the lengths varying from micrometers to kilometers (Narr *et al.*, 2006). These fractures may act as conductive paths for the fluid flow in the low permeability reservoirs affecting the ultimate recovery. However, they can also increase the leakoff volume during the fracturing treatments leading to early



screenouts or poorly propped hydraulic fractures. Contribution of natural fractures in the hydrocarbon recovery is more significant in the tight formations with low permeability than permeable reservoirs (Nelson, 2001). Existence of natural fractures in the outcrop samples could be an indicative of their existence in the subsurface; however, characterization of natural fractures in subsurface is not a trivial task. Most of the outcrop studies are qualitative and the existing models studying the interaction of natural fractures with the hydraulic fracture mainly consider the contribution of large natural fractures, i.e. fractures with the dimensions comparable to the size of hydraulic fracture, on the hydraulic fracture growth (Jeffrey *et al.*, 2009; Dahi Taleghani and Olson, 2014). However, the log-normal distribution of natural fractures, shown in Figure 3.1, demonstrates that small natural fracture exist orders of magnitudes more frequent than the large natural fractures. Hence, the role of small-size natural fractures may be as important as the large natural fractures since the small fractures exist in large numbers. Length of small natural fractures varies from micro- to centi- meter; therefore, injected proppants cannot enter inside these small fractures to keep them open.

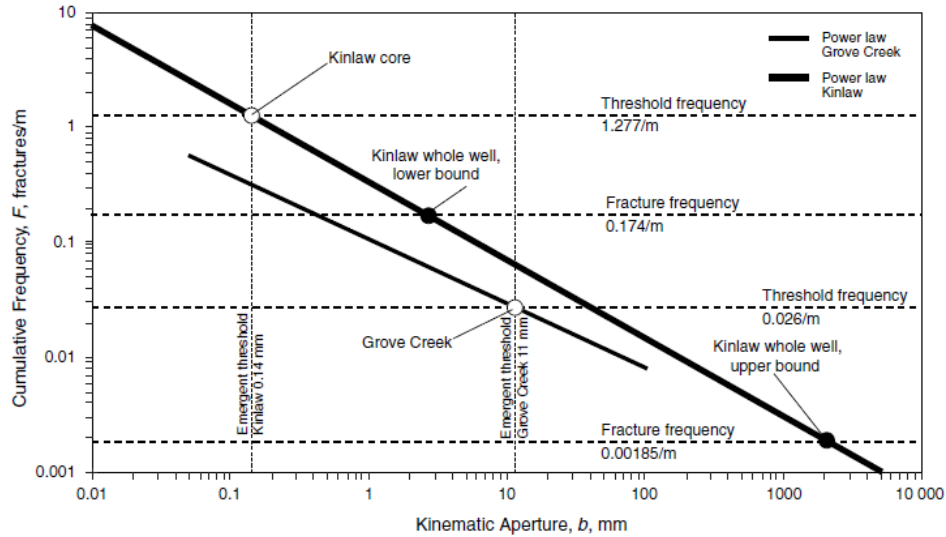


Figure 3.1: Power-law aperture-size distribution in Groove Creek and Kinlaw formations shows much larger frequency of micro-fractures in comparison to large size fractures (Plot borrowed from Gale, 2002).

In contrast to the driving force of the main hydraulic fracture, the magnitude of induced thermal stresses, only a few MPa, is not large enough to initiate new fractures in the intact rock, but it may be sufficient for opening pre-existing micro natural fractures even though they might be filled with diagenetic materials as cement bonds are typically much weaker than the intact rock. Parameters controlling the opening of these small fractures are tensile strength of cementing materials filling the fractures, temperature difference between the fracturing fluid and the formation, and microfractures' density. Induced thermal stress in a homogenous isotropic elastic half-plane due to heat conduction can be shown by the Equation (3.1) (Nemat Nasser *et al.*, 1978). The elastic half-plane is at the initial temperature of  $T_0$ ; however, temperature at its surface suddenly drops to the temperature of  $T_1$ .

$$\frac{d\sigma}{dx} = \frac{2D_T\beta_s(T_0 - T_1)}{3\sqrt{\pi}} \exp^{-\left(\frac{x\sqrt{3}}{\delta}\right)^2} \quad (3.1)$$

$$\delta = \left(\frac{tk}{\rho C}\right)^{0.5}$$

where  $D_T$ ,  $\beta$ ,  $k$ ,  $\rho$ ,  $C$ , and  $t$  are tangent constitutive tensor, volumetric thermal expansion coefficient, thermal conductivity, density, specific heat capacity, and time.  $\delta$  is a length scale where a specific temperature gradient has been formed. Rock thermal failure due to injection/circulation of cold water into the brittle hot rocks is a known phenomenon (Perkins and Gonzalez, 1985). The effect of temperature changes in stress redistribution and consequently fracture opening is mainly studied in hot dry geothermal reservoirs rather than hydrocarbon reservoirs. For instance, Zhou *et al.* (2010) have only considered thermal fracture initiation in a homogeneous rock. In a reservoir with multiple natural fracture sets, stress shadow effect of neighbor cracks may lead to competition or arrest of advancing cracks. Opening of small fractures in large numbers may significantly improve well productivity by increasing fracture-formation contact area and rock overall permeability. Since the fracturing fluid is injected at the ambient temperature at the surface and it has a high velocity in the tubing, its temperature is lower than the reservoir temperature when it first get exposed to

the surface of hydraulic fracture. This temperature difference induces tensile stress on the surface of hydraulic fracture. If the induced stress exceeds the tensile strength of cementitious materials filling the natural fractures, natural fracture will be opened. The required energy to open small natural fractures is smaller than the energy required for opening large natural fractures. Temperature gradient as the driving force for thermal failure is a function of parameters like injection rate, tubing size, fracture width and length. This study aims to quantitatively estimate the impact of the opening of small pre-existing natural fractures, activated by the induced thermal stress and their contribution in the hydrocarbon recovery.

### 3.2 Natural Fractures Characterization

Fractures are discontinuities formed to alleviate the excessive pore pressure or stress in the rock mass with possibly self-affine or fractal structures like the fracture pattern shown in Figure 3.2. Natural fractures can make significant heterogeneity in the permeability and cause anisotropy in the rock strength. Natural fractures distribution covers a wide range of scales from kilometers in lineaments to micrometers in microfractures and is characterized by their length, aperture, and density attributes. There are several ways to obtain a better understanding of fractures pattern in the subsurface like outcrop observations, production data, reservoir cores and image logs (Narr *et al.*, 2006). Among these methods, outcrop samples are the most direct way to study natural fractures. Natural fractures may be recognized in the drilling phase due to considerable mud loss or bit chatting and bit drops, or in the early stages of production, causing heterogeneity in the production data and productivity index. Natural fracture characterization may also be achieved by integration of microseismic data, well log, treatment data and production history which involved more complicated workflow (Puyang *et al.*, 2015).

Natural fractures are important as they can act as pre-existing weak paths for fracture network development. Open natural fractures increase reservoir overall permeability and consequently the hydrocarbon production. However, fully cemented fractures may act as



Figure 3.2: Distribution of natural fractures in flagstones, Caithness, Scotland. (Source: Mike Norton, Wikipedia)

barriers against the fluid flow. Degree of cementation in natural fractures depends on the burial depth at the time of fracturing and its history after fracturing, mineralogy of host rock and its fluid chemistry (Gale, 2002). Field studies suggest that fractures with small apertures, i.e. less than a critical threshold, are probably fully filled with mineralized materials (Laubach, 2003), further geochemical analyses have confirmed these findings in other formations (for instance see Olson *et al.*, 2009). These diagenetic minerals can be calcite, dolomite or quartz. Figure 3.3 shows a broken face of natural fractures sealed with calcite recovered from Barnett shale. Compositions of cementing materials and its formation conditions have crucial impacts on mechanical strength of the cemented fracture. If the cementing materials inside the natural fracture are stiffer than the host rock, they absorb larger portion of the applied stress in comparison to the host rock; therefore, it is not surprising that the interface of the cement and the host rock is the first spot for failure occurrence. Some lab measurements in the Barnett shale suggests that the digenetic materials filling the fracture have tensile strength about 10 times lower than the tensile strength of the rock matrix (Gale *et al.*, 2007). To predict the impact of natural fractures on the well productivity, a comprehensive knowledge about the natural fractures population, its cement properties, and in-situ stresses is required.

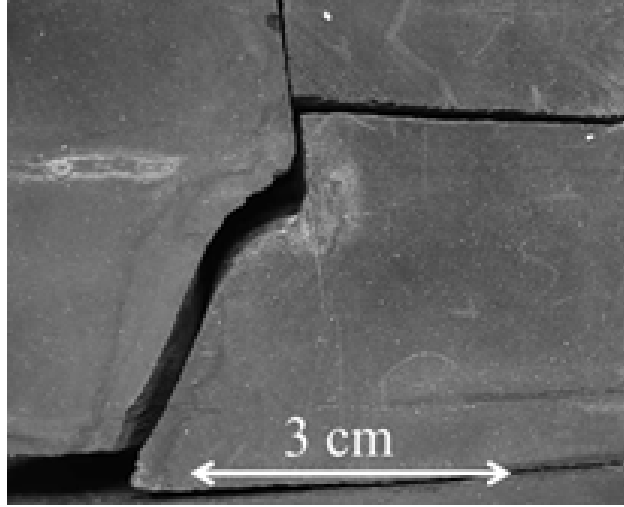


Figure 3.3: Broken surface of natural fractures sealed with calcite in Barnett Shale. (Borrowed from Gale *et al.*, 2007)

### 3.3 Natural Fractures Characterization

Linear elastic fracture mechanics (LEFM) is a powerful tool to model fracture behavior in brittle rocks, however, it fails to predict fracture propagation in soft rocks. Lack of capability to predict fracture initiation is another drawback of LEFM. Cohesive zone method (CZM) is a substitute theory for LEFM to study fracture behaviors without the described limitations. Cohesive zone model can predict fracture initiation and propagation in brittle, ductile, and cemented materials. Dugdale (1960) and Barenblatt (1962) introduced the theory of cohesive zones to incorporate material inelastic behavior at the fracture tips. In the cohesive zone model, Barenblatt assumed that molecular cohesive forces create a non-linear bonding zone at the crack tip while tensile strength and cohesive toughness control the damage of these bonds. This technique removes the stress singularity at fracture tips by introducing cohesive forces to address one of the main drawbacks of LEFM.

Elices *et al.* (2002) discussed the advantages and limitations of the CZM in a review paper. A significant limitation in CZM is the pre-defined path for fracture propagation which requires that the pre-defined path supporting rock failure should be known or dynamically

adjusted in the simulation. Cohesive failure occurs in three phases: initiation, evolution, and removal of the cohesive zone at the complete failure, shown in Figure 3.4.

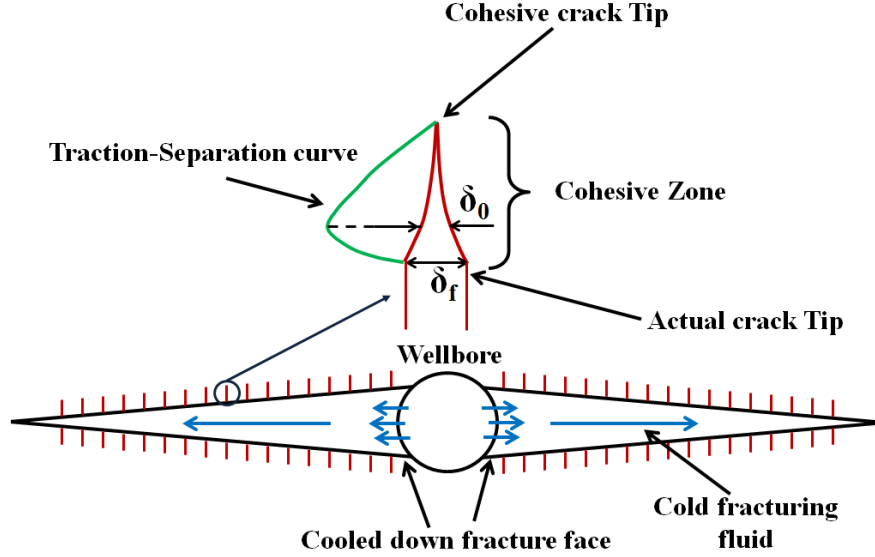


Figure 3.4: Schematic picture of natural fracture modeled cohesive zone method. Cohesive failure occurs in three phases: initiation, evolution, and removal of the cohesive zone at the complete failure.

Cohesive degradation represents fracture initiation. Stress-strain relationship in cohesive zones is described by traction-separation laws (TSL). The bilinear TSL, shown in Figure 3.5, is used in this study. This cohesive law assumes linear behavior before reaching the maximum tensile strength of the cohesive zone. Damage initiates if separation of the faces in the cohesive zone reaches the critical value  $\delta_0$  which is called the critical separation point. Beyond this point, the degradation of cohesive element further develops as the complete failure happens at  $\delta_f$  where the cohesive forces are gone and fracture propagates. Slope of the elastic segment and the area of traction-separation curve are known as cohesive stiffness and cohesive energy, respectively. Fracture initiation in the bilinear cohesive law is determined by either the critical separation point or the maximum tensile strength. Fracture propagation is controlled by the failure point,  $\delta_f$ , or the cohesive energy. Quadratic stress damage criterion, shown in Equation (3.2) is used here to predict failure initiation in cohesive elements where  $t_n$ ,  $t_s$ , and  $t_t$  are values of the normal and tangential traction stress components acting on the

cohesive zone and  $t_{n0}$ ,  $t_{s0}$ , and  $t_{t0}$  represent the cohesive maximum tensile strength values in the principal directions of the failure plane. Failure initiates if summation of these ratios becomes equal or greater than one i.e.

$$\left\{\frac{t_n}{t_{n0}}\right\}^2 + \left\{\frac{t_s}{t_{s0}}\right\}^2 + \left\{\frac{t_t}{t_{t0}}\right\}^2 = 1 \quad (3.2)$$

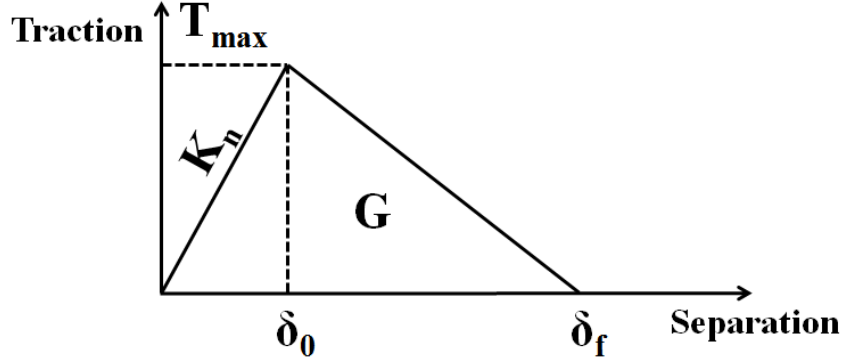


Figure 3.5: Bilinear traction-separation law. Opening is equal to the  $\delta_0$  at the maximum tensile strength. Complete failure happens at the  $\delta_f$  where traction-separation law is no longer valid.

### 3.4 Semicircular Bending Test

Extensive laboratory studies have shown that cohesive zone models can better describe the inherent nonlinear nature of interfacial fractures in granular materials. The main challenge in using cohesive models is choosing, or being more precise, measuring cohesive model parameters in the lab. Semicircular bending test (SCBT) is a laboratory experiment that determines when the rock will fail when under a particular applied force. Sierra *et al.* (2010) performed a semicircular bending test for the Woodford shale samples to monitor fracture initiation-propagation, and to measure the Woodford shale mechanical properties. Based on these tests, he suggests that fracture roughness of the Upper Woodford shale is higher than fracture toughness of the middle and the lower Woodford shale. Percentage of clay

content has significant impact on the magnitude of fracture toughness in the Woodford shale samples. Kerogen saturation also affects the rock mechanical properties and consequently rock failure in the shale reservoirs (Abousleiman *et al.*, 2016). Kerogen acts like a binding glue which can significantly affect the stress-strain curve in shale reservoirs. Abousleiman experimental works are shown that the kerogen can significantly increase the rock tensile strength in the micro-scale.

This study uses the load-displacement curve of the Woodford shale samples, measured by Sierra *et al.* (2010), to inversely calculate the stiffness, strength, and energy of cohesive elements for our following numerical models. Indicated cohesive parameters are measured by matching the experimental load-displacement curve with the curve obtained from the numerical simulation of this test, shown in Figure 3.6.

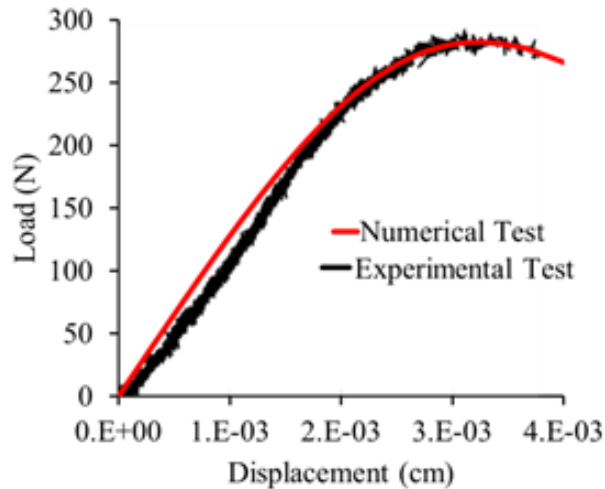


Figure 3.6: Match of experimental semicircular bending test, obtained from the Sierra *et al.* (2010), with the numerical semicircular bending test. Numerical experiment uses cohesive interface theory to model fracture initiation-propagation.

Table 3.1 presents the CZM parameters obtained from matching numerical and experimental works. It is notable that these parameters are dependent on the size of cohesive elements. If the size of cohesive element changes, the cohesive parameters needs to be adjusted as they are scale dependent. Small size of the cohesive element in the numerical simulation imposes significant computational cost especially for large models. To overcome



this problem, one may increase size of the initial model and then the cohesive path in the upscaled model is meshed once with small cohesive element size and again with large cohesive element size. Both models are supposed to generate same loading curves as shown in Figure 3.7.

Table 3.1: Cohesive properties used in the numerical simulation

Parameter	Value	Unit
Cohesive strength	2.325	MPa
Cohesive stiffness	75	GPa
Cohesive energy	10	Pa.m
Cohesive element size	0.0005	m

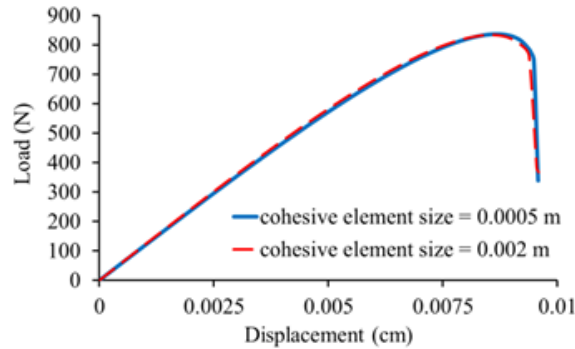


Figure 3.7: The match of numerical upscaled semicircular bending tests with two different cohesive element sizes. The cohesive properties of the case with four-time larger cohesive elements are adjusted in a way to have the similar loading-displacement curve with the one with smaller cohesive elements.

### 3.5 Results and Discussion

In hydraulic fracturing treatments, cold fracturing fluid reduces the bottomhole temperature, and generates tensile stress on the surface of hydraulic fractures. If this stress is larger than the tensile strength of cementing material inside the natural fractures, it may open these pre-existing fractures. Nemat Nasser *et al.* (1978) discussed how induced thermal stress can initiate parallel cracks with uniform spacing in a homogenous plate. These induced cracks do not grow at the same rate. They initially propagate at the same rate before reaching

a critical state. At the critical state, some of the cracks stop propagating while the rest propagate faster. This critical state is determined by the stress shadow of neighbor cracks. This process continues until there is no more energy in the system to be released. Similar scenario may happen for opening of pre-existing natural fractures.

The geometry in Figure 3.8 is used for finite element analysis of thermal reactivation of microcracks.

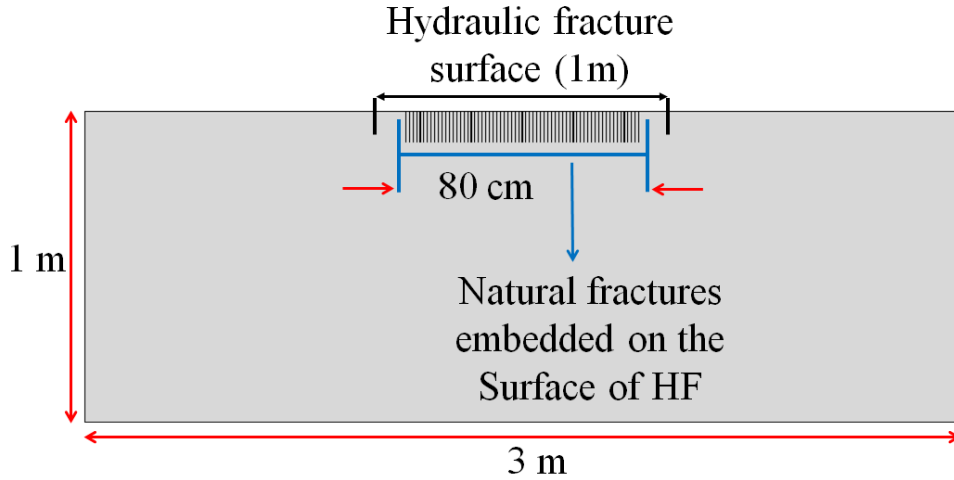


Figure 3.8: The two dimensional model representing a mosaic frame of hydraulic fracture with natural fractures embedded on the surface of hydraulic fracture. Cohesive interface theory models opening of natural fractures.

For the sake of simplicity and reducing the computational cost, a small frame of the hydraulic fracture with the intersecting natural fractures is selected for modeling by ABAQUS. Due to symmetry of the fracture, only one surface of the hydraulic fracture is modeled here. Pre-existing cemented fractures are assumed to be vertical and perpendicular to the surface of the hydraulic fracture modeled with CZM. The cohesive-modeled fractures have the length of 10 cm. All of the boundaries are constrained for normal displacement except the surface of the hydraulic fracture. At  $t < t_0$ , the formation and embedded natural fractures are at initial formation temperature  $T_0$ . However, at time  $t \geq t_0$ , temperature at the free surface of the hydraulic fracture for a time period of 100 seconds is linearly reduced to a pre-defined temperature which is  $100^\circ\text{C}$  less than initial formation temperature. A summary of rock

mechanical properties and cohesive zone properties are listed in Table 3.2. Cohesive and rock properties are from the Woodford Shale formation (Sierra *et al.*, 2010; Abousleiman *et al.*, 2007).

Table 3.2: Properties of cemented natural fractures and intact rock

Property	Value	Unit
Rock Density	2500	Kg.m <sup>-3</sup>
Rock Young's modulus	14	GPa
Poisson's ratio	0.2	
Thermal expansion coefficient	$15 \times 10^{-6}$	°C <sup>-1</sup>
Rock conductivity	0.1	W.m <sup>-1</sup> .K <sup>-1</sup>
Rock specific heat capacity	1000	J.Kg <sup>-1</sup> .K <sup>-1</sup>
Cohesive strength	2.265	MPa
Cohesive stiffness	75	GPa
Cohesive energy	100	Pa.m
Cohesive element size	0.2	cm
Reservoir temperature	163	° C
In-situ stress	3.7	MPa

In the primary numerical example, crack spacing is 1.25 cm and the rock matrix with cohesive elements properties listed in Table 3.2. Temperature at the surface of the hydraulic fracture is linearly reduced to 63 °C over 100 seconds. Simultaneously, the surface of the hydraulic fracture goes under linear loading and unloading. The maximum fluid net pressure is assumed to be 20 MPa. Figure 3.9 shows the temperature profile along the cohesive path after 50 and 100 seconds. Sharp temperature gradient at the hydraulic fracture surface induces tensile stress on the natural fractures. The right axis in Figure 3.10 illustrates SDEG of cohesive elements along the cohesive path versus crack length. However, the left axis shows the opening of cemented cracks along the reactivated length. SDEG is the scalar stiffness degradation of the cohesive zone with a range from 0 to 1. This variable defines the magnitude of cohesive stiffness degradation once the damage in the cohesive interface has been initiated. SEDG of 1 means complete failure of the cohesive interface. The selected cracks in Figure 3.10 have the longest and shortest length of reactivation in the primary numerical example. This figure suggests that the crack with the longer length has the larger

opening. However, Figure 3.11 shows that cumulative frequency of longer cracks is lower than the frequency of shorter ones. Cumulative frequency represents the total number of cracks with apertures equal or larger than a specific size. In Figure 3.11, apertures are measured at the surface of hydraulic fracture in which the maximum induced stress is available to open the cracks.

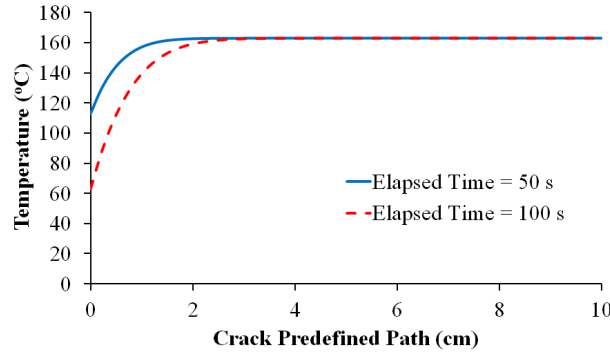


Figure 3.9: Temperature distributions along the cohesive interface after 50 and 100 seconds. Minimum Temperature happens at the intersection of natural and hydraulic fracture.

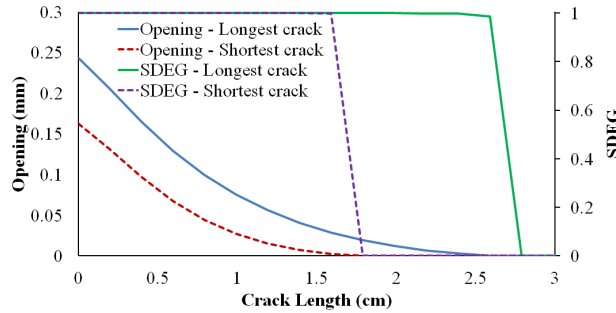


Figure 3.10: Crack length vs. crack opening after 100 seconds for the longest and shortest cracks in the primary numerical example. Right vertical axis represents the cohesive interface SDEG which is the scalar stiffness degradation of cohesive interface with a range from 0 to 1. SDEG of 1 shows the complete failure of cohesive element.

Magnitude of temperature difference can affect total length of induced cracks since the larger temperature difference provides more energy for cracking. Figure 3.12 depicts the influence of fracturing-fluid-formation temperature difference on the activated length of cracks. This figure shows that for the same cumulative frequency, larger temperature difference re-activates larger crack by feeding more energy to the system to induce cracking.

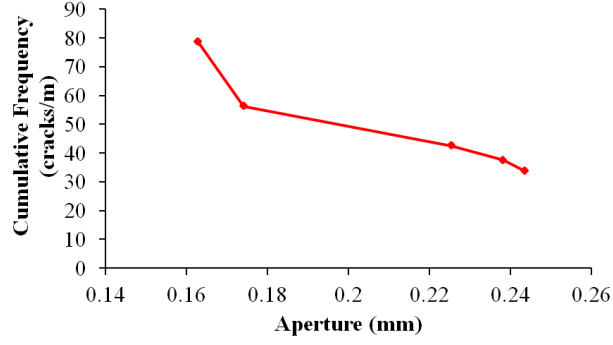


Figure 3.11: Aperture-size distribution after elapsed time of 100 s for the primary numerical example. Aperture is measured at the surface of hydraulic fracture where cemented cracks cross the surface of hydraulic fracture.

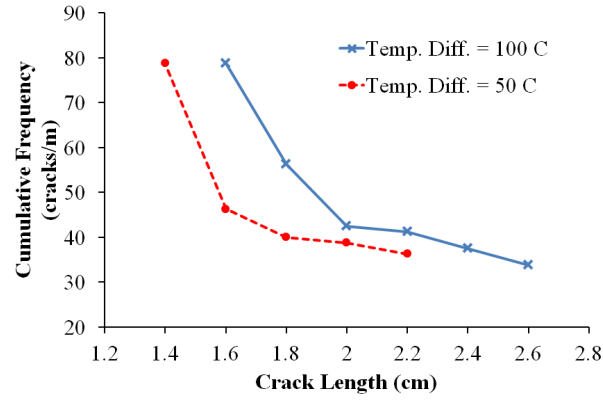


Figure 3.12: Length-size distribution after elapsed time of 100 s for the spacing of 1.25 cm, and temperature differences of 100 °C and 50 °C at the end of elapsed time.

Conductivity of shales at the ambient conditions varies from 0.5 to  $2.2 \frac{w}{m.K}$  (Gilliam and Morgan, 1987). Figure 3.13 shows the role of rock conductivity on the activated cracks lengths. This figure suggests if thermal conductivity is very low, it is more expected that all of the activated cracks have more uniform length. This observation may be explained by the importance of thermal conductivity on the heat transfer. Rock thermal conductivity dictates the rate of heat transfer in the system. Lower formation thermal conductivity results in less heat transfer across the formation and lower available energy for the crack propagation. The magnitude of available energy for the thermal conductivity of  $1 \frac{w}{m.K}$ , or smaller than 1, is not large enough to overcome the critical energy to induce non-uniform cracking.

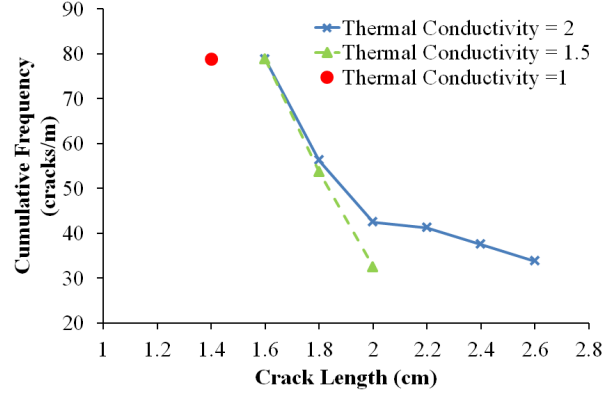


Figure 3.13: Length-size distribution for three shale thermal conductivities. If the rock thermal conductivity is very low, it is more expected that all of the activated cracks have more uniform length.

Natural fractures can show different resistance against opening. This resistance depends on the diagenetic materials filling the natural fractures and the degree of cementation. Natural fractures filled with the materials with smaller tensile strength are easier to be opened. Tensile strength of cementitious materials can affect the cohesive properties. Figure 3.14 pictures the crack-length distribution of natural fractures with two different cohesive properties.

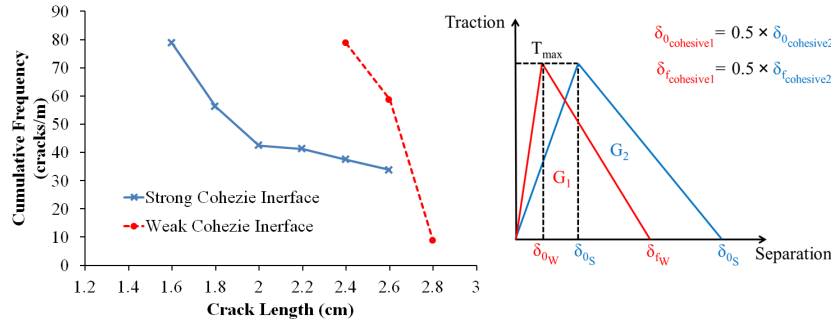


Figure 3.14: Length-size distribution for two cohesive interfaces after elapsed time of 100 s. Critical separation and critical failure points of the weaker cohesive interface are half of their values for the stronger interface.

Critical separation and critical failure points of the weaker cohesive interface are half-time smaller than their values for the stronger interface. This figure shows that the minimum length of activated cracks in the weaker interface is significantly larger than the minimum in the stronger interface. The available energy to induce cracking in both of these cases

is the same. However, the weaker interface experiences the damage and complete failure faster than the stronger interface. Since the amount of energy is required to damage the weaker interface is smaller than the stronger interface and both of the systems have the same amount of energy available to induce cracking, the extra energy in the model with the weaker interface is consumed to increase the crack length.

Fracture spacing can affect the length and width of activated fractures. Figure 3.15 and 3.16 show the average crack length and width at different spacings.

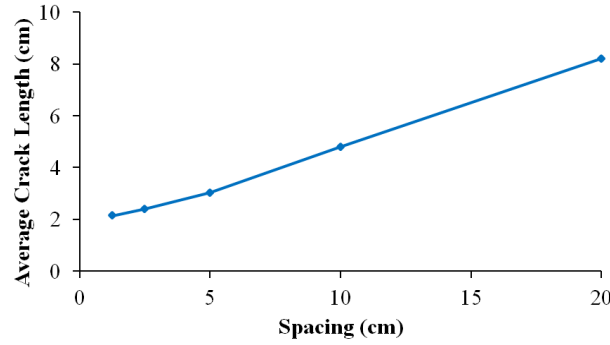


Figure 3.15: Average crack length at different cracks spacings. In small spacings, a crack should first overcome the imposed stress by the neighbouring cracks which equals to less available energy to propagate deeper.

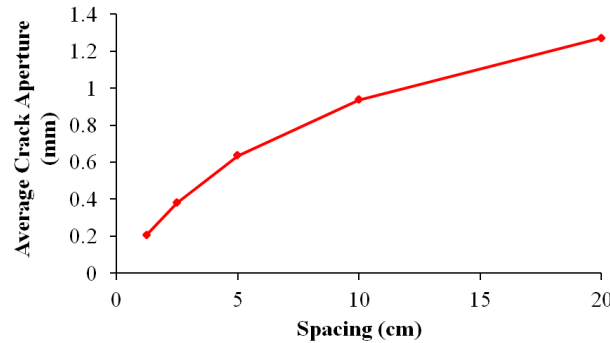


Figure 3.16: Average crack width at different cracks spacings after elapsed time of 100. Stress shadow effect leads to narrower cracks.

These figures suggest the stress shadow effect of neighboring cracks can affect both the length and width of reactivated cracks. For small spacings, a crack should first overcome the extra stress imposed by the neighboring cracks which mean less amount of energy is available to

propagate deeper and wider. At larger spacings, the induced stress field of neighboring cracks is less effective on the adjacent cracks growth and the activated cracks have more uniform distribution.

Reactivated microcracks, as shown in Figure 3.17, increase the formation-fracture contact area as well as the rock permeability along the fracture. However, these microfractures can have a negative effect during hydraulic fracturing by increasing the leak-off rate due to the capillary effect. These fractures, as shown in this study, have very small width which favors the capillary trapping of based-water fracturing fluids.

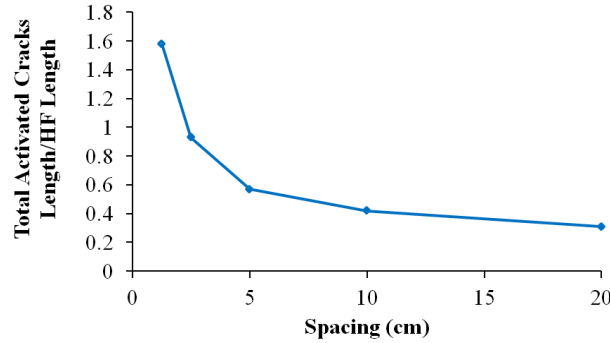


Figure 3.17: Total reactivated cracks length per length of hydraulic. Total activated cracks length is equal to the cumulative length of activated cracks lengths for a specific cracks spacing.

Effect of these activated microfractures can be considered in the calculation of equivalent wellbore radius and skin factor. In the equivalent wellbore radius, the inflow surface areas only include inflow areas of wellbore and hydraulic fracture. However, hydraulic fracture inflow area can be modified to include the microcracks inflow area as well as pictured in Figure 3.18. Equation (3.3) describes the revised version of equivalent wellbore radius for the natural fractures where  $r'_w$ ,  $x_f$ ,  $x_{nf}$ ,  $h_f$ , and  $h$  are equivalent wellbore radius, hydraulic fracture length, cumulative length of activated natural fractures, average natural fractures height, and reservoir height (Economides *et al.*, 2012). The positive sign in Equation (3.3) considers the favorable effect of reactivated microfractures; however, the negative sign shows the effect of capillary trapping on the effectiveness of induced hydraulic fracture. Capillary



trapping and extra leak-off cause early screenouts which reduce the propped fracture width and decrease the treatment efficiency. The equation of Folds of Increase in the hydrocarbon production, shown in Equation (3.4), can be calculated with the revised value of equivalent wellbore radius where  $r_e$  and  $r_w$  are reservoir and wellbore radius. This method does not consider the effect of enhanced permeability and microfractures widths in the calculation. Therefore, it is more realistic to modify the transmissibility coefficient in the dual porosity-permeability model to include contribution of natural fractures.

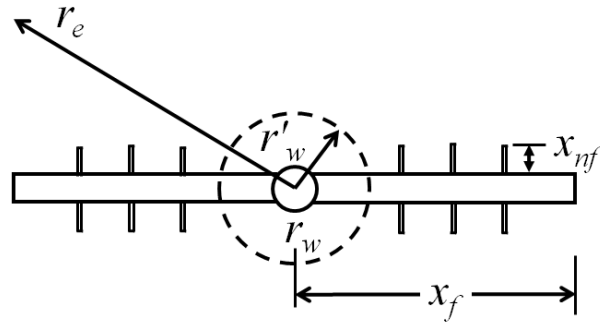


Figure 3.18: Schematic picture of equivalent wellbore radius including the wellbore inflow area, hydraulic fracture inflow area and activated natural microcracks inflow area.

$$r'_w = 0.6x_f \pm 0.6 \frac{x_{nf}h_f}{h} \quad (3.3)$$

$$FOI_{ps} = \frac{\ln\left(\frac{r_e}{r_w}\right) - 0.75}{\ln\left(\frac{r_e}{r'_w}\right) - 0.75} \quad (3.4)$$

In dual porosity model, porous media include two distinct volumes, rock matrix with the large storage capacity and low flowing capacity and fracture with lower storage capacity and high flowing capacity. Barenblatt (1962) introduced the Equation (3.5) for the single-phase fluid flow in the rock matrix and fracture where  $K$ ,  $P$ ,  $C$ ,  $\mu$ , and  $S$  are permeability,

pressure, compressibility, viscosity, and fracture-formation contact area. The subscripts of 1 and 2 refer to matrix and fracture, respectively. Natural fractures can affect the variable  $S$  by enhancing fracture-formation contact area. Opened natural fractures may also improve the reservoir permeability for the areas nearby the hydraulic fracture. Barenblatt in his equations did not consider effects of fracture and rock compressibilities.

$$\begin{aligned}\frac{K_1}{\mu} \nabla P_1 &= \Phi_1 C_1 \frac{\partial P_1}{\partial t} - \varphi_1 \frac{\partial P_2}{\partial t} + \frac{SK_1}{\mu} (P_1 - P_2) \\ \frac{K_2}{\mu} \nabla P_2 &= \Phi_2 C_2 \frac{\partial P_2}{\partial t} - \varphi_2 \frac{\partial P_1}{\partial t} + \frac{SK_2}{\mu} (P_1 - P_2)\end{aligned}\tag{3.5}$$

Kazemi *et al.* (1976) enhanced Barenblatt's work to account for the multiphase systems, shown in Equation (3.6) in which  $B$ ,  $g$ ,  $K$ ,  $K_r$ ,  $P$ ,  $q$ ,  $S$ ,  $t$ ,  $D$ ,  $\mu$ ,  $\rho$ ,  $\phi$ ,  $\tau$ ,  $f$ ,  $m$ , and  $\alpha$  are formation volume factor, gravitational acceleration, permeability, relative permeability, pressure, production/injection rate, saturation, time, depth, viscosity, density, porosity, transfer function, fracture, matrix and phase, respectively. Their model considers the effects of gravity force, relative fluid mobilities, imbibition and variation in reservoir properties and they used a transfer function to couple the matrix fluid flow with the fracture fluid flow.

$$\begin{aligned}\nabla \lambda_{\alpha f} (\nabla P_{\alpha f} - \rho_{\alpha} g \nabla D) &= \frac{\partial}{\partial t} \left( \frac{\phi S_{\alpha}}{B_{\alpha}} \right) + q_{\alpha f} + \tau_{\alpha m-f} \\ \tau_{\alpha m-f} &= \frac{\partial}{\partial t} \left( \frac{\phi S_{\alpha}}{B_{\alpha}} \right)_m \\ \lambda_{\alpha f} &= \frac{K_{r_{\alpha f}} K_f}{\mu_{\alpha} B_{\alpha}}\end{aligned}\tag{3.6}$$

To account for the influence of natural fractures in Kazemi's formulation, one can adjust their transmissibility coefficient which is the ratio of effective permeability to fluid viscosity and formation volume factor. In vicinity of the hydraulic fracture, formation transmissibility should be a weighted average of matrix and natural fractures transmissibilities, as shown in Equation (3.7) where  $\lambda$ ,  $L$ , and  $w$  are transmissibility, length, and width. Subscripts  $RM$

and  $NF$  refer to rock matrix and natural fracture. Figure 3.19 illustrates the schematic picture of a reservoir block including rock matrix and reactivated natural fractures. This modified transmissibility coefficient, considering the effect of natural fractures, can be used for areas in the vicinity of hydraulic fracture.

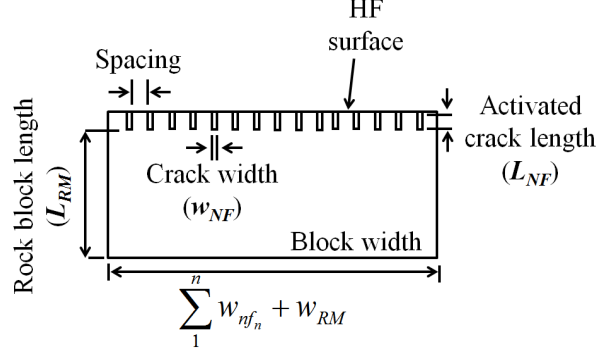


Figure 3.19: Schematic picture of a reservoir block including rock matrix and reactivated natural fractures.

$$K_{NF} = \frac{w_{NF}^2}{12}$$

$$\bar{\lambda} = \frac{\frac{L_{NF} + L_{RM}}{L_{NF}}}{\frac{\sum_1^N w_{NF_n} \lambda_{NF} + w_{RM} \lambda_{RM}}{\sum_1^N w_{NF_n} + w_{RM}}} + \frac{L_{RM}}{\lambda_{RM}} \quad (3.7)$$

In the low permeable shale reservoirs, hydrocarbon production from the hydraulic fractures and natural fractures dictates the economic success of a well. To illustrate effect of micro-natural fractures in hydrocarbon production, the cumulative gas production in a hydraulically fractured shale reservoir, having a horizontal well, can be compared for two different scenarios where the reactivated cracks either do or do not cross the surface of hydraulic fracture. In this reservoir simulation, effect of capillary trapping is ignored for the sake of simplicity, and it is assumed that all of the reactivated natural fractures boost fluid flow from the reservoir into the wellbore. As it is shown in Figure 3.10, crack opening reduces with crack length. To determine cracks length and width in the reservoir simulation, it is

assumed that all of the cracks have once apertures equal to the shortest crack aperture shown in Figure 3.10. Then to measure the average crack length, the area of crack opening-length diagram in Figure 3.10 can be compared for the shortest crack and divide it by the related aperture. This means that all of the reactivated fractures in the reservoir simulation have the width of 0.163 mm and length of 0.48 cm. The reservoir volume for gas production from the assumed shale reservoir is equal to 23-acre  $\times$  270-ft. Effect of natural fractures is modeled by the modified transmissibility coefficient ratio. Equation (3.7) suggests a modified transmissibility ratio of 2.17 for the hydraulic fracture by considering the contribution of natural fractures. Table 3.3 lists the properties of the shale gas reservoir as well as the horizontal well. Commercial reservoir simulator, CMG, is used to model the gas production from this reservoir (CMG GEM, 2015). Due to the limited number of grids cells available for numerical simulation in our version of CMG, it is assumed that one hydraulic fracture crosses middle of the horizontal well.

Table 3.3: Properties of gas reservoir

Property	Value	Unit
Matrix prosity	0.03	
Matrix permeability	$10^{-4}$	md
Langmuir adsorption constant ( $\text{CH}_4$ )	0.002	$\text{psi}^{-1}$
Maximal adsorbed mass ( $\text{CH}_4$ )	0.1	$\text{gmole.lb}^{-1}$
Rock density	120	$\text{lb.ft}^{-1}$
Hydraulic fracture permeability	10000	md
Propped hydraulic fracture width	0.00833	ft
Hydraulic fracture half-length	350	ft
Hydraulic fracture height	210	ft
Average natural fracture length	0.0157	ft
Average natural fracture width	0.000534	ft
Natural fractures spacing	0.041	ft
Rock compressibility	$10^{-6}$	$\text{psi}^{-1}$
Initial pressure	2500	psi
Bottom-hole pressure	500	psi
Length of horizontal well	550	ft

Figure 3.20 shows the increase in cumulative gas production after one year and five years of production. Figure 3.21 illustrates the percentage of increase in production during 5

years. These figures suggest that natural fractures are significantly effective at early stage of production. This observation is due to small formation permeability which restricts the rate of hydrocarbon drainage from the reservoir into the natural fractures and hydraulic fracture after fractures are fully drained. The magnitude of difference in cumulative production in Figure 3.21, for the cases with and without effect of natural fractures, is only for the indicated reactivation length of natural fractures in this study. In reality, the reactivated length of natural fractures may be larger than what we calculate in this study. For instance, the calculated parameters for the cohesive interface are representative of the shale rocks and not completely the cemented materials inside the natural fractures in the shale reservoirs. It is shown that cemented materials filling the natural fractures have lower strength than the host rock (Gale *et al.*, 2007). Therefore, crack in the cemented materials propagates faster with deeper penetration than in the host rock. In the reservoir simulation, only one hydraulic fracture crosses the horizontal wellbore in this study. However in a real fracturing treatment, 15 to 25 hydraulic fractures are connected to the horizontal wellbore which means our rough estimate for increase in cumulative production in Figure 3.20 can be at least one order of magnitude larger.

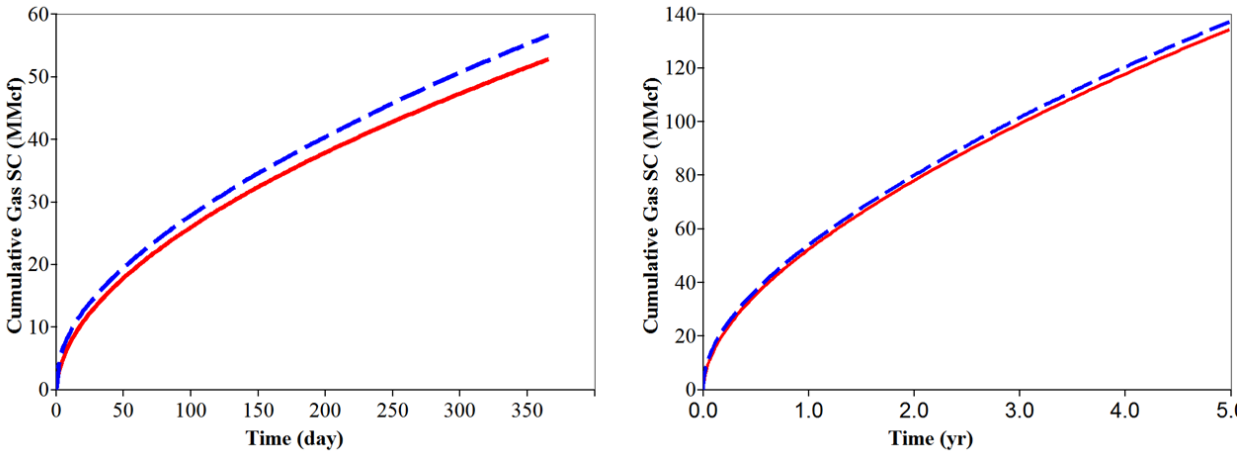


Figure 3.20: Cumulative gas production after 1 year, left figure, and 5 five years, right figure.

Reactivated natural fractures, as shown in Figures 3.20 and 3.21, can improve the fluid recovery in the shale reservoirs. However, these small opened cracks can act like a two

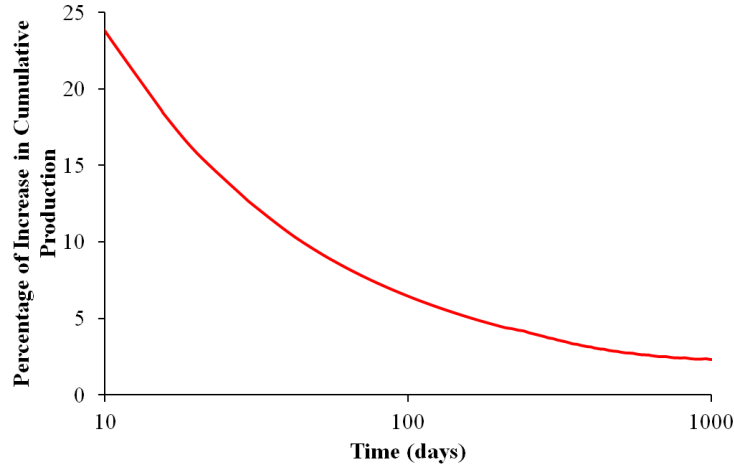


Figure 3.21: Percentage of increase in cumulative gas production during 5 years in a semi-log graph.

edged swords. Some of the hydraulic fracturing treatments use water as the based fluid for fracturing fluid. In water wet formations, since the width of reactivated cracks, as shown in Figures 3.10 and 3.16, are significantly small, capillary pressure for these cracks can be large enough to suck in the fracturing fluid and trap it inside the natural fractures. The reservoir pressure at the early stages of production can push out the trapped water inside the reactivated natural fractures; however, during production as the water cut increases along with drop in the reservoir pressure below the capillary pressure, a significant drop in the hydrocarbon production is expected as the produced water will be trapped inside the reactivated natural fractures.

### 3.6 Conclusion

Considerable temperature difference between fracturing fluid and reservoir would induce thermal tensile stress on the surface of the hydraulic fracture. The induced tensile stresses may open cemented natural fractures, improving the formation-fracture contact area as well as enhancing the rock permeability in the vicinity of the hydraulic fracture. Most of natural fractures are much smaller than the hydraulic fracture; however, their presence in large population can have a considerable impact on production. Right after stimulation, these natural

fractures are drained by the drive of reservoir pressure. As production continues and water cut increases, the water is being trapped in these natural fractures (capillary trapping) and act as barrier against gas production. Cohesive interface theory has been utilized here to model reactivation of natural fractures due to induced thermal stresses. Semicircular bending test of the Woodford shale samples are used to derive cohesive properties required for numerical simulations. This study suggests that the length and width of reactivated length depends on the spacing of natural fractures, rock thermal conductivity, temperature difference between fracturing fluid and reservoir, as well as the strength of diagenetic materials filling natural fractures. Larger natural fracture spacing results in longer and more uniform activated cracks since the stress shadow effect diminishes as fracture spacing increases. Injecting a colder fracturing fluid into a reservoir with larger thermal conductivity increases the length of reactivated fractures. The impact of reactivated natural fractures can be translated into transmissibility coefficient of the hydraulic fracture to incorporate their impact on permeability enhancement near fractures.

### 3.7 References

- Abousleiman, Y. N., M. H. Tran, S. Hoang, C. P. Bobko, A. Ortega, and F.J. Ulm. "Geomechanics field and laboratory characterization of the Woodford Shale: The next gas play." In SPE Annual Technical Conference and Exhibition. Society of Petroleum Engineers, 2007.
- Abousleiman, Y. N., K. L. Hull, Y. Han, G. Al-Muntasheri, P. Hosemann, S. Parker, and C. B. Howard. "The granular and polymer composite nature of kerogen-rich shale." *Acta Geotechnica*: 1-22, 2016.
- Barenblatt, G. I. "The mathematical theory of equilibrium cracks in brittle fracture." *Advances in applied mechanics* 7.1 (1962): 55-129.
- User's Manual for CMG GEM. Computer Modeling Group Ltd, CMG GEM. 2015: Calgary, Alberta, Canada.
- Dahi Taleghani, A., and J. Olson. "Numerical modeling of multistranded-hydraulic-fracture propagation: accounting for the interaction between induced and natural fractures." *SPE Journal* 16.3 (2011): 575-581.

- Dahi Taleghani, A., M. Ahmadi, and J. E. Olson. "Secondary Fractures and Their Potential Impacts on Hydraulic Fractures Efficiency." In ISRM International Conference for Effective and Sustainable Hydraulic Fracturing. International Society for Rock Mechanics, 2013.
- Dahi Taleghani, A., and J. E. Olson. "How natural fractures could affect hydraulic-fracture geometry." *SPE Journal* 19, no. 01 (2014): 161-171.
- Dugdale, D. S. "Yielding of steel sheets containing slits." *Journal of the Mechanics and Physics of Solids* 8.2 (1960): 100-104.
- Elices, M., G. V. Guinea, J. Gomez, and J. Planas. "The cohesive zone model: advantages, limitations and challenges." *Engineering fracture mechanics* 69, no. 2 (2002): 137-163.
- Economides, M. J. and K.G. Nolte. "Reservoir stimulation." Wiley Press, 2000.
- Economides, M. J., A. D. Hill, C. Ehlig-Economides, and D. Zhu. "Petroleum production systems." Pearson Education, 2012.
- Gale, J. FW. "Specifying lengths of horizontal wells in fractured reservoirs." *SPE Reservoir Evaluation & Engineering* 5.03 (2002): 266-272.
- Gale, J. FW, R. M. Reed, and J. Holder. "Natural fractures in the Barnett Shale and their importance for hydraulic fracture treatments." *AAPG bulletin* 91.4 (2007): 603-622.
- Gilliam, T. M., and I. L. Morgan. "Shale: Measurement of thermal properties." No. ORNL/TM-10499. Oak Ridge National Lab., TN (USA), 1987.
- Gonzalez-Chavez, M., P. Puyang, and A. Dahi Taleghani. "From semi-circular bending test to microseismic maps: an integrated modeling approach to incorporate natural fracture effects on hydraulic fracturing." *Unconventional resources technology conference, SPE*. Aug. 2015.
- Jeffrey, R., X. Zhang, and M. Thiercelin. "Hydraulic Fracture Offsetting in Naturally Fractured Reservoirs: Quantifying a Long-Recognized Process." *SPE Hydraulic Fracturing Technology Conference*. 2009.
- Kazemi, H., L. S. Merrill Jr, K. L. Porterfield, and P. R. Zeman. "Numerical simulation of water-oil flow in naturally fractured reservoirs." *Society of Petroleum Engineers Journal* 16, no. 06 (1976): 317-326.
- Kresse, O., X. Weng, H. Gu, and R. Wu. "Numerical modeling of hydraulic fractures interaction in complex naturally fractured formations." *Rock mechanics and rock engineering* 46, no. 3 (2013): 555-568.
- Laubach, S. E. "Practical approaches to identifying sealed and open fractures." *AAPG bulletin* 87.4 (2003): 561-579.
- Narr, W., D. S. Schechter, and L. B. Thompson. "Naturally fractured reservoir characterization." *Society of Petroleum Engineers*, 2006.



- Nelson, R. "Geologic analysis of naturally fractured reservoirs." Gulf Professional Publishing, 2001.
- Nemat-Nasser, S., L. M. Keer, and K. S. Parihar. "Unstable growth of thermally induced interacting cracks in brittle solids." *International Journal of Solids and Structures* 14.6 (1978): 409-430.
- Olson, J. E., S. E. Laubach, and R. H. Lander. "Natural fracture characterization in tight gas sandstones: Integrating mechanics and diagenesis." *AAPG bulletin* 93.11 (2009): 1535-1549.
- Perkins, T. K., and J. A. Gonzalez. "The effect of thermoelastic stresses on injection well fracturing." *Old SPE Journal* 25.1 (1985): 78-88.
- Potluri, N. K., D. Zhu, and A. D. Hill. "The effect of natural fractures on hydraulic fracture propagation." In *SPE European Formation Damage Conference*. Society of Petroleum Engineers, 2005.
- Puyang, P., A. Dahi Taleghani, and B. R. Sarker. "Multi-Disciplinary Data Integration for Inverse Hydraulic Fracturing Analysis: A Case Study." In *Unconventional Resources Technology Conference*. Society of Petroleum Engineers, 2015.
- Sierra, R., M. H. Tran, Y. N. Abousleiman, and R. M. Slatt. "Woodford Shale mechanical properties and the impacts of lithofacies." In *44th US Rock Mechanics Symposium and 5th US-Canada Rock Mechanics Symposium*. American Rock Mechanics Association, 2010.
- Warpinski, N. R., and L. W. Teufel. "Influence of geologic discontinuities on hydraulic fracture propagation." *Journal of Petroleum Technology* 39, no. 02 (1987): 209-220.
- Zhou, X., A. Aydin, F. Liu, and D. D. Pollard. "Numerical modeling of secondary thermal fractures in hot dry geothermal reservoirs." *Proceedings in Thirty-Fifth Workshop on Geothermal Reservoir Engineering* Stanford University, Stanford, California (2010). California.

# Chapter 4

## Thermoporoelastic Analysis of Artificially Fractured Geothermal Reservoirs; a Multiphysics Problem

### 4.1 Introduction

Geothermal energy is referred to as an attractive energy resource to address the increasing electricity demand in various parts of the world. This energy resource is derived from the decay of the radioactive materials, such as uranium, thorium, and potassium, or the stored heat in the earth core during the formation of planet Earth. This source of energy is considered renewable as the rate of temperature drop in the earth mantle is about 100 to 116°C per billion years. Armstead (1983) showed that the total heat content of the earth is in the order of  $12.6 \times 10^{24}$  MJ from which we only harvest a small portion. Geothermal energy is weather-independent compared to wind or solar energy and is environmentally friendly in comparison to the fossil fuels. Production of greenhouse gases in geothermal plants is significantly lower than fossil-fuel plants (Ulgiati and Brown, 2002). For instance, the rate of CO<sub>2</sub> emission in a geothermal power plant is 5% of a similar size coal-fired plant (Duffield and Sass, 2003). Production of electricity from geothermal resources places it third among other renewable resources. Cumulative electricity production from the geothermal reservoirs is higher than the solar and wind resources, however less than the hydroelectricity and biomass.

The first geothermal plant was established at Larderello, Italy in 1904; however, it was not commercially producing electricity until 1911. Geothermal power plant was not commercialized in the US before 1960, when the Pacific Gas and Electric initiated electricity production from the Geysers in California. Geothermal resources in the US have the capacity to supply 10 percent of current national electricity consumption by 2050 (Giardini, 2009). Williams *et al.* (2008) showed that US can economically produce 100 GWe from the enhanced geothermal systems by 2050. They discussed about how enormous amount of sustainable, clean, and affordable energy can be produced from this source in the next 25 years.

Geothermal gradient defines sustainability of the electricity production in the geothermal reservoirs. This gradient is defined as the ratio of the temperature rise with the increase in depth. An average geothermal gradient is around 25 to 30°C per kilometer. However, this average cannot be extended to everywhere on the earth. For instance, Tanaka *et al.* (2004) reported the gradient of 100°C per kilometer in some areas of Japan. In general, geothermal reservoirs are located in the regions with the gradients above the average value. These reservoirs more likely exist in the areas close to the geotectonic plate margins, where the geothermal gradient is significantly above the average gradient.

Geothermal systems generally consist of a heat source, a reservoir and a geofluid. Figure 4.1 shows a schematic picture of a geothermal system. The heat source can either be the high temperature gradient or the magmatic intrusion. The reservoir is a hot porous medium overlaid by an impermeable cap rock. Geofluid, usually water, is circulating through the reservoir by convection mechanism which transfers the heat from the larger depths to the shallow zones. The density difference between the cold and hot geofluid initiates convective mechanism as the cold geofluid at the lower depths is replaced by the hot geofluid at the higher depths. Heat source is the heart of a geothermal system. Without a heat source, heat withdrawal is meaningless. However, the circulating fluid can be artificially made; for

instance, heat withdrawal from a fissured hot dry rock by injection of the cold water into the formation.

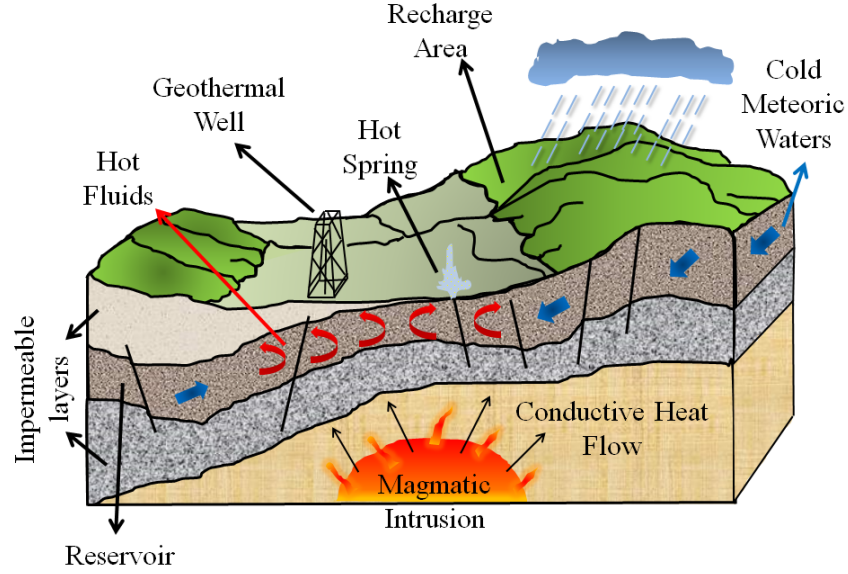


Figure 4.1: Schematic picture of a geothermal system containing heat source, geothermal reservoir, cap rock and geofluid (from Dickson and Fanelli (2013)).

Geothermal reservoirs have low, medium, or high enthalpy. Table 4.1, from Dickson and Fanelli (2013), illustrates different definitions of these reservoirs in the literature. Geothermal reservoirs can be classified by the types of the geothermal reservoirs as hydrothermal, geopressured, or hot dry rocks.

Table 4.1: Classification of low, medium and high enthalpy resources based on temperature of geothermal system (Adapted from Dickson and Fanelli (2013))

Enthalpy of Geothermal System	Temperature ( $^{\circ}\text{C}$ )			
	Muffler and Cataldi (1978)	Hochstein (1990)	Benderitter and Cormy (1990)	Nicholson (2012)
Low	$< 90$	$< 125$	$< 100$	$= 150$
Medium	$90 - 150$	$125 - 225$	$100 - 200$	—
High	$> 150$	$> 225$	$> 200$	$> 150$

Hot dry rocks are the most common geothermal resources in the world, shown in Table 4.2. In these reservoirs, there is not enough fluid in place to be used for the heat extraction.

The proposed technique in this study is suitable for the hot dry rocks with lack of fluid in place and environmental constraint for waste fluid disposal.

Table 4.2: Estimation of worldwide geothermal resources (Adapted from Armstead (1983))

	Hot Dry Rock	Geo-pressured	Hydrothermal
Energy content (EJ)	110775000	569700	137150

Lack of fluid in place in the hot dry rock reservoirs may have a significant drawback. To overcome this problem, a working fluid should be injected into the reservoir to absorb the heat, and later be produced from production wells (Rawal and Ghassemi, 2014). In this open-loop system which is an Enhanced Geothermal System (EGS), enough reservoir permeability is crucial for the project success. In a reservoir with low permeability, hydraulic fracturing treatments are performed to increase injectivity and productivity. The amount of the produced heat in this system depends on the rock temperature, rate of fluid circulation in the reservoir, and the swept volume by the injected working fluid. Loss of the working fluid, affecting total cost of the produced electricity, is a common issue. However, drawbacks are not limited to only this issue. Surface subsidence, formation compaction, induced earthquakes, and consequent damages to the wellbore integrity are other disadvantages of heat extraction from open-loop systems (Geertsma, 1973; Majer *et al.*, 2007).

## 4.2 Closed-Loop Geothermal Systems

To address the indicated issues, closed-loop geothermal system can be considered as an alternative solution. In this method, a working fluid, with low-boiling point, is circulated inside a series of coaxial sealed pipes to extract the stored heat in the reservoir. The low-boiling point improves the heat extraction efficiency (Diao *et al.*, 2004). It is expected that the lack of fluid production/injection from/into the reservoir should not significantly affect the pore pressure distribution. The closed-loop system has negligible environmental hazard compared to the open-loop system. For instance, produced water in an open-loop system

contains high levels of sulfur, salt, and radioactive elements. Therefore, extracted water should be injected back into the reservoir which is a costly process (Kagel *et al.*, 2005). Land subsidence is another drawback in the open-loop systems. Production of the ground water reduces the pore pressure. Most of the open-loop facilities address this problem with reinjection of the working fluid into the reservoir; however, this solution can induce significant seismic events. For instance, induced earthquakes in an open-loop geothermal plant in Basel, Switzerland, led to suspension of the whole project (Giardini, 2009).

Focus of the present study is on enhancing heat extraction from a closed-loop geothermal wellbore via thermal conductive fractures. A thermoporoelastic finite element model is developed to study the geomechanical behavior of the proposed system as well as heat production. Thermoporoelasticity enables us to couple temperature, pore pressure, and displacement changes in the reservoir especially close to the wellbore. To solve the governing partial differential equations, Finite Element Method (FEM) is used to solve the governing equations.

In classic closed-loop systems, heat transfer is mainly limited to the area close to the wellbore. However, mere conduction cannot withdraw enough energy from the geothermal reservoir to keep the heat production economically feasible. To address this deficiency, somehow the formation-wellbore contact area as well as the conductivity of the area around the wellbore should be increased. To improve the conductivity in the vicinity of the wellbore and to minimize the heat loss, high conductivity cements can be used (Xu and Chung, 2000; Dahi Taleghani, 2013). Hydraulic fracturing of geothermal wells can improve the formation-wellbore contact area and may increase the rate of heat extraction. Figure 4.2 depicts a horizontal wellbore connected to a double-wing vertical fracture. The induced fracture is filled by the proppants with significantly larger thermal conductivity than the thermal conductivity of the rock matrix. The conductive fracture acts as a thermal conduit to transfer the heat from the reservoir into the wellbore.

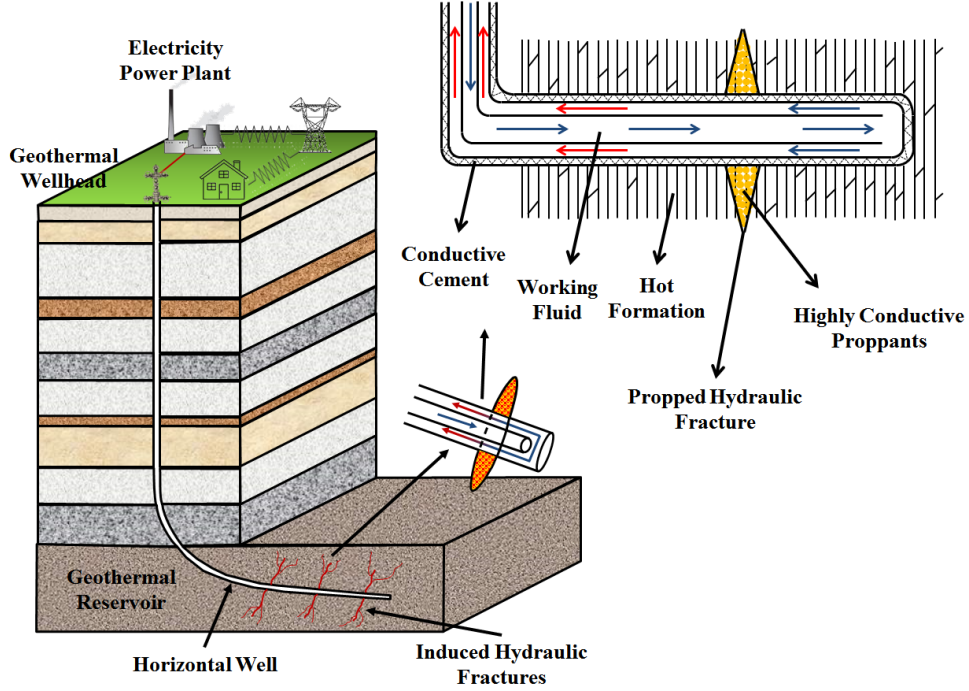


Figure 4.2: Schematic of closed loop geothermal system with fractured wellbore. Hydraulic fractures are filled with the high thermal-conductive proppants to improve the heat withdrawal efficiency from the reservoir.

In conventional hydraulic fracturing treatments, fractures facilitate the fluid flow into the wellbore; therefore, proppant crushing is a serious issue. However in the proposed configuration, induced fractures are designed to enhance the heat flow into the wellbore. Proppant with high thermal conductivity should be used in this technique. Proppants crushing cannot be considered as an issue anymore in the proposed configuration. Proppant crushing happens if the reservoir in-situ stress exceeds the strength of the proppants. Crushing of proppants may significantly improve the thermal conductivity of the fracture. The objective of this study is to show how thermally conductive fractures may enhance the heat extraction from the low-enthalpy reservoirs utilizing closed-loop system.

### 4.3 Governing Equations

Fluid flow, heat conduction and convection as well as rock deformation are interacting phenomena involved in the functioning of the proposed geothermal system. The governing

equation of the thermo-hydro-mechanical problem can be obtained from the balance principles. The displacement, pore pressure, and temperature are usually the primary solution field stored at the nodal points. If the whole set of governing equations are solved simultaneously, then the solver is called monolithic. The monolithic solver is particularly important for strongly coupled problems.

Porous media is void solid frame saturated with the geofluids. Interactions between the solid grains, geofluids, and external forces dictate the relationship between fluid flow, heat transfer, and mechanical behavior of the porous media. To analyze the behavior of such a system, a multidisciplinary approach is required to couple the solid deformation with the change in the pore pressure and the medium temperature. Change in the volume of rock matrix comes from the rock expansion/contraction, induced by the temperature rise/drop as well as fluid injection/production. The induced deformation, caused by the rock contraction/expansion, may affect the reservoir storage capacity and its permeability.

In the literature, there are several analytical solutions to study the coupling of heat transfer and fluid flow in deformable porous media (McTigue, 1986; Kodashima and Kurashige, 1996; Bai and Abousleiman, 1997; Belotserkovets and Prevost, 2011). However, these analytical solutions are derived for simple geometries with limited initial and boundary conditions, and neglecting different terms in the governing equations. In contrast, numerical method is more powerful and flexible to accurately approximate the solutions of realistic engineering problems. For instance, McTigue (1986) decoupled the energy equation from the momentum and mass balance equations. Kodashima and Kurashige (1996) did not consider the effect of the thermo-poro-mechanical response on the displacement fields. Bai and Abousleiman (1997) solved a thermo-poroelasticity problem for a one-dimensional geometry by dismissing convection in their solution.

Any disturbance in the formation temperature or pore pressure can initiate deformation. The deformation of a one-dimensional porous skeleton under loading was originally introduced by the Terzaghi (1925). He studied the behaviors of fully saturated soils under a



constant loading and considered the role of grains deformation. However, Biot (1941) established the theory of three-dimensional consolidation, for incompressible fluids, based on the initial work of Terzaghi (1925). Biot's formulation was developed by Rice and Cleary (1976) for compressible fluids. McTigue (1986) evolved the previous works by adding the term of non-isothermal conduction to the governing equations.

In the following sections, the general forms of constitutive laws, momentum balance, mass balance, and energy balance equations for a single-phase fluid in a deformable porous medium are developed. The weak form of governing equations, assembly of global matrices and solution procedure are provided in Appendix A. The thermoporoelastic equations assume isotropic solid matrix, small deformations, and instantaneous thermal equilibrium between the solid grains and fluid particles. Instantaneous thermal equilibrium between the solid grains and fluid particles means an equal temperature between the solid and fluid phases.

#### 4.3.1 Momentum Balance

Considering Newton's second law of motion, an increase in the linear momentum of a mass volume should be equal to the external force acting on the material. The momentum balance in the absence of inertial forces for a saturated porous media can be written as shown in Equation (4.1). The superscripts “*s*” and “*f*” refer to the solid phase and fluid phase.

$$\nabla^T \sigma + \rho g = 0 \tag{4.1}$$

$$\rho = (1 - \phi)\rho_s + \phi\rho_f$$

where

$$\nabla^T \sigma = \begin{bmatrix} \frac{\partial}{\partial x} & 0 & 0 & \frac{\partial}{\partial y} & 0 & \frac{\partial}{\partial z} \\ 0 & \frac{\partial}{\partial x} & 0 & \frac{\partial}{\partial y} & \frac{\partial}{\partial z} & 0 \\ 0 & 0 & \frac{\partial}{\partial x} & 0 & \frac{\partial}{\partial y} & \frac{\partial}{\partial z} \end{bmatrix} \tag{4.2}$$

Recalling from poroelasticity theory, the total stress in a porous medium is a linear function of the effective stress, pore pressure, and Biot's constant. Biot's constant is equal to the ratio of the volume change in the fluid phase filling the pores to the change in the volume of the solid matrix. The compressive forces are assumed to have negative sign in this study. The relationship between displacement, pore pressure and reservoir temperature is described by the mass and energy balance equations driven in the next following sections.

$$\begin{aligned}\sigma &= \sigma'' + \alpha m P_f \\ m &= \begin{bmatrix} 1 & 1 & 1 & 0 & 0 & 0 \end{bmatrix}\end{aligned}\tag{4.3}$$

#### 4.3.2 Mass Balance

By assuming Darcy's law, the mass balance equation for a saturated porous medium in the absence of chemical reactions can be considered as follows

$$\left(\frac{\alpha - \phi}{K_s} + \frac{\phi}{K_f}\right)\frac{\partial P_f}{\partial t} + \alpha m^T L \frac{\partial u}{\partial t} - \beta_{sf} \frac{\partial T}{\partial t} + \nabla^T \left[ \frac{k}{\mu_f} (-\nabla P_f + \rho_f g) \right] = 0\tag{4.4}$$

$$\beta_{sf} = (\alpha - \phi)\beta_s + \phi\beta_f\tag{4.5}$$

where  $\beta$  is the thermal expansion coefficient.  $K$ ,  $u$ ,  $k$ , and  $\mu_f$  are the bulk modulus, solid displacement, permeability, and fluid viscosity, respectively. The first coefficient in the mass balance equation which describes the specific storage of the porous medium at a constant strain is a function of solid and fluid compressibilities.

#### 4.3.3 Energy Balance

To satisfy the first law of thermodynamics in a porous medium, the enthalpy equation might be written like Equation (4.10), resulting in the merger of Equation (4.6) with the fluid-phase

energy balance equation of (4.7). In this equation, it is assumed that the conduction in the solid- and the fluid-phase act simultaneously which means temperature of the solid- and the fluid-phase are equal to each other. The effects of the viscous dissipation and radioactivity are neglected in the energy equation and it is assumed that Darcy's law defines the fluid flow in the formation. In the energy equation, the first term accounts for the heat accumulation. However, second term represents the convective heat transfer and the last one describes conduction. In this study, it is assumed that the formation rock is fully saturated with water. Equations (4.8) and (4.9) show the functionality of water density and viscosity with its temperature.

$$\text{Solid} - \text{phase} : (1 - \phi)(\rho C_p)_s \frac{\partial T_s}{\partial t} - (1 - \phi) \nabla^T (\chi_s \nabla T) = 0 \quad (4.6)$$

$$\begin{aligned} \text{Fluid} - \text{phase} : & \phi(\rho C_p)_f \frac{\partial T_f}{\partial t} - \phi \nabla^T (\chi_f \nabla T) + \\ & \left[ \rho_f C_{pf} \frac{k}{\mu_f} (-\nabla P_f + \rho_f g) \right] \cdot \nabla T = 0 \end{aligned} \quad (4.7)$$

$$\rho_w = \frac{999.8}{1 + 0.000088T_w} \quad (4.8)$$

$$\mu_w = 2.41318 \times 10^{-5} \times 10^{\frac{247.8}{T_w + 134.15}} \quad (4.9)$$

Assuming that  $T_f = T_s = T$

$$\begin{aligned} \text{Porous} - \text{phase} : (\rho C_p)_{eff} \frac{\partial T_s}{\partial t} + [\rho_f C_{pf} \frac{k}{\mu_f} (-\nabla P_f + \rho_f g)] \cdot \nabla T \\ - \nabla^T (\chi_{eff} \nabla T) = 0 \end{aligned} \quad (4.10)$$

where

$$(\rho C_p)_{eff} = (\alpha - \phi) \rho_s C_{ps} + \phi \rho_f C_{pf} \quad (4.11)$$

$$\chi_{eff} = (\alpha - \phi) \chi_s + \phi \chi_f \quad (4.12)$$

The heat capacity of porous medium is shown in Equation (4.11), using the heat capacities of rock matrix and fluid phase in conjunction with rock porosity. Effective thermal conductivity, shown by  $\chi_{eff}$ , determines the average thermal conductivity of the porous medium using the porosity and the thermal conductivities of both fluid and solid phases. In this study, the momentum balance and mass balance are fully coupled, while thermal transport may affect the solid deformation and pore-fluid diffusion but not vice versa.

#### 4.3.4 Elastic Constitutive Law

We assumed that the rock shows elastic behavior; however, the proposed coupled model can be extended to nonlinear or plastic behavior depending on the rock properties. Considering the large magnitude of the in-situ stresses, it is essential to consider in-situ stress conditions as the initial stress state in order to obtain more accurate analysis.

The constitutive law for the isotropic elastic behavior is written as Equation (4.13) where  $\varepsilon$ ,  $u$ , and  $D$  are strain, displacement, and the elasticity matrix, respectively.  $\varepsilon$  is the total

strain and  $\varepsilon^{Thermal}$  is the thermal strain. However,  $\varepsilon_0$  represents any initial or residual strains. To reduce the computational costs, this problem is modeled for the two-dimensional plane-strain geometry.

$$\sigma'' = D(\varepsilon - \varepsilon_0 - \varepsilon^{Thermal}) \quad (4.13)$$

$$\varepsilon^{Thermal} = m\left(\frac{\beta_s}{3}\right)T \quad (4.14)$$

A finite element solution based on the above governing equations is developed in MATLAB 2012. The Newton-Raphson method is applied to linearize the resultant non-linear equations in conjunction with the finite difference discretization for the time domain.

#### 4.3.5 Seismic Assessment

To estimate the seismic magnitude of the proposed technique in this study, the Kanamori and Brodsky (2004) formula is used to measure the seismic moment. They relate the seismic moment,  $M_0$  to fault size,  $A$  and its average slippage:

$$M_0 = GAd \quad (4.15)$$

where  $G$  is the shear modulus of the rock. The calculated seismic moment can then be used to estimate the moment magnitude of the induced seismic event represented by  $M$  (Kanamori and Anderson, 1975).

$$M = \frac{\log_{10} M_0}{1.5} - 6.1 \quad (4.16)$$

#### 4.4 Verification

To examine the accuracy of the developed multiphysics finite element code, the results of a few benchmark problems in literature are compared with the computational results obtained from the simulator developed for this research. These verifications evaluate the reliability of our numerical results. The analytical solution for these benchmark problems are given in Appendix B.

The first benchmark is the Mandel’s two-dimensional consolidation problem. In this problem, a porous medium is under a uniform vertical loading from top and bottom as shown in Figure 4.3. Fluid can freely drain from the lateral boundaries while the other two boundaries are impermeable. Analytical solution at the early times of production shows an unexpected jump in the pore pressure at the center of the compressed sample. This phenomenon in the soil mechanics literature is known as the Mandel’s effect which can be observed in core samples collected from the subsurface (Wang, 2000). Table 4.3 illustrates a list of required parameters to solve Mandel’s problem. Figure 4.3 presents the agreement of pore pressure distributions calculated by analytical and numerical methods.

Table 4.3: List of required parameters to solve the Mandel’s problem

Parameter	Value	Unit
Young’s modulus	14.4	GPa
Poisson’s ratio	0.1	
Biot’s coefficient	1	
Rock density	2000	Kg.m <sup>-3</sup>
Fluid density	1000	Kg.m <sup>-3</sup>
Porosity	0.2	
Permeability	$2 \times 10^{-13}$	m <sup>2</sup>
Fluid bulk modulus	2200	GPa
Rock bulk modulus	8	GPa
Dynamic viscosity	0.2	Pa.s
Load	4	MPa
Length	10	m
Height	20	m

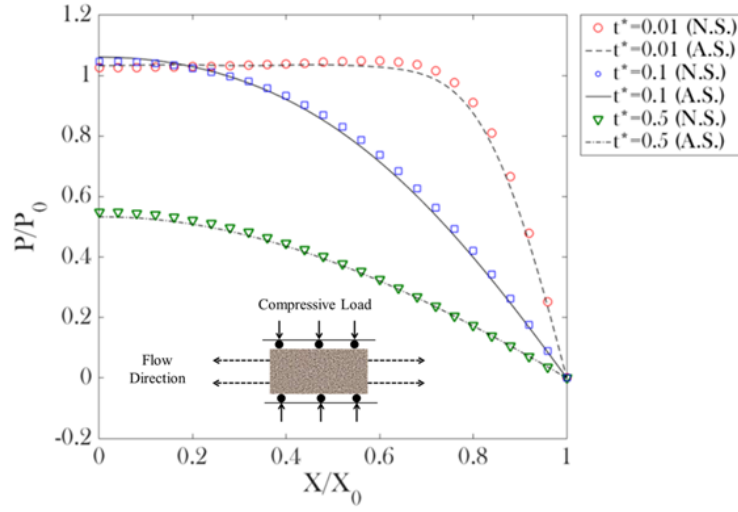


Figure 4.3: Verification of numerical solution with the Mandel's analytical solution. Fluid can be extracted from the sides while top and bottom boundaries are impermeable.

As the first benchmark validates the accuracy of the numerical simulator under an external loading, the second problem considers the fluid flow as a favorable boundary condition. In the Cooper-Jacob's two-dimensional problem shown in Figure 4.4, a transient flow of fluid is produced from a vertical wellbore located at the middle of an aquifer with finite boundaries. This was the hydrologist who developed a mathematical model for the indicated problem, using the analogy between the heat conduction and fluid flow (Theis, 1935). Table 4.4 lists the values of the parameters required to solve this problem. Figure 4.4 shows resemblance of the analytical and numerical solutions.

The last verification problem is the Elder's convection example. Elder (1967) through a laboratory experiment developed a time-dependent benchmark for density-driven flow in a porous medium. Temperature variations may initiate a density-driven flow. This problem is a well-known benchmark in the heat transfer literature that displays the effect of buoyancy forces. To accurately model this system, the computational software should have the flexibility to correct the fluid density and viscosity with changes in fluid temperature. Table 4.5 represents a list of the required parameters to solve the Elder's benchmark.

Table 4.4: List of required parameters to solve the Theis-Jacob's problem

Parameter	Value	Unit
Young's modulus	14.4	GPa
Poisson's ratio	0.2	
Biot's coefficient	1	
Rock density	2000	Kg.m <sup>-3</sup>
Fluid density	1000	Kg.m <sup>-3</sup>
Porosity	0.2	
Permeability	$2 \times 10^{-13}$	m <sup>2</sup>
Fluid bulk modulus	2200	GPa
Rock bulk modulus	8	GPa
Dynamic viscosity	0.001	Pa.s
Fluid rate	$10^{-3}$	Kg.m <sup>-2</sup> .s <sup>-1</sup>

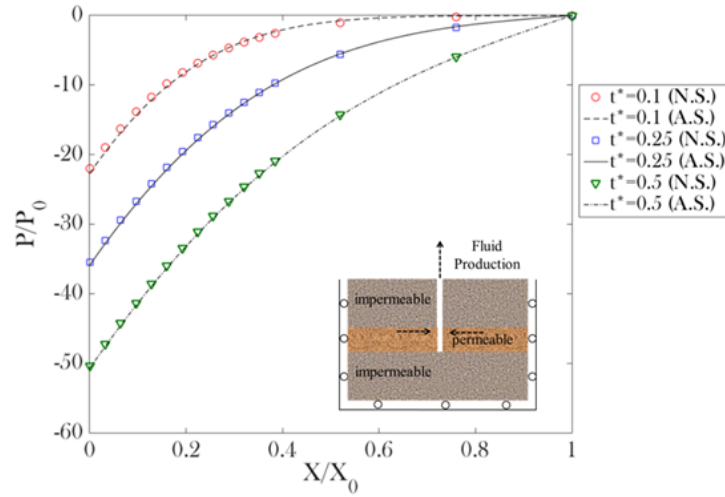


Figure 4.4: Verification of numerical solution with the Theis-Jacob's analytical solution. The middle layer is permeable while the top and bottom layer are impermeable. Fluid trapped in the permeable layer can flow into the well.

Figure 4.5 compares the temperature distribution at dimensionless time of 0.1 between the Elder's laboratory experiment and our numerical result. The density gradient due to temperature anomalies between the bottom edge and the top boundaries acts as a driving force to form eddies in the model. The growing eddies at the two sides of the heat source cannot penetrate through the impermeable boundaries. The impermeable boundaries cause reverse circulation and development of another finger at the middle of the bottom boundary.



Upon validation of the numerical software, we can move forward to model a closed-loop geothermal system to investigate its thermo-geomechanical behavior during its operation.

Table 4.5: List of parameters used to solve the Elder's problem

Parameter	Value	Unit
Young's modulus	14.4	GPa
Poisson's ratio	0.2	
Biot's coefficient	1	
Rock density	2000	$\text{Kg.m}^{-3}$
Fluid density	1000	$\text{Kg.m}^{-3}$
Porosity	0.1	
Permeability	$9.084 \times 10^{-9}$	$\text{m}^2$
Fluid bulk modulus	2200	GPa
Rock bulk modulus	8	GPa
Dynamic viscosity	0.001	Pa.s
Initial medium temperature	10	$^{\circ}\text{C}$
Heat source temperature	20	$^{\circ}\text{C}$
Ratio of length to height	4	
Solid thermal conductivity	2	$\text{W.m}^{-1} \text{ } ^{\circ}\text{C}^{-1}$
Solid heat capacity	$2 \times 10^3$	$\text{Kj.m}^{-3} \text{ } ^{\circ}\text{C}^{-1}$
Fluid thermal conductivity	0.6	$\text{W.m}^{-1} \text{ } ^{\circ}\text{C}^{-1}$
Fluid heat capacity	4182	$\text{Kj.m}^{-3} \text{ } ^{\circ}\text{C}^{-1}$
Fluid thermal expansion coefficient	$1.5 \times 10^{-4}$	$^{\circ}\text{C}^{-1}$

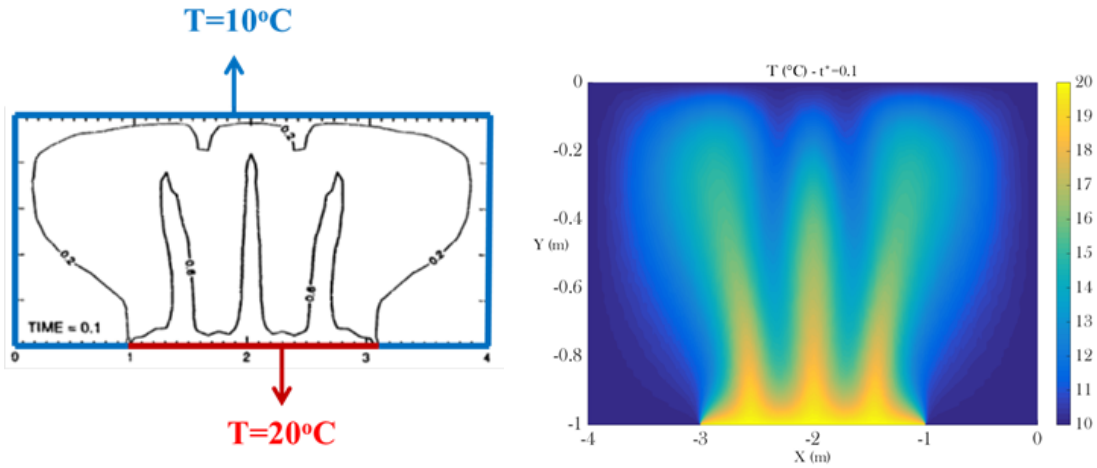


Figure 4.5: Verification of numerical temperature with the Elder's experimental benchmark at the dimensionless time of 0.1. The initial temperature of the medium is  $10^{\circ}\text{C}$ . Half of the bottom boundary is exposed to a heat source, keeping its temperature at a constant value of  $20^{\circ}\text{C}$ . Elder's benchmark is famous for illustrating the effect of buoyancy and convection.

## 4.5 Results and Discussion

Drastic climate changes during the last century caused by the emission of greenhouse gases from the burning fossil fuels has encouraged countries to expand the application of clean and sustainable energy resources. Geothermal energy is one of these sustainable resources and the general interest in the production of electricity from the geothermal power plants has immensely risen in recent years. The aim of the present study is to illustrate how induced hydraulic fractures filled with the highly thermal-conductive proppants may enhance the efficiency of heat withdrawal in the closed-loop systems as a new technique. The surface subsidence and seismic hazards involved in the heat production from the geothermal systems are studied through executing a coupled finite element simulation.

Drilling a well has a significant share in the overall costs of a geothermal project. To reduce the project costs, existing abandoned wells in the areas with sufficient temperature gradient can be converted into the geothermal wells. A candidate reservoir in the United States with several abandoned oil and gas wells can be found in *Camerina A* formation. Camerina A is a geopressed formation located in South Louisiana, at the border of Vermillion and Acadia Parishes. Camerina A formation located at the depth of 4000 meters below the ground surface has a thickness of 200 to 400 meters at different locations. Kehle (1973) estimated a temperature gradient of 28 to 30°C per kilometer along the sand layer of this formation. Recalling the Nicholson's definition from Table 4.1, this formation can be categorized as a low-enthalpy geothermal reservoir. Numerical simulations in this study are executed for a reservoir with the similar rock-fluid-physical properties as Camerina A formation. Table 4.6 summarizes all of the properties required to model heat withdrawal from the proposed geothermal system described in Figure 4.2 (Gray, 2010).

To model the heat transfer and fluid flow along with the mechanical behavior of the rock matrix, a fully coupled two-dimensional finite element model is developed to represent the heat withdrawal from a horizontal wellbore connected to a vertical induced fracture.

Table 4.6: List of parameters used to solve the Elder's problem

Parameter	Value	Unit
Young's modulus	13.8	GPa
Poisson's ratio	0.3	
Biot's coefficient	1	
Rock density	2700	Kg.m <sup>-3</sup>
Fluid density	1000	Kg.m <sup>-3</sup>
Porosity	0.2	
Permeability	$2 \times 10^{-13}$	m <sup>2</sup>
Fluid bulk modulus	2.15	GPa
Rock bulk modulus	11.1	GPa
Dynamic viscosity	$3 \times 10^{-4}$	Pa.s
Wellbore temperature	40	°C
Solid thermal conductivity	1.9	W.m <sup>-1</sup> °C <sup>-1</sup>
Solid heat capacity	1000	Kj.m <sup>-3</sup> °C <sup>-1</sup>
Fluid thermal conductivity	0.649	W.m <sup>-1</sup> °C <sup>-1</sup>
Fluid heat capacity	3726	Kj.m <sup>-3</sup> °C <sup>-1</sup>
Fluid thermal expansion coefficient	$4.5 \times 10^{-4}$	°C <sup>-1</sup>
Rock thermal expansion coefficient	$1 \times 10^{-6}$	°C <sup>-1</sup>
Fracture height	80	m
Fracture width	4	cm
Wellbore half-length	50	m
Fracture diameter	22	cm

Formation rock displacements are modeled by quadratic triangular elements with the mesh shown in Figure 4.6. Temperature and pore pressure are represented by linear shape functions for the three nodes on each corner.

The geothermal reservoir in our model has a thickness of 200 meter and a permeability of  $2 \times 10^{-13} \text{ m}^2$  while the permeability of the upper and lower geological layers (shales) is  $10^{-4}$  times smaller than the reservoir permeability. The indicated model includes a horizontal well with a length of 100 meters located at the depth of 4100 meters below the ground surface. The wellbore has a diameter of 22 centimeters. A vertical fracture with a width of 4 centimeters and a half-length of 40 meters intersects the middle of the horizontal wellbore. Size of the domain is  $5000 \times 5000$  square-meter which is larger than the volume affected by the heat transfer between the wellbore and formation. Due to the symmetry with respect to the well axis and to reduce the computational costs, the numerical simulation is executed

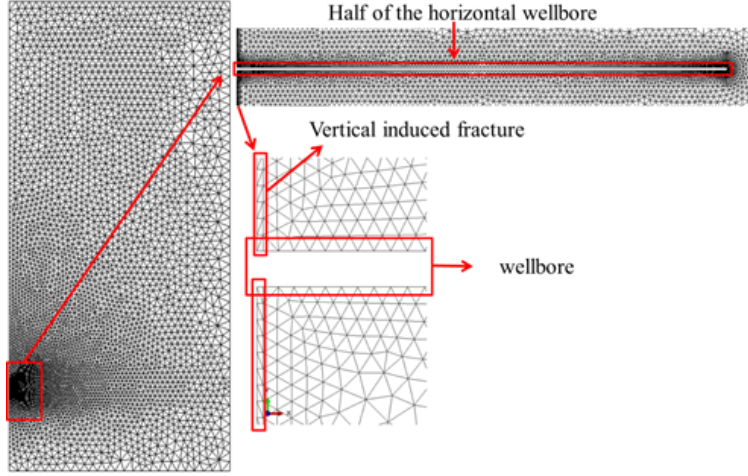


Figure 4.6: The picture represents the mesh distribution across the considered domain, around the wellbore and two wings of the fracture. Displacement quadratic triangular elements, with six nodes on each element, in conjunction with linear triangular element for temperature and pore pressure cover the domain of finite element model.

for only half of the problem. The symmetry imposes zero horizontal displacements at the left boundary. Displacements in the normal directions are restricted at the bottom and right boundary. To measure the surface subsidence, no constraint is applied on the top boundary. Zero fluid-flux is considered at the far-field boundaries. To characterize the fluid flow in the fracture-matrix, a dual-porosity/dual-permeability model is formulated. The temperature gradient of  $28^{\circ}\text{C}$  per kilometer is assumed for the model with the surface temperature of  $20^{\circ}\text{C}$ . Temperature at the far-field boundaries is kept constant and equal to the initial temperature. The wellbore temperature which is lower than the medium temperature is defined separately for each numerical experiment. The significant temperature gradient at the wellbore and close to the fracture imposes a refined mesh distribution at those areas in order to reduce the numerical instabilities of the solution.

Figures 4.7 and 4.8 illustrate the extracted thermal power from a horizontal well in a closed-loop system. In these figures, the captions of “NF”, “F”, “KP”, and “ $\Delta T$ ” stand for unfractured well, fractured well, proppants thermal conductivity, and the initial temperature gradient between the wellbore and reservoir, respectively.

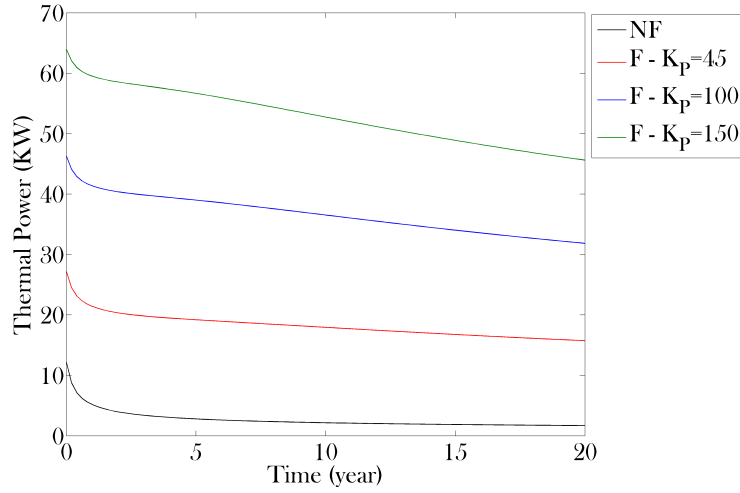


Figure 4.7: Comparing thermal power into a horizontal well in a closed-loop geothermal system. The “NF”, “F”, and “KP” stand for unfractured well, fractured well, and thermal conductivity of the proppants, respectively. In the fractured wellbore, the artificial fracture is filled within three different types of proppants with thermal conductivities of 45, 100 and 150 W/m/°C. The larger is the thermal conductivity of the proppants, the more is the produced thermal power.

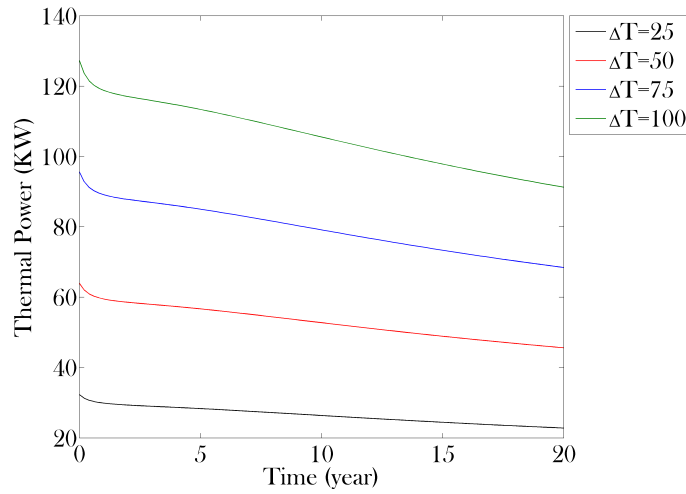


Figure 4.8: Comparing thermal power into a fractured horizontal well in a closed-loop geothermal system. The “ $\Delta T$ ” stands for the initial temperature difference between the wellbore and reservoir. The temperature difference is the main driving force for the heat transfer between the wellbore and the reservoir. The larger is the temperature difference, the more is the produced thermal power.

Figure 4.7 compares the heat flow of an unfractured wellbore and the fractured wellbore with different thermal conductivities of proppants filling the fracture. In Figure 4.7, the

initial temperature difference between the wellbore and reservoir is  $50^{\circ}\text{C}$  and the unit of thermal conductivity is  $\text{W/m/}^{\circ}\text{C}$ . The remaining properties are the same as listed in the Table 4.6. As it is shown in Figure 4.7, the lowest thermal power and consequently total produced heat belong to the unfractured wellbore in the closed-loop configuration. The magnitude of extracted heat from the unfractured wellbore in the closed-system is significantly lower than the magnitude in the fractured wellbore. In other words, unfractured closed-loop wellbore cannot withdraw enough heat from the geothermal reservoir in this pure conduction case to keep a geothermal project feasible. To keep the closed-loop competitive, the wellbore-formation contact area in the closed-loop should be increased. This can happen by fracturing the reservoir and then the induced fractures should be filled with the highly conductive proppants. This figure suggests that the extracted thermal power of the fractured wellbore is larger than the unfractured wellbore; however, the magnitude of increase in the thermal power is substantially a function of the thermal conductivity of the proppants filling the fracture. The larger is the proppant conductivity, the more is the heat flow into the wellbore. To improve the thermal conductivity of the common proppants, they can be coated with a layer of highly conductive metals or any other conductive material. Carbon-steel, cast-iron, aluminum, and copper with thermal conductivities of 53, 80, 214, and  $380 \text{ W/m/}^{\circ}\text{C}$ , respectively, are some of the metal coatings which can be considered to improve the proppants conductivities. Figure 4.8 highlights the role of the initial temperature difference on the extracted thermal power. In this figure, the wellbore is fractured and the fracture is filled by proppants with the thermal conductivity of  $150 \text{ W/m/}^{\circ}\text{C}$ . The rest of the parameters are the same as listed in the Table 4.6. The temperature gradient is the main driving force for the heat flow into the wellbore. The initial temperature of the reservoir is assumed to be uniform. However, we can control the wellbore temperature through adjusting the temperature of circulating working fluid and circulation rate. Figure 4.8 suggests that injecting a working fluid with lower temperature can result in the larger temperature difference and consequently more heat flow into the well. Figures 4.9 and 4.10

compare the magnitude of cumulative extracted heat during a time span of 20 years for the Figures 4.7 and 4.8, respectively. Figures 4.9 and 4.10 emphasize that connecting a wellbore to highly conductive fractures as well as enforcing a considerable temperature gradient can improve the extracted heat in the closed-loop geothermal systems.

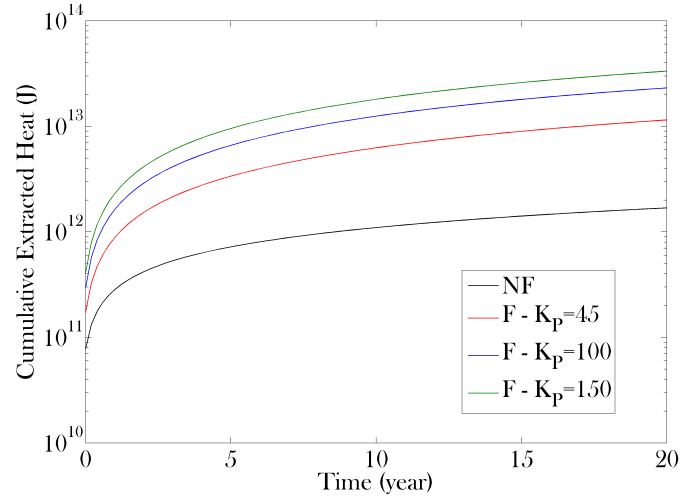


Figure 4.9: Comparing cumulative extracted heat from a horizontal well in a closed-loop geothermal system. The cumulative collected heat for the wellbore with the fracture filled within the high thermal conductive proppants is one order of magnitude larger than the unfractured wellbore.

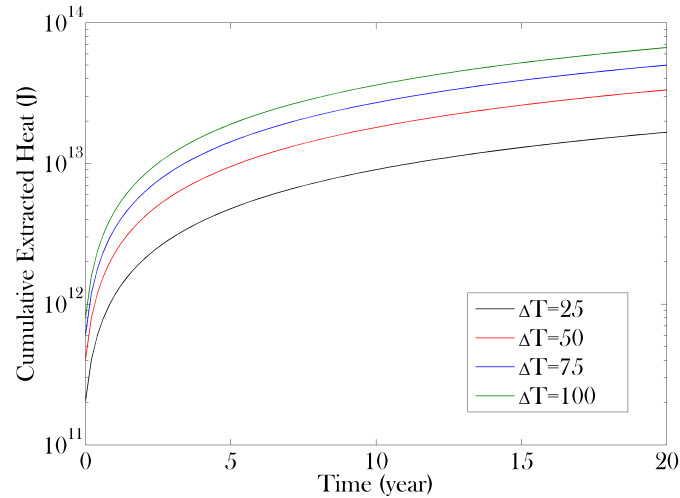


Figure 4.10: Comparing cumulative extracted heat from a horizontal well in a closed-loop geothermal system. This Figure suggest that the increase in the temperature difference can significantly improve the extracted heat.

To compare the heat withdrawals from the fractured wellbore in the closed-loop system with the unfractured wellbore in the open-loop configuration, assume a geofluid with a rate of  $5 \text{ Kg}/\text{m}^2/\text{s}$  flows into the unfractured wellbore in the open-loop configuration. The reservoir properties are the same as listed in the Table 4.6 and the length of the well is 100 meters. The results of our simulation suggest a thermal power of 923 KW for the open-loop system with the indicated flow rate. This thermal power is significantly larger than the thermal power of the fractured well in our closed-loop configuration shown in Figures 4.7 and 4.8. However, the calculated thermal powers in these figures are only for a single fracture during one stage of hydraulic fracturing treatments. The common length of a horizontal well in a shale or sandstone reservoirs is in the range of 3000 ft, roughly a kilometer, with 20 to 25 fracturing stages. Considering 20 to 25 fracturing stages which are common in horizontal wells of this length, 3000 ft, and multiply them with the thermal powers in Figures 4.7 and 4.8, one can conclude that the proposed closed-loop configuration might be compatible with the open-loop configurations. The efficiency factor of 0.25 to 0.3 is considered to be reasonable in the open-loop enhanced geothermal reservoirs, including the required energy to run the pumping facilities and it accounts for all of the heat losses in the cement, casing, and turbine.

All of the figures for the rest of the paper are illustrated for the fractured well with temperature gradient of  $100^\circ\text{C}$  and proppant conductivity of  $150 \text{ W}/\text{m}/^\circ\text{C}$  as this scenario has the largest rate of heat extraction. Figure 4.11 describes the temperature drop in the closed-loop configuration after 20 years of heat production. The temperature drop is calculated by subtraction of the current temperature from the initial temperature. Effect of fracture on heat production, shown in Figure 4.7, is more tangible when the fracture is filled with the highly conductive proppants. In this case, the temperature front stretches along the fracture height, sweeping larger area of the formation, shown in Figure 4.12. Figure 4.12 illustrates propagation of the temperature front across the fracture. The maximum temper-



ature drop happens at the intersection of the wellbore and the fracture. The magnitude of the temperature drop reduces from the intersection towards the fracture tip.

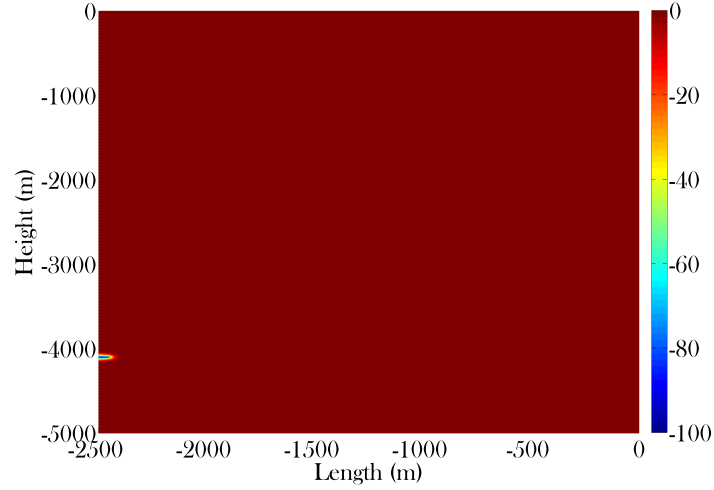


Figure 4.11: Temperature drop, in centigrade, across the geothermal model after 20 years of heat withdrawal. Temperature drop is calculated by subtraction of the current temperature from the initial temperature.

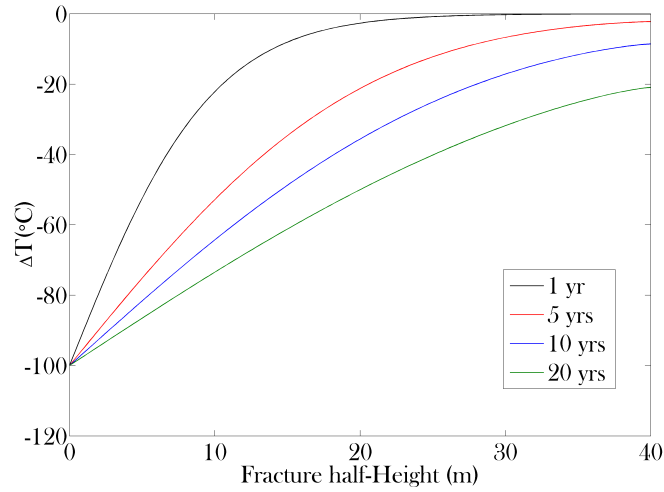


Figure 4.12: Temperature drop changes versus time, measured along one of the fracture wings. Fracture is filled by the proppants with thermal conductivity of 150 W/m/°C. The initial temperature gradient at the wellbore is 100°C.

Figure 4.13 compares the pressure drop in the reservoir after 20 years of heat production. The magnitude of pressure drop is not significant since there is no reservoir fluid production in

the closed-loop system. Most of the open-loop systems have to deal with the risks of induced seismicity due to the change of pore pressure in the reservoir. For instance, the Basel geothermal power plant in Switzerland was suspended by the government after receiving complaints from the local residents regarding the induced earthquakes. The magnitude of induced earthquakes in this power plant, caused by the significant manipulation in the reservoir pressure, was large enough to persuade the officials to suspend the whole project. This example describes how the change in the pore pressure can leave the whole project in danger. Since change in pore pressure in the proposed configuration in this study is negligible, there is no fear about the induced seismicity issues.

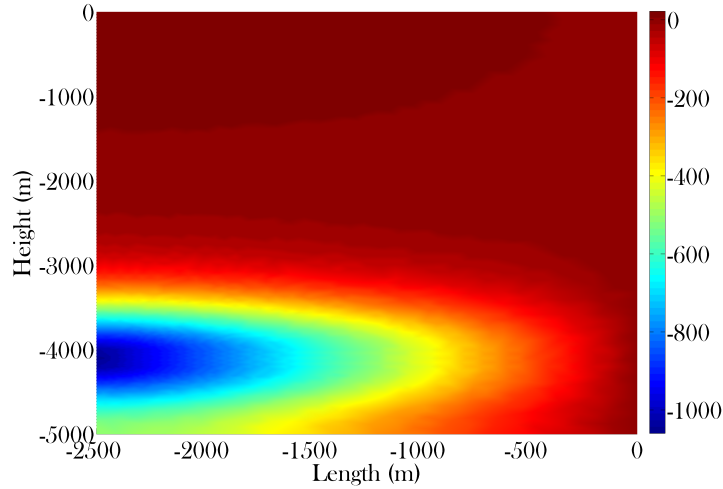


Figure 4.13: Pressure drop, in Pa, across the geothermal model after 20 years of heat withdrawal. Pressure drop is calculated by subtraction of the current temperature from the initial temperature.

Horizontal and vertical displacements across a reservoir are induced by either change in pore pressure or the change in reservoir temperature. As shown in the Figure 4.13, change in pore pressure in our configuration is negligible. However, the significant temperature drop along the wellbore induces displacement through shrinkage in the rock volume. Figures 4.14 and 4.15 present the distribution of horizontal and vertical displacement component across the geothermal model, respectively. The negative sign of horizontal displacement in Figure 4.14 accounts for the rock shrinkage due to the temperature drop along the wellbore.

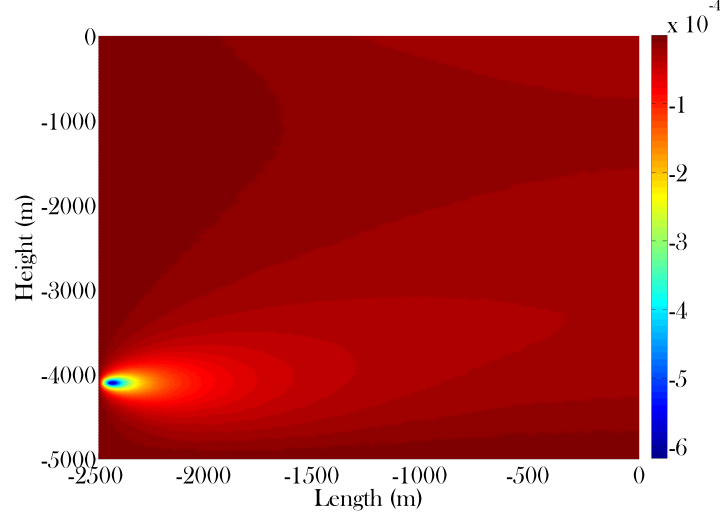


Figure 4.14: Horizontal displacement, in meter, across the geothermal model after 20 years of heat withdrawal. The maximum horizontal displacement happens around the wellbore.

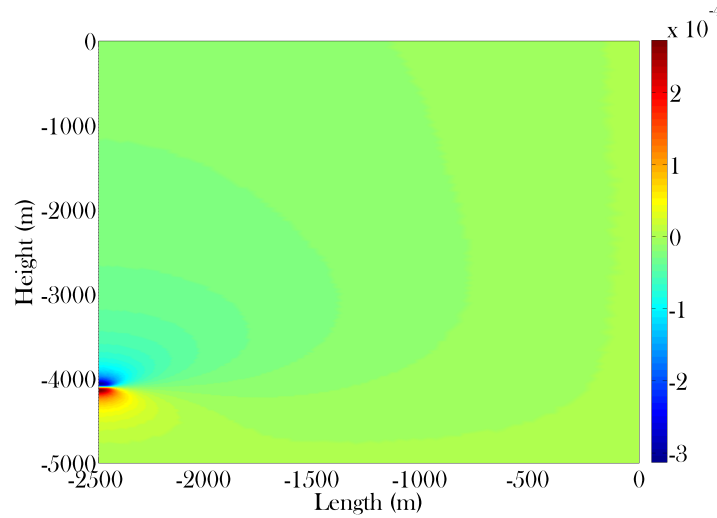


Figure 4.15: Vertical displacement, in meter, across the geothermal model after 20 years of heat extraction. The maximum vertical displacement happens around the wellbore.

With expansion of temperature front in the reservoir, the magnitude of horizontal displacement as well as propagation of displacement front grows in the system. The negative sign of vertical displacement in the Figure 4.15 demonstrates that part of the reservoir in contact with the lower edge of the wellbore shrinks downward. However, the positive sign illustrates the upward motion in the area of formation-wellbore contact area. Figure 4.16 compares the magnitude of surface subsidence with time. Surface subsidence at the far-field boundary

is zero; however, the ground surface shifts downward as it gets closer to the areas above the wellbore. Surface subsidence is one of the main sources of public fears related to any underground operation. The level of surface subsidence in our proposed model is quite small which does not affect the feasibility of the project.

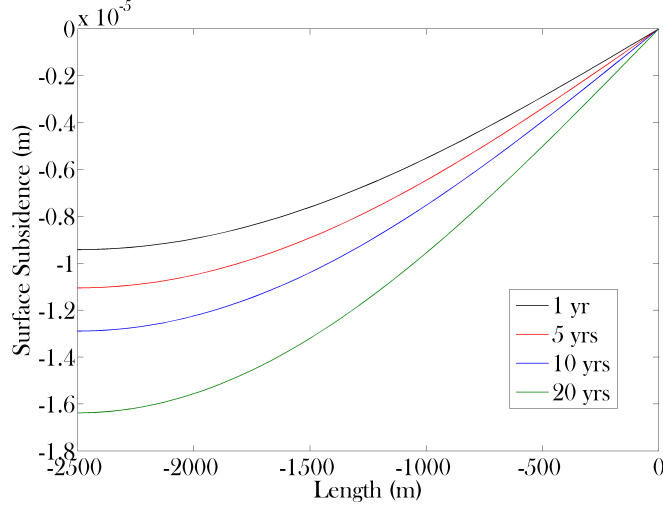


Figure 4.16: Surface subsidence versus time in a closed-loop fractured wellbore. The magnitude of surface subsidence increases with time. The largest subsidence happens at the middle of the model where the horizontal well is intersected with a vertical fracture.

To perform a seismic assessment for the proposed technique, we use the method described in the seismic assessment section. For the sake of simplicity, we assume that the mean slip in the Equation (4.15) is equal to the maximum induced displacement in our numerical model. The maximum displacements as shown in Figures 4.14 and 4.15 happen in the vicinity of the wellbore. To calculate the rupture area in the Equation (4.15), we assume that the rupture length in our 2D model is equal to the wellbore radius with a circular rupture patch. Using both the indicated equations, the moment magnitude of the seismic event in this study is equal to -2.71 which is an ignorable tremor with a small magnitude.

Figures 4.17 and 4.18 show the principal horizontal and vertical stress component; however, the shear component of stress field is represented in Figure 4.19. The illustrated stress distribution accounts for the mechanical stresses as well as the thermal stress. As it is shown in these examples, the maximum stress happens in the vicinity of the wellbore where there is

the maximum temperature drop in the system. The stress front develops in the system with the propagation of temperature-drop front since the change in the pore pressure is negligible.

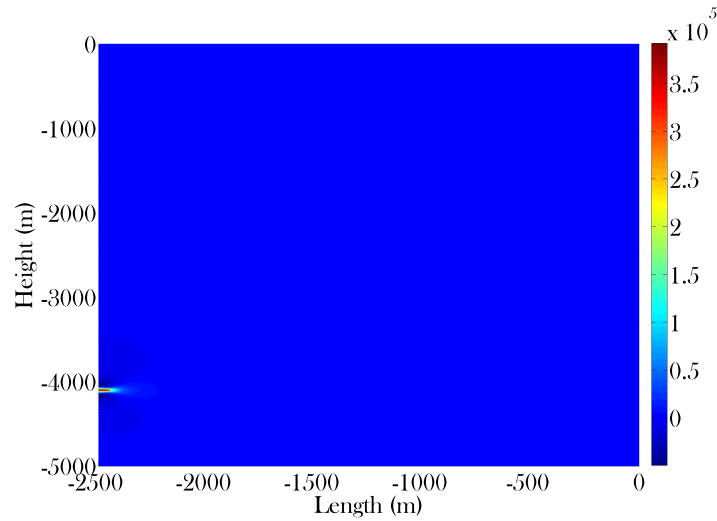


Figure 4.17: Principal horizontal stress across the geothermal model after 20 years of heat extraction. The stress unit is Pa.

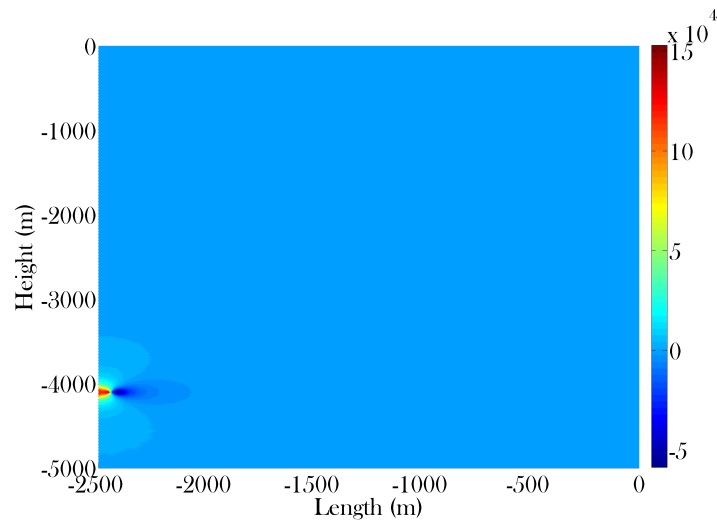


Figure 4.18: Principal vertical stress across the geothermal model after 20 years of heat extraction. The stress unit is Pa.

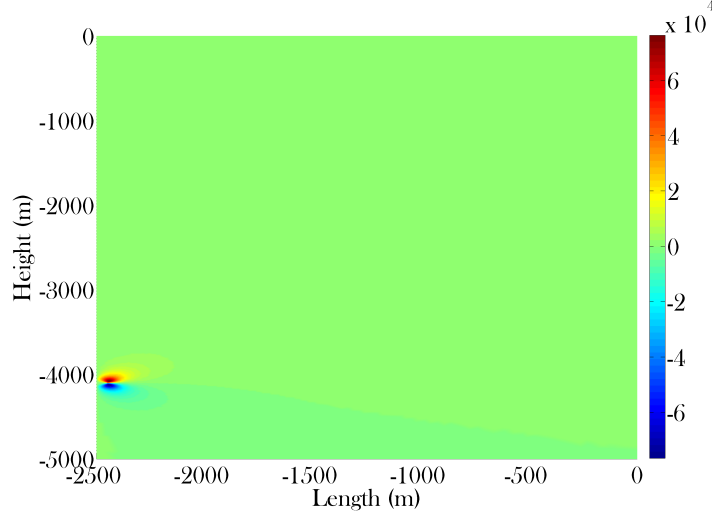


Figure 4.19: Shear stress across the geothermal model after 20 years of heat extraction. The stress unit is Pa.

#### 4.6 Conclusion

In this study, we provide a comprehensive analysis of a new method for heat extraction from the low-enthalpy geothermal reservoirs without mass withdrawal. The developed coupled numerical model in this study assesses the effectiveness of the proposed closed-loop configuration including the induced hydraulic fractures propped with highly thermal conductive materials to enhance heat production. The highly conductive proppants placed inside the fracture virtually increase the wellbore-formation contact area through absorbing the heat from a larger volume of the reservoir. In comparison with the conventional hydraulic fracturing treatments in the oil or gas industry, the proppants crushing in this technique has a positive impact, since the crushed proppants still can transfer the heat from the reservoir to the wellbore. As it is shown in the results and discussion section, the magnitude of surface subsidence and displacements across the formation is very small which significantly reduces the risk of induced seismicity compared to open-loop systems. The rate of heat flow into the wellbore in our technique strongly depends on the thermal conductivity of the proppants, the temperature gradient between the circulating working fluid and the reservoir, and the

magnitude of increase in the wellbore-formation contact area. The numerical simulations show promising economic value for the application of this technique to horizontal wellbores.

## 4.7 References

- Armstead, H. C. H. "Geothermal energy: Its past, present, and future contributions to the energy needs of man E. and FN Spon." London, UK (1983).
- Bai, M., and Y. Abousleiman. "Thermoporoelastic coupling with application to consolidation" *International Journal for Numerical and Analytical Methods in Geomechanics*: 21.2 (1997): 121-132.
- Belotserkovets, A., and J. H. Prevost. "Thermoporoelastic response of a fluid-saturated porous sphere: An analytical solution." *International Journal of Engineering Science*: 49.12 (2011): 1415-1423.
- Benderitter, Y., and G. Cormy. "Possible approach to geothermal research and relative costs" *Small geothermal resources: A guide to development and utilization*, UNITAR, New York (1990): 59-69.
- Biot, M. A. "General theory of threedimensional consolidation." *Journal of applied physics* 12.2 (1941): 155-164.
- Dahi Taleghani, A. "An Improved Closed-Loop Heat Extraction Method from Geothermal Resources" *Journal of Energy Resources Technology* 135.4 (2013): 042904.
- Diao, N., Q. Li, and Z. Fang. "Heat transfer in ground heat exchangers with groundwater advection." *International Journal of Thermal Sciences* 43.12 (2004): 1203-1211.
- Dickson, M. H., and M. Fanelli. "Geothermal energy: utilization and technology." Routledge, 2013.
- Duffield, W. A., and J. H. Sass. "Geothermal energy: Clean power from the earth's heat. Diane Publishing: Vol. 1249. (2003).
- Elder, J.W. "Transient convection in a porous medium. *Journal of Fluid Mechanics*, v. 27, no. 3, p. 609-623 (1967).
- Feng, Yin, M. Tyagi, and C. D. White. "A downhole heat exchanger for horizontal wells in low-enthalpy geopressured geothermal brine reservoirs." *Geothermics* 53 (2015): 368-378.
- Fridleifsson, I. B., R. Bertani, E. Huenges, J. W. Lund, A. Ragnarsson, and L. Rybach, "The possible role and contribution of geothermal energy to the mitigation of climate change." IPCC scoping meeting on renewable energy sources, proceedings, Luebeck, Germany. Vol. 20. No. 25. (2008).

- Gray, T.A., "Geothermal resource assessment of the Gueydan salt dome and the adjacent southeast Gueydan field. Masters thesis, Louisiana State University, Baton Rouge, LA (2010).
- Geertsma, J. "Land subsidence above compacting oil and gas reservoirs" *Journal of Petroleum Technology* 25.6 (1973): 734-744.
- Giardini, D. "Geothermal quake risks must be faced" *Nature* 462.7275 (2009): 848-849.
- Hochstein, M. P. "Classification and assessment of geothermal resources" *Small geothermal resources: A guide to development and utilization*, UNITAR, New York (1990): 31-57.
- Holm, A., D. Jennejohn, and L. Blodgett. "Geothermal energy and greenhouse gas emissions." *Geothermal Energy Association* (2012).
- Kagel, A., D. Bates, and K. Gawell. "A guide to geothermal energy and the environment" Washington, DC: Geothermal Energy Association, (2005).
- Kanamori, H., and D.L. Anderson. "Theoretical basis of some empirical relations in seismology. *Bull. Seism. Soc. Am.*, 65, 1073-1095 (1975).
- Kanamori, H., and E. E. Brodsky. "The physics of earthquakes." *Reports on Progress in Physics* 67, no. 8 (2004): 1429.
- Kehle, R. O. "Geothermal Survey of North America: 1972 Annual Progress Report." *American Association of Petroleum Geologists*, 1973.
- Kipp Jr, K. L. "Guide to the revised heat and solute transport simulator: HST3D version 2." *Water-Resources Investigations Report* 97-4157 (1997).
- Kodashima, T., and M. Kurashige. "Thermal stresses in a fluid-saturated poroelastic hollow sphere." *Journal of thermal stresses*: 19.2 (1996): 139-151.
- Lewis, R. W., and B. A. Schrefler. "The Finite Element Method in the Static and Dynamic Deformation and Consolidation of Porous Media" *John Wiley & Sons, Ltd.* (1998).
- Majer, E. L., R. Baria, M. Stark, S. Oates, J. Bommer, B. Smith, and H. Asanuma. "Induced seismicity associated with enhanced geothermal systems" *Geothermics* 36.3 (2007): 185-222.
- McTigue, D. F. "Thermoelastic response of fluidsaturated porous rock" *Journal of Geophysical Research*: 91.B9 (1986): 9533-9542.
- Muffler, P., and R. Cataldi. "Methods for regional assessment of geothermal resources" *Geothermics* 7.2 (1978): 53-89.
- Murphy, H. D., J. W. Tester, C. O. Grigsby, and R. M. Potter, "Energy extraction from fractured geothermal reservoirs in lowerpermeability crystalline rock" *Journal of Geophysical Research: Solid Earth* 86.B8 (1981): 7145-7158.
- Nicholson, K., "Geothermal fluids: chemistry and exploration techniques" *Springer Science and Business Media*, (2012).



- Rawal, C., and A. Ghassemi. "A reactive thermo-poroelastic analysis of water injection into an enhanced geothermal reservoir." *Geothermics* 50 (2014): 10-23.
- Rice, J. R., and M. P. Cleary. "Some basic stress diffusion solutions for fluidsaturated elastic porous media with compressible constituents" *Reviews of Geophysics* 14.2 (1976): 227-241.
- Ulgiati, S., and M. T. Brown. "Quantifying the environmental support for dilution and abatement of process emissions: the case of electricity production" *Journal of Cleaner Production*: 10.4 (2002): 335-348.
- Tanaka, A., M. Yamano, Y. Yano, and M. Sasada. "Geothermal gradient and heat flow data in and around Japan (I): Appraisal of heat flow from geothermal gradient data" *Earth, planets and space* 56.12 (2004): 1191-1194.
- Terzaghi, C. "Principles of soil mechanics: IVSettlement and consolidation of clay Engineering News-Record, (1925) v. 95, p. 874-878.
- Theis, C. V. "The relation between the lowering of the Piezometric surface and the rate and duration of discharge of a well using groundwater storage." *Eos, Transactions American Geophysical Union* 16.2 (1935): 519-524.
- Verruijt, A. "Theory and problems of poroelasticity" Delft University of Technology, The Netherlands (2013).
- Wang, H. "Theory of linear poroelasticity with applications to geomechanics and hydrogeology." Princeton University Press, 2000.
- Williams, C. F., M. J. Reed, R. H. Mariner, J. DeAngelo, and S. P. Galanis. "Assessment of moderate-and high-temperature geothermal resources of the United States No. 2008-3082. Geological Survey (US), (2008).
- Xu, Y., and D. D. L. Chung. "Cement of high specific heat and high thermal conductivity, obtained by using silane and silica fume as admixtures." *Cement and Concrete Research* 30.7 (2000): 1175-1178.

# Chapter 5

## Summary and Future Works

### 5.1 Summary

The ratio of normal-to-shear compliance can be used for reservoir characterization and depletion optimization. As extensively discussed in the literature, this ratio is sensitive to fracture roughness, type of the fluid filling the fracture, fluid viscosity, rock permeability, fracture connectivity and the presence of cement, clay and other fracture fillings. Fracture faces always consist of asperities and morphological irregularities. It is shown in the literature that the degree of contact between the fracture faces controls fluid flow and electrical current as well as fracture mechanical properties. Fracture roughness in the form of asperities might be generated during joint formation or faulting. These features on the surface of fractures can affect measured compliance ratios. In Chapter 2, the author employs quasi-static and dynamic approaches to investigate the effects of contact area and interface offset on the fracture compliance ratio. This research proposal studied different geometrical and offset configurations to show how compliance ratio is a function of available contact area at the fracture interface and also the size of the asperities. For a single smooth crack in a tensile stress in a 2D infinite medium, the compliance ratio equals to 1. However, this study shows that compliance ratio increases to values more than 1 if the fracture has rough faces. The interlocking of asperities on fracture faces can significantly influence the compliance ratio in the stiff direction. The deviation in the compliance ratio for the soft direction from 1, suggested by the analytical solution for a single smooth crack, can be explained by the riding

up effect. It is notable that interlocking is not the only parameter governing the interaction between rough fracture faces. The contact area between the fracture faces is also controlled by effective stress that affects the excess of compliance ratio, as shown in Figures 2.8 to 2.10.

Temperature difference between fracturing fluid and reservoir can induce thermal tensile stress on the surface of hydraulic fracture. The induced tensile stress may open cemented natural fractures, improving the formation-fracture contact area as well as enhancing the rock permeability in the vicinity of hydraulic fracture. Most of natural fractures are smaller in length than the hydraulic fracture; however, they exist in large numbers. Cohesive interface theory models the reactivation of natural fractures in this study. Semicircular bending test of the Woodford shale samples defines the cohesive interface properties used in our numerical experiments. Cohesive stiffness degradation of 1, SDEG, dictates the length of reactivated crack. This study suggests that the length and width of reactivated length depends on the spacing of natural fractures, rock thermal conductivity, temperature difference between fracturing fluid and the reservoir, and strength of cemented materials filling natural fractures. Larger spacing between natural fractures results in longer and more uniform activated cracks since the stress shadow effect of neighboring cracks is smaller. Injecting a colder fracturing fluid into a reservoir with larger thermal conductivity increases the length of reactivated fractures as more energy is available for crack propagation. Weaker cementing materials require lower energy to be damaged. In other words, more induced tensile energy can be consumed to propagate deeper fractures. Transmissibility coefficient for areas nearby the hydraulic fracture can be modified in way to include the contribution of reactivated natural fractures in permeability enhancement, shown in Equation (3.5).

A comprehensive analysis were provided of a new method for heat extraction from the low-enthalpy geothermal reservoirs without mass withdrawal. The developed coupled numerical model in this study assesses the effectiveness of the proposed closed-loop configuration including the induced hydraulic fractures propped with highly thermal conductive materials to enhance heat production. The highly conductive proppants placed inside the fracture vir-

tually increase the wellbore-formation contact area through absorbing the heat from a larger volume of the reservoir. In comparison with the conventional hydraulic fracturing treatments in oil of gas industry, the proppants crushing in this technique has a positive impact, since the crushed proppants still can transfer the heat from the reservoir to the wellbore. As it is shown in detail in chapter 4, the magnitude of surface subsidence and displacements across the formation is very small which significantly reduces the risk of induced seismicity compared to open-loop systems. The rate of heat flow into the wellbore in our technique strongly depends on the thermal conductivity of the proppants, the temperature gradient between the circulating working fluid and the reservoir, and the magnitude of increase in the wellbore-formation contact area. The numerical simulations show promising economic value for the application of this technique to horizontal wellbores.

## 5.2 Recommendations for Future Works

The following recommendations are made for possible future research:

### Chapter 2

- Develop a fracture model with more complicated fracture interface and measure the compliance ratio.
- Apply more numerical experiments on the measurement of dynamic compliance ratio.
- Build a 3D model to measure out-of-place compliance.
- Conduct lab experiments to compare the experimental dynamic compliance ratio with the numerical compliance ratio for different rock samples with different rough faces.
- Model the compliance of propped fractures and role of proppants on the fracture compliance.

### Chapter 3

- Conduct lab measurements on the shale samples with cemented natural fractures. The cohesive properties of cementing materials can be then used to calculate the length and width of reactivated fractures.
- Model a more complicated natural fractures network to study the reactivation of natural fractures intersecting each other.
- Model the reactivation of natural fractures with damage mechanics and compare it with cohesive zone model.
- Model the extra leak-off due to opened natural fractures.

### Chapter 4

- Include the damage mechanics in the developed thermoelastic FEM code to model the fracture initiation-propagation.
- Study the wellbore integrity of the proposed configuration and characterize cement sheath integrity.
- Investigate on the cement additives to improve the heat extraction efficiency around the wellbore.
- Cementing the induced propped hydraulic fractures with thermally conductive cements and measure the heat extraction.

# Appendix A: FEM Discretization of Non-Isothermal Saturated Porous Media

In this Appendix, the strong and the weak form of the partial differential equations for mass, energy, momentum balance, and solid constitutive laws are presented. FEM discretization, containing weak forms of the partial equations, is a non-linear algebraic equation. By applying the weighted residual method on the differential equations, we have:

$$\int_{\Omega} (Lw)^T \sigma d\sigma = \int_{\Omega} w^T \rho g d\sigma + \int_{\Gamma} w^T \bar{t} d\Gamma \quad (1)$$

$$\begin{aligned} & \int_{\Omega} [w^{*T} (\frac{\alpha - \phi}{K_s} + \frac{\phi}{K_f}) \frac{\partial P_f}{\partial t} + w^{*T} \alpha m_T L \frac{\partial u}{\partial t} - w^{*T} \beta_{sf} \frac{\partial T}{\partial t}] d\sigma \\ & - \int_{\Omega} [(\nabla w^*)^T \frac{k}{\mu_f} (-\nabla P_f + \rho_f g)] d\sigma - \int_{\Omega} [(\nabla w^*)^T \frac{k}{\mu_f} (-\nabla P_f + \rho_f g)] d\sigma \\ & + \int_{\Gamma} w^{*T} \frac{q_f}{\rho_f} d\Gamma = 0 \end{aligned} \quad (2)$$

$$\begin{aligned} & \int_{\Omega} [w^{\circ T} (\rho C_p)_{eff} \frac{\partial T}{\partial t} + w^{\circ T} (\rho_f C_{pf} \frac{k}{\mu_f} (-\nabla P_f + \rho_f g)) \cdot \nabla T] d\sigma \\ & - \int_{\Omega} \nabla w^{\circ T} (-\chi_{eff} \nabla T) d\sigma + \int_{\Gamma} w^{\circ T} (q^T + h(T - T_0)) d\Gamma = 0 \end{aligned} \quad (3)$$

To discretize the integral form of balance equations, the nodal values and shape functions express the variable parameters as follows:

$$\begin{aligned} u &= N_u \bar{u} \\ P_f &= N_p \bar{P}_f \\ T &= N_T \bar{T} \end{aligned} \quad (4)$$

$$\int_{\Omega} (LN_u)^T (\sigma'' + \alpha m P_f N_p) d\sigma = \int_{\Omega} N_u^T \rho g d\sigma + \int_{\Gamma} N_u^T \bar{t} d\Gamma \quad (5)$$

$$\begin{aligned} & \int_{\Omega} [N_p^T (\frac{\alpha - \phi}{K_s} + \frac{\phi}{K_f}) N_p \frac{\partial \bar{P}_f}{\partial t} + N_p^T \alpha m^T L N_u \frac{\partial \bar{u}}{\partial t} - N_p^T \beta_{sf} N_T \frac{\partial \bar{T}}{\partial t}] d\sigma \\ & + \int_{\Omega} [-\nabla N_p^T \frac{k}{\mu_f} \rho_f g + \nabla N_p^T \frac{k}{\mu_f} \nabla N_p \bar{P}_f] d\sigma + \int_{\Gamma} N_p^T \frac{q_f}{\rho_f} d\Gamma = 0 \end{aligned} \quad (6)$$

$$\begin{aligned} & \int_{\Omega} [N_T^T (\rho C_p)_{eff} N_T \frac{\partial \bar{T}}{\partial t} + N_T^T [(\rho_f C_{pf} \frac{k}{\mu_f} (-\nabla P_f + \rho_f g)) \cdot \nabla N_T] \bar{T}] d\sigma \\ & - \int_{\Omega} \nabla N_T^T (-\chi_{eff} N_T^T) \bar{T} d\sigma + \int_{\Gamma} N_T^T (q^T + h(T - T_0)) d\Gamma = 0 \end{aligned} \quad (7)$$

$$\begin{aligned} & \int_{\Omega} B^T \sigma'' d\sigma + Q \bar{P}_f = f_u \\ & H \bar{P}_f + Q^T \frac{\partial \bar{u}}{\partial t} + S \frac{\partial \bar{P}_f}{\partial t} + \frac{\partial \bar{T}}{\partial t} = f_p \\ & K_T \bar{T} + C_T \frac{\partial \bar{T}}{\partial t} = f_T \end{aligned} \quad (8)$$

$$\begin{aligned} B &= L N_u \\ Q &= \int_{\Omega} B^T \alpha m N_p d\sigma \\ S &= \int_{\Omega} N_p^T (\frac{\alpha - \phi}{K_s} + \frac{\phi}{K_f}) N_p d\sigma \\ R &= \int_{\Omega} -N_p^T \beta_{sf} N_T d\sigma \\ K_t &= \int_{\Omega} N_T^T [\rho_f C_{pf} \frac{k}{\mu_f} (-\nabla P_f + \rho_f g)] \cdot \nabla N_T d\sigma - \int_{\Omega} \nabla N_T^T (-\chi_{eff}) \nabla N_T d\sigma \\ C_T &= \int_{\Omega} N_T^T (\rho C_p)_{eff} N_T d\sigma \\ f_u &= \int_{\Omega} \rho g d\sigma + \int_{\Gamma} N_u^T \bar{t} d\Gamma + \int_{\Omega} B^T D_e \varepsilon_0 d\sigma \\ f_p &= \int_{\Omega} (\nabla N_p)^T \frac{k}{\mu_f} \rho_f g d\sigma - \int_{\Gamma} N_p^T \frac{q_f}{\rho_f} d\Gamma \\ f_p &= - \int_{\Gamma} N_T^T (q^T + h(T - T_0)) d\Gamma \end{aligned} \quad (9)$$

By applying the constitutive laws for an isotropic linear elastic medium, we will have:

$$\begin{aligned}
\int_{\Omega} B^T \sigma'' d\sigma &= \int_{\Omega} B^T D_e (\varepsilon - \varepsilon_0 - \varepsilon^T) d\sigma = -K_e \bar{u} + K_{te} \bar{T} - \int_{\Omega} B^T D_e \varepsilon_0 d\sigma \\
K_e &= \int_{\Omega} B^T D_e B d\sigma \\
K_{te} &= \int_{\Omega} B^T D_e m \frac{\beta_s}{3} N_T d\sigma
\end{aligned} \tag{10}$$

The non-linear behavior of the solid phase can be established as:

$$\begin{aligned}
\frac{\partial P(\bar{u})}{\partial \bar{u}} &= K_T = \int_{\Omega} B^T D_T B d\sigma \\
\frac{\partial P(\bar{u})}{\partial \bar{T}} &= K_{tT} = - \int_{\Omega} B^T D_e m \frac{\beta_s}{3} N_T d\sigma
\end{aligned} \tag{11}$$

Based on the above calculations, the governing equations can be written as:

$$\begin{bmatrix} 0 & 0 & 0 \\ 0 & H & 0 \\ 0 & 0 & K_t \end{bmatrix} \times \begin{bmatrix} \bar{u} \\ \bar{P}_f \\ \bar{T} \end{bmatrix} + \begin{bmatrix} K_T & -Q & K_{tT} \\ Q^T & S & R \\ 0 & 0 & C_t \end{bmatrix} \times \begin{bmatrix} \frac{\partial \bar{u}}{\partial t} \\ \frac{\partial \bar{P}_f}{\partial t} \\ \frac{\partial \bar{T}}{\partial t} \end{bmatrix} = \begin{bmatrix} \frac{\partial f_u}{\partial t} \\ f_p \\ f_t \end{bmatrix} \tag{12}$$

To solve the dynamic problem, the central difference in time is applied to the above general equations:

$$\begin{aligned}
&\begin{bmatrix} K_T & -Q & K_{tT} \\ Q^T & S - (1 - \theta)\Delta t H & R \\ 0 & 0 & C_t - (1 - \theta)\Delta t K_t \end{bmatrix} \times \begin{bmatrix} \bar{u}_{n+1} \\ \bar{P}_{f_{n+1}} \\ \bar{T}_{n+1} \end{bmatrix} \\
&= \begin{bmatrix} K_T & -Q & K_{tT} \\ Q^T & S + \theta\Delta t H & R \\ 0 & 0 & C_t + \theta\Delta t K_t \end{bmatrix} \times \begin{bmatrix} \bar{u}_n \\ \bar{P}_{f_n} \\ \bar{T}_n \end{bmatrix} + \Delta t \begin{bmatrix} \frac{\partial f_u}{\partial t} \\ f_p \\ f_t \end{bmatrix}
\end{aligned} \tag{13}$$



# Appendix B: Analytical Solution of Benchmark Problems

This appendix contains the analytical solution (Verruijt, 2013) for the benchmark problems, discussed in the numerical validation section.

- Mandel's Analytical Solution

$$\frac{P}{P_0} = 2\eta \sum_{k=1}^{\infty} \frac{\cos(\xi_k) [\cos(\frac{\xi_k x}{a}) - \cos(\xi_k)]}{1 - 2\eta \cos^2 \xi_k} \exp(-\xi_k^2 \frac{c_v t}{a^2}) \quad (14)$$

$$\begin{aligned} c_v &= \frac{\kappa(K + \frac{4}{3}G)}{\gamma_f} \\ P_0 &= \frac{P_{load}}{2} \\ \eta &= \frac{1 - \nu}{1 - 2\nu} \\ \kappa &= \frac{k\rho_f g}{\mu} \\ \frac{\sin(\xi_k)}{\xi_k} &= 2\eta \cos(\xi_k) \end{aligned} \quad (15)$$

- Theis-Jacob's Analytical Solution

$$\begin{aligned} P &= \frac{P_{load}\mu_f}{\rho_f k} [(x - H) + \\ &\sum_{k=1}^{\infty} \frac{2H}{(2k-1)\pi} \frac{\sin(\frac{(2k-1)\pi(x-H)}{2H})}{\frac{3}{2}\cos(\frac{(2k-1)\pi}{2}) - \frac{2k-1}{4}\pi\sin(\frac{(2k-1)\pi}{2})} ] \end{aligned} \quad (16)$$

Verruijt, A. “Theory and problems of poroelasticity” Delft University of Technology, The Netherlands (2013).

# Appendix C: Letters of Permission to Use Published Material

MA

Milad Ahmadi  
6/17/2016  
journals.permissions@oup.com <Journals.Permissions@oup.com> ✕

👍 ⌵ Reply all ⌵

Sent Items

To whom it may concern,

I'm the first author of a paper published in the **Geophysical Journal International** with the title of "*The effects of roughness and offset on fracture compliance ratio*" and doi of [10.1093/gji/ggw034](https://doi.org/10.1093/gji/ggw034). I would like to include this paper as one of the chapters in my PhD dissertation. I have tried to request for a written permission from the Geophysical Journal International website but I was not successful. I appreciate if you can guide me on how to receive such a permission form your journal.

Thanks in advance

Best regards,  
Milad Ahmadi

Request a permission ⌵

JP

JOURNALS PERMISSIONS <Journals.Permissions@oup.com> 6/23/2016

▶ 📧 ⌵

Dear Milad Ahmadi,

RE. M. Ahmadi et al. The Effects of Roughness and Offset on Fracture Compliance Ratio. *Geophysical Journal International* (2016) 205 (1): 454-463

Thank you for your recent email requesting permission to reuse all or part of your article in a thesis/dissertation.

As part of your copyright agreement with Oxford University Press you have retained the right, after publication, to use all or part of the article and abstract, in the preparation of derivative works, extension of the article into a booklength work, in a thesis/dissertation, or in another works collection, provided that a full acknowledgement is made to the original publication in the journal. As a result, you should not require direct permission from Oxford University Press to reuse you article.


In line with the journal self-archiving policy, you may include either your **accepted manuscript PDF** or **your version of record PDF** in your thesis/dissertation. For full details of our publication and rights policy please see the attached link to our website:  
<http://www.oxfordjournals.org/en/access-purchase/rights-and-permissions/self-archiving>.

If you have any other queries, please feel free to contact us.

Kind regards,  
Louise

Miss Louise Eyre  
Permissions Assistant | Rights Department  
Academic and Journals Divisions | Global Business Development  
Oxford University Press  
Great Clarendon Street | Oxford | OX2 6DP

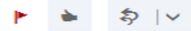
Tel: +44(0)1865 354454 | Email: [louise.eyre@oup.com](mailto:louise.eyre@oup.com)



## Permission request



Jennifer Cobb <jcobb@seg.org>  
6/17/2016



Dear Milad,  
Authors may reuse all or part of their papers published with SEG in a thesis or dissertation that authors write and are required to submit to satisfy criteria of degree-granting institutions.

Please let me know if you have more questions.

Sincerely,  
**Jennifer Cobb** | Director, Journals and Books  
+1.918.497.5537 direct  
[Society of Exploration Geophysicists \(SEG\)](#)  
[8801 South Yale Ave, Ste. 500 Tulsa, OK 74137 USA](#)

On Jun 17, 2016, at 2:52 PM, Milad Ahmadi <[mahmad7@lsu.edu](mailto:mahmad7@lsu.edu)> wrote:

To whom it may concern,

I'm the first author of a paper published in the **Geophysics** with the title of "*Direction dependence of fracture compliance induced by slickensides*" and doi of 10.1190/geo2013-0227.1

I would like to include some parts of this paper in one of the chapters in my PhD dissertation. I have tried to request for a written permission from the Geophysics website but I was not successful. I appreciate if you can guide me on how to receive such a permission from your journal.

Thanks in advance

Best regards,

# Vita

Milad Ahmadi was born in Tehran, Iran in 1986. He joined Craft and Hawkins Department of Petroleum Engineering geomechanics research group at LSU as a Ph.D. student in Spring 2012 where he started his research under the supervision of Dr. Arash Dahi-Taleghani.

He holds a B. S. in Chemical Engineering and a M. S. degree in Petroleum Engineering at University of Tehran. He is currently a member of Society of Petroleum Engineers (SPE), American Rock Mechanics Association chapter LSU (ARMA), and American Petroleum Professionals of Iranian Heritage (APPIH).

Milad Ahmadi is expected to receive his Doctor of Philosophy degree at the 2016 Summer Commencement. He may be reached at milad.amd7@gmail.com in future.